Inaugural dissertation

for

obtaining the doctoral degree

of the

Combined Faculty of Mathematics, Engineering and Natural Sciences

of the

Ruprecht - Karls - University

Heidelberg

Presented by

M.Sc. Ana Yagüe Relimpio

born in: Barcelona, Spain

Oral examination: December 10th, 2024

# Design and development of bottom-up assembled SARS-CoV-2 miniviruses to investigate the impact of lipid species on infectivity

Referees: Prof. Dr. Hans-Georg Kräusslich

Prof. Dr. Joachim P. Spatz

# Abstract

Research of highly pathogenic viruses, such as SARS-CoV-2, is often challenging due to their inherent variability and complexity, and has to be performed in a high biosafety environment. The use of bottom-up synthetic biology provides tools to investigate specific aspects of the viral life cycle in a controlled manner. To address this I designed bottom-up synthetic SARS-CoV-2 miniviruses, named MiniVs, with the aim to study the influence of lipids on the attachment process of the viral cycle. To conduct a functional screening comparing Omicron and Alpha spike glycoproteins I utilised both ACE2-functionalised and non-functionalised planar supported lipid bilayers and giant unilamellar vesicles and discovered that Omicron had a previously unreported affinity towards lipid membranes. I measured the dissociation constants of both variant spikes to a lipid membrane and demonstrated that the affinity of Omicron spike is twice as high as the one of Alpha. These findings were further validated using two cell lines, with and without ACE2 receptor expression. Moreover, modification of the plasma membrane composition proved the importance of cholesterol in the attachment step of SARS-CoV-2. Loading the cellular membrane with different amounts of cholesterol enhanced the attachment of Omicron MiniVs. The same treatment had the opposite effect on Alpha MiniVs suggesting that the effect observed on the cell membrane is not due to membrane reorganisation and receptor clustering. Measuring the interaction between Omicron spike and SLBs with increasing amounts of cholesterol indicated that there is no specific affinity between the protein and the lipid. Finally I produced spike proteoliposomes, which consisted of full-length transmembrane Alpha or Omicron spike inserted into small unilamellar vesicles. I demonstrated that the full-length spike glycoprotein can be inserted into vesicles while remaining functional and binding to the ACE2 receptor. Proteoliposomes that contained a higher content of cholesterol on their membrane showed an increased interaction with the ACE2 receptor. Altogether, the research presented here underscores the advantages of using synthetic bottom-up assembled viruses to investigate the importance of lipids on viral infectivity, specifically during viral attachment. The results obtained highlight the differences between SARS-CoV-2 variants Alpha and Omicron, and partially explain their distinct transmissibility and pathogenicity patterns. The use of MiniVs and proteoliposomes offers a novel platform for studying specific aspects of the viral life cycle that are challenging to examine with conventional biological methods.

# Zusammenfassung

Die Erforschung pathogener Viren wie SARS-CoV-2 ist aufgrund ihrer inhärenten Variabilität und Komplexität oft eine Herausforderung und muss in einer Umgebung mit hoher biologischer Sicherheit durchgeführt werden. Die Verwendung der Bottom-up-Synthetischen Biologie bietet Werkzeuge, um bestimmte Aspekte des viralen Lebenszyklus auf kontrollierte Weise zu untersuchen. Um dieses Problem anzugehen, habe ich synthetische Bottom-up-SARS-CoV-2-miniViren, genannt MiniVs, entwickelt, mit dem Ziel, den Einfluss von Lipiden während der Adsorption im viralen Zyklus zu untersuchen. Um eine funktionelle Untersuchung durchzuführen, bei dem Omicron- und Alpha-Spike-Glykoproteine verglichen wurden, verwendete ich sowohl ACE2-funktionalisierte als auch nicht funktionalisierte planare Lipidschichten und große unilamellare Vesikel und entdeckte, dass Omicron eine bisher nicht berichtete Affinität zu Lipidmembranen aufweist. Ich maß die Dissoziationskonstanten beider spike Proteine zu einer Lipidmembran und zeigte, dass die Affinität des Omicron-Spike doppelt so hoch ist wie die des Alpha-Spike. Diese Ergebnisse wurden durch die Verwendung von zwei Zelllinien mit und ohne ACE2-Rezeptorexpression weiter validiert. Darüber hinaus bewies die Modifizierung der Plasmamembranzusammensetzung die Bedeutung von Cholesterin in der Adsorption des SARS-CoV-2 Virus. Das Beladen der Zellmembran mit unterschiedlichen Mengen an Cholesterin verstärkte die Anheftung von Omicron MiniVs. Die gleiche Behandlung hatte bei Alpha MiniVs den gegenteiligen Effekt, was darauf hindeutet, dass der beobachtete Effekt auf die Zellmembran nicht auf eine Membran-Umstrukturierung und Rezeptor-clustering zurückzuführen ist. Die Messung der Interaktion zwischen Omicron-Spike und Lipidschichten mit zunehmenden Cholesterinmengen zeigte, dass es keine spezifische Affinität zwischen dem Protein und dem Lipid gibt. Schließlich stellte ich Spike-Proteoliposomen her, die aus einem Alpha- oder Omicron-Spike in voller Länge bestanden, welches in kleine unilamellare Vesikel eingebracht wurde. Ich konnte nachweisen, dass das Spike-Glykoprotein in voller Länge in Vesikel eingefügt werden kann, während es funktionsfähig bleibt und an den ACE2-Rezeptor bindet. Proteoliposomen, die einen höheren Cholesteringehalt auf ihrer Membran aufwiesen, zeigten eine verstärkte Interaktion mit dem ACE2-Rezeptor. Insgesamt unterstreicht die hier vorgestellte Forschung die Vorteile der Verwendung synthetisch aufgebauter Viren zur Untersuchung der Bedeutung von Lipiden für die virale Infektiosität, insbesondere während der viralen Adsorption. Die erzielten Ergebnisse heben die Unterschiede zwischen den SARS-CoV-2-Varianten Alpha und Omicron hervor und erklären teilweise ihre unterschiedlichen Übertragbarkeits- und Pathogenitätsmuster. Die Verwendung von MiniVs und Proteoliposomen bietet eine neuartige Plattform zur

Untersuchung spezifischer Aspekte des viralen Lebenszyklus, die mit herkömmlichen biologischen Methoden nur schwer zu untersuchen sind.

# Contents

# List of Figures

# List of Tables

# 1 Introduction

Severe acute respiratory syndrome coronavirus 2 (SARS-CoV-2) is the virus responsible for the COVID-19 pandemic.[1] The sudden need for new treatments and vaccines has underscored the urgency in developing innovative approaches to understand and combat new viruses.[2] Traditional biology and virology methods, while powerful and effective, often face considerable limitations specifically when addressing highly infectious pathogens. A major drawback is the requirement for high-level biosafety facilities to conduct research with these viruses.[3] Furthermore, they regularly lack control over the composition of the *in vitro*-produced viral particles. Bottom-up synthetic biology enables the design and construction of biological systems with precise control over their functions and composition, a feature which is often lacking in top-down approaches and standard biology methods.[4]

In this thesis I will utilise bottom-up assembled synthetic SARS-CoV-2 miniviruses (MiniVs) to investigate the effect of lipid species on SARS-CoV-2 infectivity. The natural viral envelope is decorated with the spike glycoprotein (S), which is responsible for binding the angiotensin-converting enzyme 2 (ACE2) receptor and initiating infection.[5] I will imitate the external appearance of the natural virus by using liposomes functionalised with S to create MiniVs. Thanks to the modularity of the system, the lipid composition of the vesicles will be tuned at will and they will be functionalised with different S variants. I will study the role of the lipid composition on both the cellular and the viral envelope membrane, all while exploring different ways of producing these minimal synthetic viruses.

In this chapter I will delve into the complexity of the SARS-CoV-2 virus and explore the various methods available for producing viral particles to study viruses.

## 1.1 Viruses

Viruses are submicroscopic noncellular infectious agents which replicate inside of living cells, these being eukaryotes or prokaryotes. Not all viruses cause disease, some exist within their host in a non-pathogenic state, either actively or quiescently. Beyond being studied to develop cures for virus-borne illnesses, viruses have the potential for diverse applications, from biotechnology to ecology.[6]

### 1.1.1 Enveloped and non-enveloped viruses

Many of the viruses that infect animals are enveloped, meaning that they present a lipid membrane that surrounds their protein capsid and genetic material. This membrane is derived from host cell membranes, which can be the plasma membrane or other intracellular membranes along the secretory pathway.[7] Typically, enveloped viruses adopt a spherical appearance, such as the one of SARS-CoV-2. However, other shapes can be observed, such as bullet (Rabies virus), rod (Baculoviruses) or thread-like (Ebola virus).[8–10] Other examples of enveloped viruses are influenza, herpes and coronaviruses.[11–13] Non-enveloped, also called naked viruses, present an external structure formed by a protein capsid that encloses the viral genome. The proteins that form the capsid assemble in symmetrical structures, the most common being helical and icosahedral symmetries. These type of capsid structures can be found in both enveloped and non-enveloped viruses. Examples of non-enveloped viruses are norovirus, enterovirus, adenovirus and rhinovirus.[6]

### 1.1.2 The viral cycle

For viruses to replicate they need to complete the following steps: attachment to the host cell, crossing the plasma membrane or cell wall, transcription and translation of the viral proteins, replication of their genome, assembly into virions and exit from the cell. These steps vary among species and they do not always follow the same order.[6] A schematic illustration of the replication cycle of an enveloped virus is shown in Figure 1.1. Receptors on the host cell membrane used by animal-infecting viruses are primarily proteins, but can also be of carbohydrate or lipid origin. After attachment to specific receptors on the cell surface, animal enveloped viruses enter the cells via fusion, either at the plasma membrane, such as the human immunodeficiency virus (HIV), or with an endocytic compartment, such as influenza A.[14] There are also viruses which exploit both entry pathways, such as SARS-CoV-2 which can fuse at the membrane after cleavage by the transmembrane protease serine 2 (TMPRSS2) or in the endosome

after cleavage via cathepsins.[15] Non-enveloped viruses, on the other hand, cannot fuse with any membrane as they are lack a lipid envelope. Instead they break the cell membrane, such as poliovirus, or an endosome, such as adenoviruses, to deliver their genetic material.[14]

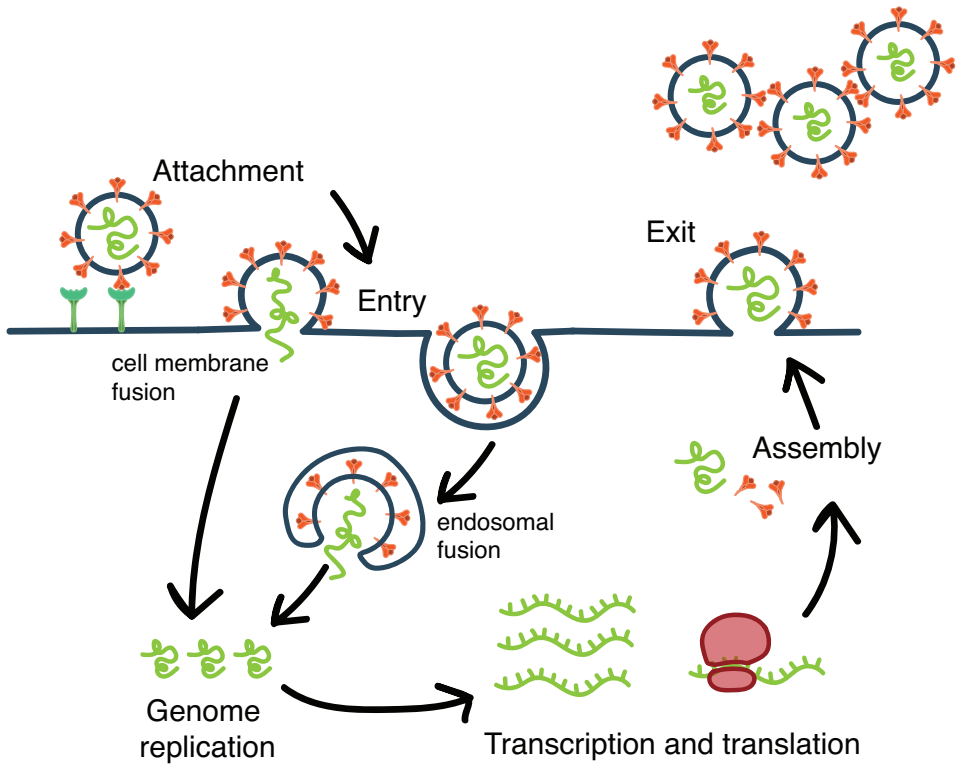


**Figure 1.1: Schematic illustration of the life cycle of an enveloped virus.** After attachment to a specific receptor, enveloped viruses proceed to enter the cell. Fusion can take place at the plasma membrane or later at the endosomal compartment. Once the genetic material has been released, it is replicated and transcribed for protein production. Viral proteins assemble at the membrane from which the virus buds, while genetic material is packaged inside, allowing new virions to exit the cell.

The viral genome can be classified into single or double-stranded DNA or RNA. This means that there are different modes of transcription. Some viruses have the same sequence as the mRNA, which are designated as (+). The ones who contain the mRNA complementary sequence are labelled (-). The genomes will be directly transcribed to mRNA or an intermediate sequence (dsDNA or RNA) will be produced before final transcription into mRNA. Translation produces proteins needed for genome replication, to aid that said replication or to generate the proteins that will form the progeny virions. At the same time, the viral genome needs to be replicated to amplify transcription and to produce copies for the new virions. The replication of the viral genome can take place in the cytoplasm (the case for most RNA viruses) or in the nucleus (the case for most

DNA viruses).[6,14]

Before egress from the cell, the viral proteins and genome need to assemble into new virions. The structures adopted by virions are varied, from helical structures (ebolavirus) to icosahedral ones (adenovirus). Some of them acquire an envelope after viral capsid assembly. The majority of virions obtain their lipid envelope by budding from the plasma membrane. Others, such as coronaviruses, bud from the endoplasmic reticulum and use the Golgi pathway to exit the cell. Before acquiring the envelope, viral proteins are inserted into the membrane from which the virus will bud. After exit, most viruses remain inert until they encounter and infect a new target cell. In some cases, they undergo maturation of their viral proteins.[6,14]

### 1.1.3 SARS-CoV-2

SARS-CoV-2 is a positive-sense single-stranded RNA virus classified as *Betacoronavirus*, within the *Coronaviridae* family. Other viruses that belong to the same genera are the Middle East respiratory syndrome–related coronavirus (MERS-CoV) and SARS-CoV, both of which cause a respiratory illness as well.[1] Since its outbreak in December 2019, thousands of different variants have been classified into five main variants of concern (VOCs) named Alpha (B.1.1.7), Beta (B.1.351), Gamma (P.1), Delta (B.1.617.2) and Omicron (B.1.1.529).[16] SARS-CoV-2 virions have a size ranging from 60-140 nm and are surrounded by a lipid membrane which protects the genetic material.[17] The virus genome is around 30 kb long which translates into 11 accessory, 16 non-structural and 4 structural proteins.[18] Three of the four structural proteins are found in the membrane: envelope (E), membrane (M) and S proteins. The other structural protein is the nucleocapsid (N) protein, which binds to the RNA and has roles in viral replication and assembly. The E and M proteins are embedded in the lipid membrane and have functions in viral assembly, budding and virulence (E) and maintaining the virion's size and shape (M).[19] S, formed by subunits S1 and S2, is a glycoprotein that assembles around the viral envelope giving it its crown-like appearance. It is responsible for the start of the infection by interacting with the ACE2 receptor which mediates viral entry into host cells.[5] In addition to ACE2, other receptors have been proposed as potential interacting partners of S, from proteins such as CD147 and AXL to polysaccharides like heparan sulfate.[20–22]

Once the virus is docked, a cell membrane protease named TMPRSS2 primes S. This induces a conformational change in S that exposes the fusion peptide within the S2 subunit, which induces fusion with the cell membrane and the release of the genetic

material.[23] In cases in which the ACE2 endogenous expression is low - or the S-ACE2 complex does not encounter TMPRSS2 - the virus is internalised and fuses later in the endosomal compartment. When acidification of the endosome occurs, proteins called cathepsins activate and prime S and fusion takes place.[15] The use of either entry pathway depends on the virus variant, with the latter being more prominent specifically for the Omicron lineage.[24] Once the fusion process has been completed, primary translation of viral proteins takes place, followed by RNA synthesis, assembly at the endoplasmic-reticulum-Golgi intermediate compartment (ERGIC) and final exocytosis which releases the virus.[25]

### 1.1.4 SARS-CoV-2 variants

The first reports of a new respiratory infection appeared in December 2019 in Wuhan, China. The original COVID-19 paper described the origin of the infection to be an RNA virus strain from the family *Coronaviridae*, and specifically being closely related to a group of SARS-like coronaviruses found in bats.[26] One of the most important mutations since its host jump into humans was D614G, which was detected in Europe for the first time in January 2020.[27] It is believed that the mutation conferred the virus a selective advantage which led to a faster spread and higher viral load compared to the previous 614D SARS-CoV-2 variant.[28]

From mid 2020 new SARS-CoV-2 variants, presenting differences in terms of transmissibility, severity and antigenicity, started to emerge. Alpha, Beta, Gamma, Delta and Omicron were the five VOCs defined by the World Health Organization (WHO), as they presented a substantial danger to the global public health.[29] The first VOC identified by the WHO was Alpha (B.1.1.7) in September 2020 in the United Kingdom, although later studies revealed that Beta (B.1.351) emerged in May 2020 in South Africa.[29] One of the main differences among variants lies in the mutations within S, particularly in the receptor binding domain (RBD). This, in turn, leads to differences in affinity to the ACE2 receptor, being Omicron and Alpha the ones with highest and Wuhan the one with lowest affinity to the receptor.[24,30,31]

### 1.1.5 SARS-CoV-2 Alpha variant

The B.1.1.7 variant, commonly called Alpha, was the first identified variant of concern by the WHO and rapidly became the predominant circulating strain. SARS-CoV-2 Alpha was not only more transmissible than preexisting variants, but also caused more severe disease.[32] From the mutations it presents in the RBD, the N501Y substitution is

the most relevant as it is involved in receptor affinity. This change from asparagine to tyrosine led to a higher interaction with the ACE2 receptor, a faster association rate and a slower dissociation rate.[33]

Moreover, deletion of H69/V70 conferred the variant with an increased incorporation of S into virions, and higher kinetics of cell-cell fusion which play a role in viral replication.[34] Substitutions N439K and Y453F were also found in multiple lineages and it was demonstrated that both aid in immune system evasion. Furthermore, the N439K mutation results in a twofold increase in affinity for ACE2.[35,36] Another mutation, E484K, appeared later in the Alpha variant as well as in other Beta lineages, conferring resistance to monoclonal antibodies and thus providing immune escape.[37]

### 1.1.6 SARS-CoV-2 Omicron variant

The last variant to emerge was Omicron, with the earliest documented samples in November 2021.[29,38] The high amount of mutations within the genome of Omicron quickly led to the classification of the strains into subvariants BA.1-5. The lineages showed different binding affinity to the ACE2 receptor, as well as cell entry efficiency.[39] Several of these mutations overlap with those found in the other VOCs, including N501K and the H69/V70 deletion described previously. Aside from the elevated ACE2 affinity, Omicron subvariants are more infectious than previous variants and present increased transmissibility.[40,41] Nonetheless, despite its high transmissibility which replaced previous variants from circulation, infection with Omicron subvariants induced less severe disease in comparison to the earlier variant Delta.[41,42]

There are six mutations in the S2 domain of S that are unique to Omicron, three of which are associated with a loss in S cleavage, fusogenicity and cell-cell fusion.[43,44] Experiments in animal models suggested that the diminished Omicron pathogenicity is due to its inability to replicate in lung tissues. Moreover, Omicron S appears to be resistant to cleavage by furin proteases.[44] As S cleavage is correlated to fusogenicity and pathogenicity, this feature of the Omicron S might explain the lower virulence of the variant.[45] Another factor that is linked to SARS-CoV-2 pathogenesis is the ability to induce syncytium formation, i.e. cell-cell fusion.[46] This process is dependent on S cleavage and is accelerated by the presentation of TMPRSS2, which explains the impaired capacity of Omicron S to promote cell-cell fusion.[47]

Supporting the fact that Omicron S appears to have an impaired cleavage, it has been shown that it replicates prominently in upper respiratory tract regions - instead of lungs - where TMPRSS2 expression is lowered. This contrasts with the Delta and WT variants,

which can efficiently replicate in the lungs. Researchers also found that Omicron's entry is independent on TMPRSS2 presentation however it is affected by inhibitors of the endocytic pathway.[24] The lower replication competence of Omicron in the lungs might partially explain the lower pathogenicity of the variant.[48]

Omicron also presents a different cell tropism compared to other variants, which could as well be a reason for its higher transmissibility. Increased viral titers in the conducting airways may lead to a greater release of viral particles in the oral cavity, which would aid airborne virus transmission.[48] Another factor that might enhance the increased transmissibility of the Omicron variants is the impaired neutralisation by antibodies. The virus variant resisted neutralisation by clinically-approved monoclonal antibodies, as well as by sera from infected or vaccinated patients.[49]

### 1.1.7 Spike glycoprotein

S is a glycoprotein, type I membrane protein (i.e. contains a single transmembrane domain) and class I viral fusion protein. It assembles as a homotrimer, and each monomer is comprised of two functionally distinct subunits. S1 is responsible for receptor recognition and binding, while S2 facilitates fusion between the viral envelope and the cell membrane. Fusion of the virus with the cellular or endosomal membrane is crucial for the delivery of its genetic material. Therefore, S presents several fusion peptides, which are regions of viral fusion proteins that mediate membrane fusion. Several membranotropic domains have been identified within S, all of which can act as functional fusion peptides and they probably do so synergistically.[50]

S presents two cleaving sites which are crucial for its infection cycle. The first one, the so-called furin cleavage site, is a polybasic site located at the S1-S2 junction, and is targeted by furin-like proteases of the host cell during biosynthesis and maturation at the Golgi. Despite the cleavage, the two subunits remain associated through non-covalent interactions.[15] The second priming site is the S2', located upstream of the fusion peptide, and is cleaved by plasma membrane-associated proteases such as TMPRSS2. After cleavage, the S1 subunit dissociates which induces a conformational change in S2. This exposes the fusion peptide which can insert into the cell membrane and initiate membrane fusion. If S is not cleaved by TMPRSS2, the virus can enter the cell through the endocytic pathway and will fuse with the endosomal compartment after cleavage by cathepsins.[15,51]

The acquisition of a furin-like protease-targeted site was beneficial for the fast and efficient spread of SARS-CoV-2. However, cleavage at the S1-S2 site leads to destabil-

isation of S and a premature postfusion conformation of the trimer. The shedding of S1 was rapidly circumvented by an aspartic acid (D) to glycine (G) mutation at position 614, D614G. Viruses harbouring the mutation rapidly became the predominant variant worldwide, only a few months since the start of the COVID-19 pandemic. This mutation did not only make the S1-S2 association stronger, but also increased viral infectivity and S density in the virion, while keeping ACE2 affinity unmodified.[52]

Despite the evidence, it is still controversial whether the cleavage of S at the furin site is essential for viral spread. Some report that, while the cleavage is not crucial, promotes viral infection and cell-to-cell fusion (i.e. cell syncytia) because it primes S for TMPRSS2 processing at the S2' site.[53] Syncytia formation occurs when a cell expressing S encounters a cell expressing ACE2, which will interact with each other and thus cell-cell fusion will occur. This mechanism is exploited by viruses to spread while avoiding antibody neutralisation.[47,54] This is further confirmed by the fact that an increase in fusion could be observed for SARS-CoV (in terms of syncytia formation) when a furin site was introduced at the S1-S2 boundary.[55] Another study points out that the acquisition of the polybasic cleavage site favours the plasma membrane entry route against the endosomal one, and hence the virus can skip inhibition by IFN-induced transmembrane (IFITM) protein 2, located in the endosomal compartment.[56]

The key factor that allowed the adaptation to humans of the virus remains elusive, although the acquisition of the furin site (followed by the D614G mutation) was suggested as essential for the zoonotic transfer to humans from bats. Increased affinity to ACE2 (and newly found interaction with rat and mouse ACE2 orthologues) in subsequent variants, such as Alpha, might also be a contributing factor.[15] Another example of broad tropism linked to the furin site has been observed in other coronaviruses. The avian infectious bronchitis virus (IBV) strain Beaudette presents a furin cleavage site and is able to infect a wide range of cell lines, an exception in its coronavirus group.[55].

Studying changes in affinity to cellular receptors, such as ACE2, or the appearance of new binding ones will give us insight on new targets to be tackled for viral spread control. In this thesis, focus will be laid on both Alpha and Omicron S variants and their interaction with ACE2 and other plasma membrane components.

## 1.2 The importance of lipids in the viral cycle

### 1.2.1 Lipids in the host cell membrane

Some lipidic components of the plasma membrane have been reported to be crucial for the viral cycle of many viruses, cholesterol being one of the most documented ones. Cholesterol is a sterol present in all animal cell membranes that constitutes up to 30 wt% of their lipid content.[57] It is an important part of lipid rafts, membrane microdomains rich in sphingolipids and cholesterol that concentrate proteins and other macromolecules, which can have an influence in signalling.[58] Cholesterol removal from the plasma membrane has been reported to disrupt the viral cycle of several viruses, from SARS-CoV to HIV, among others.[59,60] Specifically for SARS-CoV-2, several studies have demonstrated the effect of cholesterol depletion on its viral cycle, specifically during attachment and fusion.[61,62] The main receptor for the entry of SARS-CoV-2, ACE2, has been found to be associated to cholesterol-rich lipid rafts. The disruption of these microdomains by cholesterol removal with methyl-$\beta$-cyclodextrin (M$\beta$CD) reduced the infectivity of SARS-CoV-2 viral pseudotypes.[61] Cholesterol was also reported to be crucial for SARS-CoV-2 fusion, as its disruption reduced S-mediated membrane fusion *in vitro*.[62] Not only cholesterol is relevant in the viral infection process, sphingomyelin and its derivative ceramide play a role as well. Ceramide-rich membrane clusters have been proven to be entry sites for rhinoviruses, while disruption of ceramide production has been reported to affect the HIV biogenesis process.[63,64] As for SARS-CoV-2, the effect of these lipid species seems to be similar as that observed for rhinoviruses, in which a depletion of ceramide reduces viral infection.[65]

### 1.2.2 Lipids in the viral envelope

Viral lipid envelopes have a controlled composition, which partially correlates to the region of the plasma or organelle membrane they bud from. The lipid composition of the viral envelope is, in many cases, crucial for a successful viral entry and fusion into target cells, as well as for correct budding. Because of this, is it common that viral membranes are enriched in certain lipid species in comparison to the cellular membrane where they egress from. A study from 2015 analysed three different strains of influenza A virus and found a dominance of phosphatidylethanolamine (PE) as the major phospholipid component of the viral membrane, unlike in mammalian cells where phosphatidylcholine (PC) prevails.[66] Another well studied example is HIV, whose envelope is enriched in cholesterol, sphingomyelin (SM), phosphatidylserine (PS) and

PE.[67] A similar phenomenon was observed for SARS-CoV-2. Although the virus buds from the ERGIC, whose membranes do not contain ordered lipid domains, S drove the formation of ordered sphingolipid (SL) and cholesterol-rich domains. This lead to an overrepresentation of SL in the released viral particles in comparison to the host cell membrane. Disruption of the S-driven microdomains in the virions affected the fusion capability, and subsequently infectivity, of SARS-CoV-2 virions.[68]

Modifications of the composition of the budding membrane can lead in some cases to a failed viral particle formation. In the case of HIV, depletion of cellular cholesterol significantly reduced viral particle production.[69] This is consistent with the fact, that depletion of cholesterol content in HIV virions reduced their infectivity due to membrane permeabilisation, which affected the mature virion core integrity.[70] A similar approach was followed by blocking SL production in host cells. Opposite to what was reported for cellular cholesterol, the reduction in SL had no effect on viral particle release. However, HIV infectivity was strongly reduced.[71]

The impact of cholesterol removal from the plasma membrane is not uniform across all viruses. When depleting cellular cholesterol in influenza A-producing cells, an increase in viral particle release was observed. However, the released virus particles were less infectious than the ones stemming from untreated cells.[72] Similarly to HIV, cholesterol depletion from the influenza viral envelope also reduced the infectivity of the viral particles.[72,73]

Even though there are certain lipid species which are crucial to maintain the integrity and function of the virus, there are large variations in viral lipid envelope compositions. When comparing viral particles which replicated in distinct cell lines, various studies found differences in the envelope lipid composition. Examples of this are SARS-CoV-2 and HIV. SARS-CoV-2 viruses produced in A549 cells presented more phosphatidylinositol (PI) versus PC, in comparison to viruses stemming from Vero E6 cells.[74] PE was found to be enriched in HIV particles produced by MT-4, but not by HeLa cells.[67]

All of the aforementioned studies highlight the influence of the lipid envelope in the viral life cycle. Precise control over its composition often determines the fate of the infection. In the next section I will discuss the importance of synthetic biology and virology, and their contribution to virus research.

## 1.3 Synthetic biology

Synthetic biology enables the design and construction of biological systems with precise control over their functions, a feature which is often lacking in standard biology methods. Bottom-up and top-down synthetic biology are two approaches that attempt to simplify processes with the aim of understanding and reconstituting complex cellular mechanisms. Top-down strategies strive to minimise the complexity of an already existing macromolecule, organism or system. Bottom-up approaches, on the other hand, focus on reconstituting a specific biological function based on a minimal amount of well-defined components (Figure 1.2).[75]

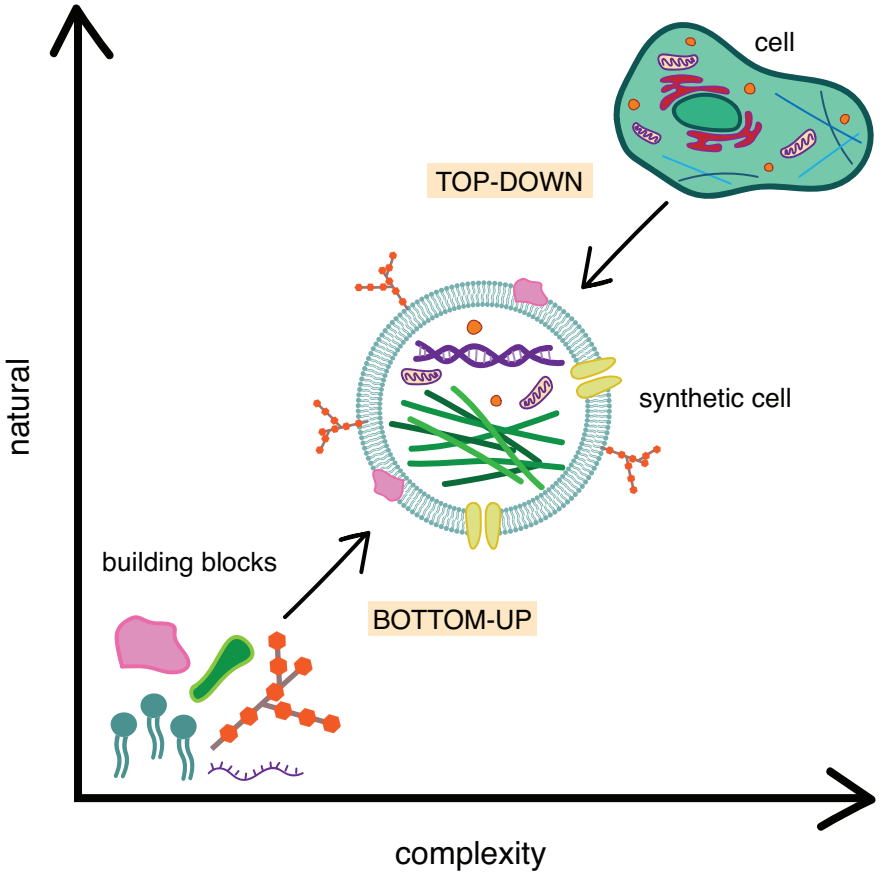


**Figure 1.2: Schematic illustration of the main concepts of bottom-up and top-down synthetic biology.** In bottom-up synthetic biology basic building blocks (genetic material, lipids, polysaccharides, proteins) are combined, usually inside a compartment, to recreate some cell-like feature. In top-down synthetic biology living cells are modified, or their complexity simplified, to produce cells with new functionalities. Figure adapted from Hirschi *et al.*[76]

### 1.3.1 Top-down synthetic biology

One of the main goals of top-down synthetic biology is to create a synthetic cell by modifying an existing living cell. This can be achieved by genome or protein modification. One well-known example is the minimal genome cell: JCVI-syn3.0. This bacterial cell has a genome which is smaller than that of any autonomously replicating cell found in nature and it is chemically synthesised *in vitro*.[77] This approach permits the distinction between essential and non-essential genes by studying the fitness of mutated cells. Genome reduction has not only been used for living cells, but also for bacteriophages. Using CRISPR/Cas9 the genome of 4 distinct bacteriophages was reduced up to 23%, which identified not only essential genes but also those involved in greater infectious efficiency.[78]

Understanding the function of each gene paves the way for designing synthetic cells tailored for specific purposes, such as drug or biofuel production. For example, an exogenous metabolic pathway was engineered into the yeast species *S. cerevisiae* to obtain an antimalarial drug at a higher productivity rate than the original drug-producing organism.[79] Additionally, several bacteria and yeast strains have been modified to produce fuels derived from different sources, from fatty-acids to alcohol.[80] Another usage of top-down synthetic biology is vaccine production. Toxins from *C. difficile* were modified to reduce their toxicity while retaining their immunogenic capacity, allowing them to serve as a vaccine.[81]

Aside from engineering cells to produce specific metabolites, cells can also be modified to be a treatment by themselves. This is the case for T cells, which can be genetically modified to target specific tumour antigens. As a result, T cells engineered to present chimeric antigen receptors (CAR T cells) are highly efficient to treat B-cell cancers and myelomas.[82]

One advantage of top-down synthetic biology is the availability of metabolites, pathways, co-factors and other elements found in a living cell that can be utilised. However, drawbacks are significant, including increased complexity as well as crosstalk between endogenous and synthetic systems, which is not always desired. Furthermore, using living cells as the starting point can come with the downfall of needing higher biosafety facilities for developing the research.[83]

### 1.3.2 Bottom-up synthetic biology

Bottom-up synthetic biology aims to reconstruct biological and chemical components by assembling functional building blocks of a natural or new-to-nature system. One main objective of synthetic biology is the creation of a fully autonomous and sustainable synthetic cell. For that goal to be reached, several biological features are required and need to be reconstructed, such as: compartmentalisation, energy supply, protein production, transport mechanism, metabolism, genetic material replication and division.[76] Among those, compartmentalisation and cell division are two aspects that are being extensively investigated.

Compartmentalisation is a feature shared by all living cells, achieved in most cases by lipid membranes. Therefore, lipid or polymer vesicles are a widely used component in many bottom-up synthetic biology approaches. Specifically cell-sized liposomes in the form of giant unilamellar vesicles (GUVs) serve as model membranes to study isolated cellular processes in a controlled environment. Many elements of the cytoskeleton, such as actin, myosin or microtubules, have been studied in such systems. One example is the investigation of actin organisation inside the cell, a crucial process in cell migration.[84] Also microtubules have been assembled inside GUVs and manipulated to assume cell-like geometries.[85]

Cell division is essential for the continuation of a population, and is an ongoing topic of investigation in bottom-up synthetic biology. A common approach is the use of rings made of actin and myosin, mimicking the contractile ring used by eukaryotic cells.[86] However, eukaryotic systems can be sometimes difficult to manipulate. Therefore, their prokaryotic homologs are often used instead. The *E. coli* machinery has been widely studied in the context of synthetic biology, specifically in terms of cell division. The Min protein system positions the bacterial cell division complex in the middle of the cell prior to division. It has been utilised alone or in combination with other cell division machinery to achieve synthetic liposome division.[87,88] A different approach substitutes cytoskeletal proteins for DNA-nanotechnology to create a synthetic cytoskeleton inside liposomes that resembles actin rings during cell division.[89]

As discussed previously, one advantage of bottom-up systems is the lack of crosstalk, toxic products and other unwanted metabolites that can be present in a top-down system. However, bottom-up approaches present a lower complexity which can limit their capabilities. Integration of different functional modules by sequential assembly thanks to precision technologies (e.g. microfluidics) will help produce more complex synthetic cells.[75] Despite their differences, sometimes top-down and bottom-up methods

can be combined. One hallmark of living cells is the ability to change their shape upon certain stimuli. This was achieved in liposomes by using pH-sensitive DNA origami, which was able to bind and deform the lipid membrane when pH increased. The proton gradients that modified the pH originated from top-down engineered *E. coli*, which was transformed to overexpress the exogenous xenorhodopsin, a light-driven proton pump.[90]

Aside from reconstructing cellular functions, there are other processes that can be investigated in bottom-up synthetic biology, such as viral cycles. Budding and fusion are essential events in the life cycle of a virus, and they have been investigated using the membrane of the GUV as a mimic of the cellular plasma membrane.[91] Moreover, GUVs as model membranes can be serve as a platform to study interactions of viruses with the lipid bilayer. One example of this is the study conducted by Stephan *et al*. These researchers achieved the asymmetric incorporation of *E. coli*'s lipopolysaccharides into the membrane of GUVs, which could be used as model bacterial membranes for antimicrobial drug studies.[92] All the aforementioned approaches highlight the potential of bottom-up synthetic biology in mimicking cell-like features in a controlled manner.

### 1.3.3 Cell-free protein synthesis

Many components used in bottom-up synthetic biology approaches are purified from living cells. The reliance on living cells and their inherent complexity presents challenges to synthetic biology, as recombinant protein expression and purification faces problems such as protein aggregation, inactivity and incorrect folding.[93] For example, one common problem of recombinant protein purification in yeast - a widely used organism for heterologous protein production - is degradation of the target protein.[94] These challenges can be overcome by cell-free synthetic biology, which utilises biological machinery without the use of living cells.[95] Even though cell-free systems can also be used to implement complex biochemical pathways, the most commonly known use is for coupled protein transcription and translation.

The necessary elements to perform cell-free protein synthesis (CFPS) can be obtained directly from a cell lysate or can be specific components isolated from the cell. The most common organisms used for obtaining a CFPS lysate are *E. coli*, *S. cerevisiae*, rabbit reticulocyte, wheat germ and insect cells.[95] They all present different protein production yields, being *E. coli* one of the most powerful ones.[96] The other CFPS strategy consists of a purified system containing a toolbox of necessary transcription

and translation components purified from *E. coli*, also known as PURE (protein synthesis using recombinant elements) system.[97] The PURE system allows for high purity and easy purification of the expressed protein. However, it is also considerably less productive compared to its lysate-based *E. coli* counterpart.[96]

The use of CFPS provides flexibility to the system, enabling specific modifications such as the incorporation of unnatural aminoacids or post-translational modifications. Although some of these modifications can also be performed in cells, using a CFPS platform avoids the challenges associated with living cells. For example, incorporation of unnatural aminoacids in cells often faces problems such as incorporation efficiency or cytotoxicity.[98] In research using GUVs as cellular compartment mimics, some of the necessary components can be produced *in situ* by CFPS. It is the case of a phospholipid synthesis pathway, which was reconstituted inside vesicles and demonstrated to be functional by production of two lipid species.[99] Moreover, the expressed proteins were either membrane-bound or integral membrane proteins. This provides an advantage to conventional methods of purification and vesicle insertion of membrane proteins, which require the use of detergents.

Commercially available S variants are usually modified to ease their purification from living cells or increase their stability. That is achieved by the addition of tags, such as the histidine tag, and a trimerisation domain to ensure S trimer stability.[100] Furthermore, they are often mutated to avoid cleavage by cell proteases.[101] Production of full-length S via CFPS provides flexibility of expressing the desired S variants without tags, mutations or stabilisation domains which might compromise its behaviour. The use of full-length S is important as it enables the study of how envelope lipid composition affects S and its binding affinity to ACE2, unlike tagged S, which is not integrated into the lipid membrane.

## 1.4 Synthetic virology

Synthetic virology is a branch of virology that sets out to recreate and manipulate natural viruses to study their properties or to engineer them for a specific purpose (e.g. vaccine development). It allows investigators to investigate aspects of the viral cycle while avoiding risks entailed by working with these dangerous viruses.[102] For example, producing non-infectious surrogate systems of Ebola virus allows research to be performed in biosafety level (BSL) 2 facilities, instead of BSL-4 needed to work with the natural infectious virus.[103] The type of information that can be obtained from such studies is double: on the one hand, one can use synthetic virology to investigate difficult

to cure or eradicate viral infections. On the other hand, one's aim can focus on better understanding the viral cycle and the underlying reasons for the characteristics of certain viruses. Moreover, synthetic virology also aims to use synthetic lab-made viruses for specific purposes, from drug delivery to vaccines.[104–106]

### 1.4.1 Top-down approaches

In top-down methods, natural viruses are modified to reduce their complexity, virulence, or to equip them with new characteristics. Two of the most common virus-derived structures are virus-like particles and pseudoviruses. Virus-like particles (VLPs) resemble their origin natural virus in terms of shape, external appearance and size, but they contain no genetic material rendering them non-infectious (Figure 1.3).[107] VLPs can be expressed and self-assembled in multiple cell types (e.g. plant, animal, bacteria) or produced using cell-free systems.[107–110] Gene therapy, drug delivery and vaccines are the three most common uses of VLPs. However, they are still time consuming and challenging to formulate, produce and purify.[107]

Pseudoviruses are viral particles coated with foreign viral envelope proteins. The most typical viruses used as packaging systems are HIV, vesicular stomatitis virus (VSV) and murine leukemia virus (MLV) (Figure 1.3). Unlike VLPs, they can carry genetic material but they lack the genes to replicate their own envelope proteins and often to complete a full replication cycle, which renders them nonpathogenic. When producing the pseudovirus, an additional plasmid to the one coding for the viral packaging system is transfected. This plasmid contains the gene coding for the heterologous envelope protein of the virus at study.[111]

The use of specific heterologous proteins allows the pseudovirus to target and enter cells containing specific receptors, while escaping the pathogenicity associated to the original live virus.[111] Pseudoviruses have been used to develop vaccines for different candidates, specially those against viruses that can only be studied in high BSL facilities, such as SARS-CoV-2, Nipah or Rabies viruses.[112–114]

Another strategy which is in the frontier between top-down and bottom-up approaches is the use of extracellular vesicles which present specific viral antigens, such as the spike from SARS-CoV-2 (Figure 1.3). Even though they might be easier to produce than enveloped-VLPs, their composition - both in terms of lipid and protein - cannot be completely controlled.[115]

Synthetic biology methods can also be applied to engineering bacteriophages. As mentioned in the previous section, genome reduction was performed in 4 distinct bacte-

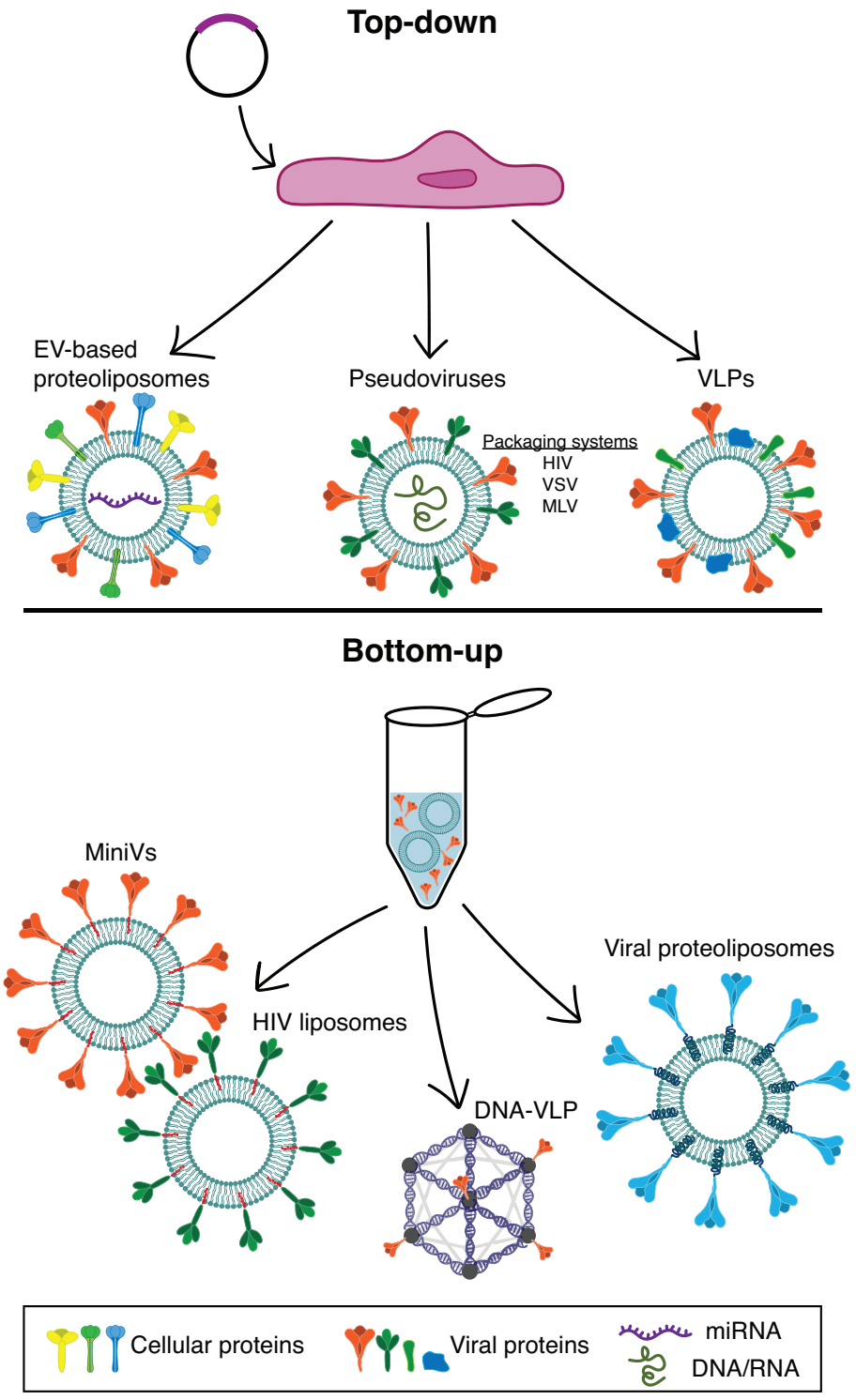


**Figure 1.3: Overview of most used top-down and bottom-up approaches in synthetic virology.** Top-down methods rely on cell transfection for the production of non-infectious viral particles, those being EV-based, pseudoviruses or VLPs. Bottom-up approaches combine purified viral proteins and a scaffold to mimic the external appearance of a natural virus. Typical scaffolds are liposomes or DNA origami.

riophages and their essential, quasi and non-essential genes were identified.[78] In addition to gaining insights into bacteriophage gene functions, top-down engineering of bacteriophages can be leveraged to enhance their antimicrobial activity. For example, genomes can be tuned to program host specificity or to regulate the antibacterial efficacy. Due to bacteriophages typically presenting very narrow host specificity, the host range is a common target to engineer. Modular swapping of phage tail components has allowed researchers to redirect the target host of several members of the T7 family.[116] It has also been accomplished for phages in the T2 and T4 families.[117]

### 1.4.2 Bottom-up approaches

Bottom-up methods for constructing viral particles have emerged more recently compared to the traditionally established top-down approaches. In order to mimic viruses that infect animal cells, the majority of which are enveloped, lipid vesicles can be used. These vesicles can be equipped with lipids which bind tagged- (histidine-, SNAP-, streptavidin-tag) proteins or can directly host transmembrane proteins. Several enveloped viruses have been mimicked by functionalising lipid vesicles with the putative viral surface protein. Examples of this are synthetic SARS-CoV-2 and HIV virions.[118,119] These synthetic viruses can be used with the aim to study aspects of the viral cycle in a safe and controlled environment. For example, synthetic SARS-CoV-2 virions were used to investigate the binding of fatty acids to the RBD, and its effects on virus-cell interactions.[118] Similarly, synthetic HIV liposomes - decorated with the envelope glycoprotein (Env) - were created with the aim to increase B cell activation (Figure 1.3). Env-functionalised liposomes induced a greater activation of B cells *in vivo* and *ex vivo* compared to soluble Env protein.[119] Both approaches allow for a deep and detailed study of virus-cell interactions and immune system activation, respectively, while simultaneously avoiding the risks and complications associated to handling the natural virus in high BSL facilities.

Other bottom-up approaches have been focused on producing liposome-based vaccines, which are based on vesicles functionalised with viral proteins on their surface. One example of this is liposome-displayed hemagglutinin, the major influenza virus surface protein, which was used as a vaccine and conferred protection to viral infection in mice.[120] A similar approach was developed to create a vaccine against SARS-CoV-2, conferring immunity to mice.[106] Some vaccines, however, do not use liposomes but lipid nanoparticles (LNPs) as scaffold, such as one of the COVID-19 mRNA vaccines.[121] Nevertheless, viruses that present surface proteins assembled in some type of symmetry, e.g. icosahedral, tend to be more challenging to replicate *in vitro*. One example of

this is the dengue virus, whose envelope protein assembles in sets of three, nearly parallel dimers, which might be difficult to self-assemble using his-tagged versions of the proteins.[122]

Even though the majority of methods rely on vesicle functionalisation of tagged-proteins, proteins can also be introduced into the lipid membrane tag-free. Proteins with transmembrane domains can be inserted directly into the vesicle membrane (Figure 1.3). This can be accomplished through cell-free simultaneous translation and reconstitution of the protein into liposomes.[123] An alternative method consists in the insertion of a detergent-protected protein, previously purified from living cells, into the vesicle membrane.[124] Both methods allow for a more natural presentation of the antigen, similar to the natural enveloped virus.[124]

Not all scaffolds are lipid-based; some make use of DNA to assemble nanoparticles that serve as platforms for antigen display (Figure 1.3).[125] Researchers designed and produced icosahedral DNA origami which later functionalised with the RBD of S. This DNA-VLPs were able to induce the production of protective neutralising antibodies to SARS-CoV-2, but none to the DNA scaffold.[126]

Non-enveloped viruses can also be designed and assembled from the bottom-up. Many studies have taken advantage of the high organisation of viral capsids that occurs through self-assembly, which has been observed for both eukaryotic and prokaryotic viruses (i.e. bacteriophages).[127] Specifically for bacteriophages, cell-free systems are widely used for the fast production and selection of different viruses, which can entail a big advantage to conventional bacteriophage production methods.[128–130]

Capsid protein self-assembly can also be used for the study of enveloped viruses, as a correct structure of the capsid is crucial for a successful viral replication cycle. As an example, two studies were able to produce synthetic hepatitis B virus capsids, one through chemical synthesis and another making use of a cell-free system.[131,132]

There are also approaches which benefit from the combination of bottom-up and top-down methods. Adenoviruses are non-enveloped viruses readily used for gene therapy. They can be packaged with up to 35 kb of genetic material and deliver it efficiently to a broad range of cell types. However, their tropism its limited to cells expressing the coxsackie and adenovirus receptor and they commonly induce hepatotoxicity.[133] In a study by Singh *et al*, adenoviruses were enveloped by self-assembled lipid bilayers. Modifying the composition of the lipid envelope led to control over the interaction with cells and transfection efficiency, as well as tumour penetration.[134] A similar approach was followed for bacteriophages, which were encapsulated in liposomes and

administered to poultry. The treatment increased protection in poultry over time against *Salmonella*.[135]

Overall, synthetic virology and specifically bottom-up approaches to mimic natural viruses provide safe and controlled research environments, which have proven to be highly valuable for the study of viruses.

# 2 Motivation

Since the start of the COVID-19 pandemic, there have been more than half a million SARS-CoV-2 studies published, often with contradicting results. Investigation of SARS-CoV-2, like many other viruses, is often challenging due to its complexity and variability. Furthermore, research can only be performed in high biosafety level facilities. These drawbacks can be overcome with bottom-up synthetic biology approaches that allow us to investigate complex mechanisms in a modular and simplified way. In the work presented in this thesis I aim to gain a better understanding of virus-cell interactions. I will implement bottom-up synthetic biology principles in order to design a modular bio-inspired synthetic version of the SARS-CoV-2 virus named MiniVs. The production of MiniVs involves the generation of small unilamellar vesicles with a similar lipid composition to the viral envelope and their functionalisation with the desired recombinant S variant. The produced synthetic viral particles have a similar size and charge to the natural SARS-CoV-2 virus. The use of MiniVs will give me the opportunity to investigate aspects of the SARS-CoV-2 viral cycle in detail, while remaining in a low biosafety environment. My research aims to contribute to this evolving field by studying the contribution of lipid species in the infectivity of the SARS-CoV-2 virus. Therefore, I will focus on the investigation of the following three major modules (Figure 2.1):

A. Affinity of recombinant SARS-CoV-2 S variants to ACE2 and lipid membranes (MiniVs - lipid membrane interactions)

B. Impact of the plasma membrane composition on SARS-CoV-2 S variant affinity (MiniVs - cell membrane interactions)

C. Functionalisation of vesicles with full-length transmembrane S (S proteoliposomes) and the analysis of the impact of proteoliposome lipid composition on S cellular affinity (proteoliposomes - natural cell interactions).

SARS-CoV-2 S variants differ in aminoacid residues and, in consequence, in surface charge and even affinity to their target ACE2 receptor. In the first module I will use Omicron and Alpha S to study the difference in ACE2 affinity and investigate their possible interaction with lipid membranes. Furthermore, I will investigate the contribution of specific components of the plasma membrane to the viral attachment. Finally, I will move from his-tagged recombinant S to a full-length transmembrane S with the aim to create S proteoliposomes. Due to S being inserted into the lipid membrane, I will be able to study the impact of certain lipid species on the insertion of S into the membrane and its affinity to ACE2.

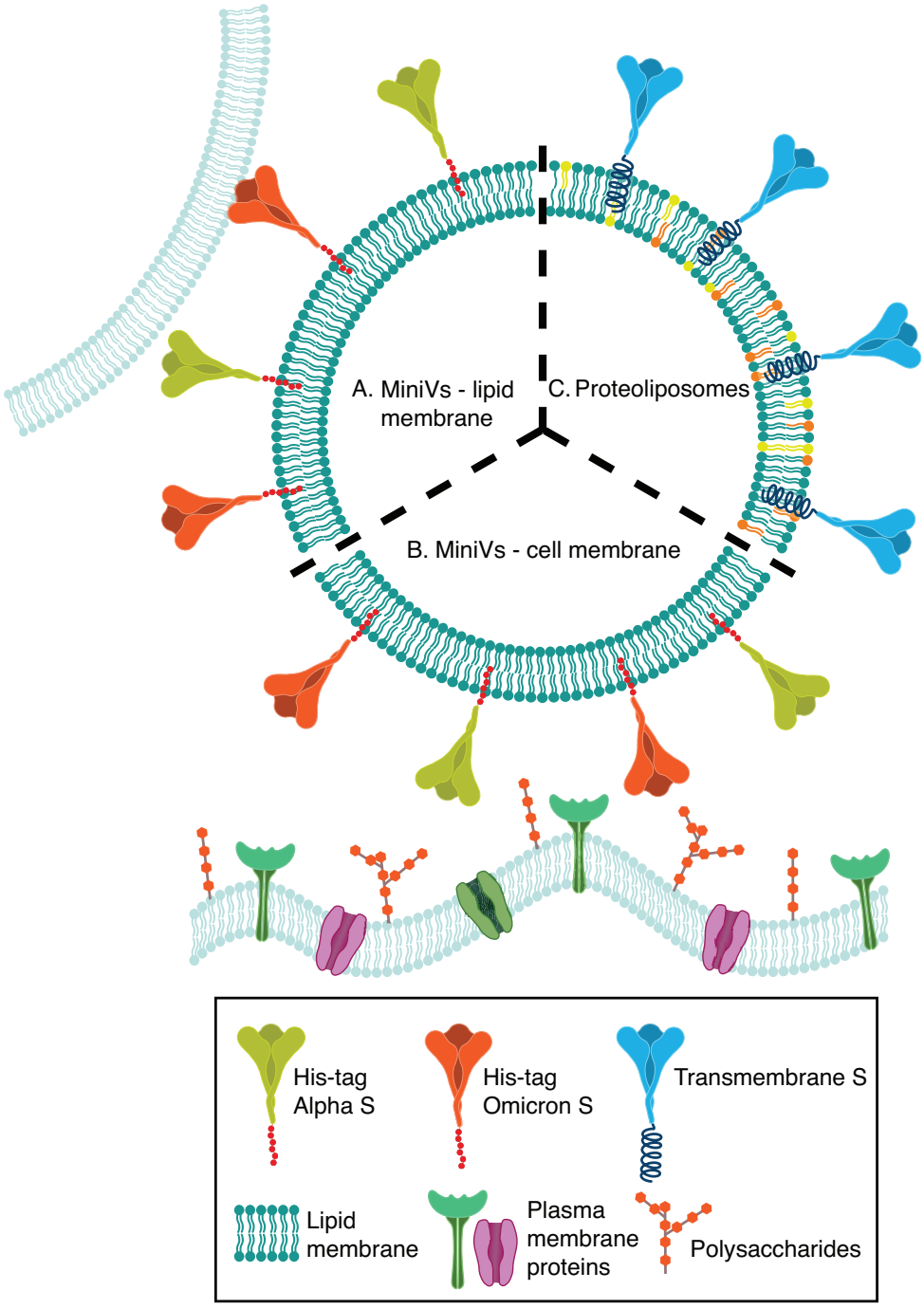


**Figure 2.1: Project overview.** Sketch of the three modules that will be investigated in this thesis. Module A is focused on the interaction between MiniVs and lipid membranes. Module B will put an emphasis on the elements of the cellular membrane that are important for the interaction with S variants. Module C will highlight the importance of specific lipid species on the viral envelope by producing S proteoliposomes.

# 3 Materials and methods

## 3.1 Materials

1,2-dioleoyl-sn-glycero-3-phosphoethanolamine-N-(lissamine rhodamine B sulfonyl) (ammonium salt) (18:1 Liss Rhod PE), cholesterol, 1,2-dioleoyl-sn-glycero-3-phosphocholine (18:1 (Δ9-Cis) PC, DOPC), 1,2-dioleoyl-sn-glycero-3-phosphoethanolamine (18:1 (Δ9-Cis) PE, DOPE), N-nervonoyl-D-erythro-sphingosylphosphorylcholine (24:1 SM), 1,2-dioleoyl-sn-glycero-3-phospho-L-serine (sodium salt) (18:1 PS, DOPS), 1,2-dioleoyl-sn-glycero-3-[(N-(5-amino-1-carboxypentyl)iminodiacetic acid)succinyl] (18:1 DGS-NTA($Ni^{2+}$), 1,2-dioleoyl-sn-glycero-3-phospho-(1'-myo-inositol) (ammonium salt) (18:1 PI, DOPI), 1,2-dioleoyl-sn-glycero-3-phospho-(1'-rac-glycerol) (sodium salt) (18:1 (Δ9-Cis) PG, DOPG), 1,2-dioleoyl-sn-glycero-3-phosphoethanol-amine-N-[methoxy-(polyethylene glycol)-2000] (ammonium salt) (18:1 PEG2000 PE) and extrude set with 50 nm and 100 nm pore size polycarbonate filter membranes were purchased from Avanti Polar Lipids, USA. Dulbecco's Modified Eagle Medium (DMEM) High Glucose, heat-inactivated fetal bovine serum, penicillin-streptomycin (10,000 U/ml), Stempro™ Accutase™ Cell Dissociation Reagent, Nunc™ Lab-Tek™ Chamber Slide System, Hoechst 33342, CellTracker™Green CMFDA , Alexa-Fluor405 tagged streptavidin and 1-Step Human Coupled IVT Kit - DNA were purchased from Thermo Fisher Scientific, USA. OptiPrep™ Density Gradient Medium, Silicone oil (viscosity 50 cSt), Mineral oil, Imidazole hydrochloride, Atto 647N DOPE, Atto 488 DOPE, Triton™ X-100, Sephadex® G-50, cholesterol-d7 and EquiSPLASH® were purchased from Merck, Germany. Human Angiotensin-converting enzyme 2 (ACE2) protein (His Tag), SARS-CoV-2 B.1.1.529 (Omicron) and B.1.1.7 (Alpha) S1+S2 trimer Protein (ECD, His Tag) and Anti-ACE2 Antibody (FITC), Mouse Monoclonal (10108-MM37-F) were purchased from Sino Biological, USA. Bio-Beads SM-2 Resin was purchased from Bio-Rad Laboratories, USA. QCM-D sensor crystals (QS-QSX303) were purchased from

Biolin Scientific, Sweden. FITC Mouse IgG1, $\kappa$ Isotype Ctrl Antibody (400107) was purchased from Biolegend, USA. SARS-CoV-2 Alpha and Omicron Spike Proteins in LMNG Detergent were purchased from Cube Biotech, Germany. PURExpress *In Vitro* Protein Synthesis Kit was purchased from New England Biolabs, USA.

## 3.2 SUV/MiniV preparation

Vesicles were produced by manual extrusion using track-etched membranes with the desired pore diameter size. First, stock lipids dissolved in chloroform were mixed to achieve the desired lipid composition (Table 3.1). If needed, 4 mol% of DOPC was substituted by 18:1 PEG2000 PE. The lipid mix was dried under vacuum for 15 min. The acquired lipid film was swelled in PBS to a final concentration of 6 mM and then shaken at 1000 rpm, 5 minutes each procedure. The obtained vesicle solution was extruded through a polycarbonate membrane with a pore diameter of 50 nm to achieve the desired vesicle size. His-tagged S was incubated with the vesicles for at least 1 h to obtain MiniVs. The final concentration of S was a sixth of DGS-NTA($Ni^{2+}$) lipid concentration (mol:mol) for QCM-D and GUVs experiments, and half for flow cytometry experiments.

**Table 3.1:** SUV control composition

| **Lipid** | **mol%** |
|---|---|
| DOPC | 45% |
| DOPE | 21% |
| Cholesterol | 14% |
| DOPI | 12% |
| DOPS | 3% |
| SM | 3% |
| Liss Rhod PE | 1% |
| DGS-NTA($Ni^{2+}$) | 1% |

## 3.3 S proteoliposome preparation

The proteoliposome protocol was adapted from Rigaud and Lévy and Lussier *et al.*[136,137] SUVs were produced with a specific lipid composition (84 mol% DOPC, 10 mol% DOPC, 5 mol% cholesterol and 1 mol% Atto 488 - DOPE) at a concentration of 6 mg/ml and average size of 100 nm. Vesicles were mixed with Triton X-100, at a final concentration of 0.4 mg/ml and 4 mM, respectively, to obtain a final volume of 950 $\mu$l. The solution was incubated at room temperature (RT) for 1 h. Next, the vesicle

solution was incubated with full-length Alpha or Omicron S at a final concentration of 0.73 mg/ml. Adding 50 $\mu$l of 0.73 mg/ml full-length S (Alpha or Omicron) achieved an approximate protein:vesicle (mol:mol) ratio of 80. After 1h incubation at RT, Bio-Beads SM-2 were added to the protein–lipid–detergent mixture at a Bio-Bead:detergent ratio of 20. Previously, Bio-Beads had been washed in methanol twice and resuspended in water. The protein-lipid-detergent solution was shaken for at least 2 h at 900 rpm and detergent removal was monitored by measuring absorbance at 200-700 nm. The protein fraction that did not insert into the vesicles, was removed by spin column filtration. Briefly, 1 g of Sephadex G-50 was swelled with 10 ml of MilliQ water and incubated for 1h at RT. The resin was loaded into a glass wool-plugged 5 ml syringe until it reached the 3 ml mark and centrifuged for 3 min at 1000 rcf. The proteoliposome solution was added on top, centrifuged for 10 min at 50 rcf and sequentially for 3 min at 1000 rcf. The eluted S proteoliposomes were collected and stored at 4 °C until needed.

## 3.4 Cell culture

Vero E6 and A549 cells were grown in Dulbecco's Modified Eagle Medium (DMEM) containing with 4.5 g/l glucose, 1% L-glutamine, 1% penicillin/streptomycin and 10% fetal bovine serum. Cells were cultured at 37 ºC and 5% $CO_2$ atmosphere and were passaged at 80% confluency using Accutase™ for detachment.

## 3.5 Flow cytometry

Cells in flask were detached with Accutase™ and centrifuged at 150 rcf for 5 min. Pellets were resuspended in 2% PFA and the cells were fixed for 10 min. Cells were centrifuged again for 5 min at 150 rcf to remove fixing agent.

### 3.5.1 MiniV affinity experiments

For MiniV affinity experiments, cells were counted and resuspended in flow cytometry (FC) buffer (PBS 1% BSA 0.1% $NaN_3$) to a final concentration of $5 \cdot 10^5$ cells/ml. Cells were distributed into single eppis and incubated for 1 h with SUVs, Omicron or Alpha MiniVs to a final concentration of 7 $\mu$M. For ACE2 quantification or inhibition experiments, cells were incubated in the dark for 1 h with FITC-conjugated anti-ACE2 antibody or Mouse IgG1, $\kappa$ Isotype antibody (used as an antibody isotype control) at a final concentration of 5 ng/ml. After the incubation time, cells were centrifuged at 4000 rcf for 5 min, the supernatant was discarded and the pellet was resuspended in FC

buffer.

### 3.5.2 Proteoliposome affinity experiments

For experiments with proteoliposomes, cells were counted and diluted in PBS to a final concentration of $1 \cdot 10^6$ cells/ml. Cells were distributed into single eppis and incubated for 1 h with SUVs, Omicron or Alpha proteoliposomes to a final concentration of $1.6 \cdot 10^{10}$ vesicles/ml. After the incubation time cells were centrifuged at 4000 rcf for 5 min and resuspended in desired buffer (FC buffer or PBS).

### 3.5.3 Plasma membrane modification experiments

In experiments in which the plasma membrane composition was modified, cells were first counted, incubated with the desired treatment and subsequently fixed. Cells were counted and diluted in PBS 0.5% BSA to a final concentration of $1 \cdot 10^6$ cells/ml. They were distributed into single eppis and incubated for 1 h with the chosen treatment (25-hydroxycholesterol, M$\beta$CD, SM, heparinase I or cholesterol), either in the incubator (37 ºC and 5% $CO_2$ atmosphere) or at RT in an eppi rotator. Stock solutions of 25-hydroxycholesterol, SM, M$\beta$CD and cholesterol were prepared in DMSO. Heparinase I was dissolved in MilliQ water. After the incubation time, cells were pelleted and fixed in 4% PFA for 10 minutes. Cells were centrifuged again at 400 rcf for 5 minutes, and resuspended in PBS. They were then distributed in wells and incubated with SUVs, Alpha or Omicron MiniV for 1 h. Finally, cells were pelleted again and resuspended in PBS.

In all cases, experiments were performed using the LSRFortessa and analysis was done using the FlowJo software (Becton Dickinson, USA).

## 3.6 Confocal microscopy

All images were obtained using a x63 immersion oil objective (Plan-Apochromat ×63/1.40 Oil DIC, Carl Zeiss AG, Germany) installed on the laser-scanning microscope LSM800 or LSM880 (Carl Zeiss AG, Germany). All microscopy images shown in this thesis were further analysed and adjusted using Fiji/ImageJ.[138]

## 3.7 Mass spectrometry of SUV composition

Mass spectrometry (MS) measurements were done in collaboration with Dr. Sebastian Fabritz. SUVs with a membrane composition suited for MS measurements were produced as explained above. For that reason, the mol% of cholesterol was doubled and no NTA-functionalised lipids were included in the formulation. Each experiment comprised two samples: one containing the unprocessed lipid solutions and another with redissolved lipids after vesicle formation. An internal standard (IS) mixture composed of Avanti's EquiSPLASH™ LIPIDOMIX® and cholesterol-d7 was used to spike all samples. Addition of IS is required for later correction of sample variability and lipid specific non-linear concentration-dependent effects. Acetonitrile (ACN) was used to dilute all samples to achieve final concentrations of 3 $\mu$M for lipids and steroids (see ratios in Figure 3.1), 0.3 $\mu$g/ml for cholesterol-d7 and 0.1 $\mu$g/ml for the EquiSPLASH™ mixture. Every sample set was produced and analysed three times. Ratiometric examination of lipid and steroid vesicle components was conducted using LC-MS/MS, specifically a Shimadzu Nexera UPLC (HILIC setup) hyphenated with a Sciex QTRAP 4500 triple quadrupole mass spectrometer. Additionally, a Waters XBridge Amide column (3.5 $\mu$m, 4.6 x 150 mm) operated at 35 ºC was incorporated in the LC system. From each final sample, 8 $\mu$l were injected on-column and elution was done using a solvent system composed of solvent A (50% v/v ACN, 50% v/v $H_2O$ supplemented with 10 mM ammonia acetate, adjusted to pH 8) and B (95% v/v ACN, 5% v/v $H_2O$ supplemented with 10 mM ammonia acetate). LCMS grade or higher was guaranteed for all solvents and additives used in these procedures. The used solvent concentration, as well as flow gradient parameters, are specified in Table 3.2. Specifically in the time period between 13 to 23 minutes, the flow rate was elevated up to 1 ml/min in order to ease a quick and efficient column cleaning and thus, avoid lipid carry-over. The solvent streams that derived from this increased flow rate were discarded.

Sciex Analyst 1.7.2 software was used to acquire data via multi reaction monitoring (MRM). The MRM parameters derived from MSM fragmentation were obtained through the infusion of the standard solutions into 50% v/v dichlormethane and 50% v/v methanol supplemented with 10 mM ammonia acetate, therefore inducing the appearance of adducts. Analysis of the samples indicated the presence of compounds with different ionizability stemming from their chemical composition. Thus, cholesterol presented an elevated limit of detection due to its single alcohol group attached to an aliphatic steroid structure as compared to, e.g., DOPG, which presents a quaternary and permanently charged amine. To solve this difference in ionizability, a segmentation

| Time (min) | Parameter | |
|---|---|---|
| **0.01** | Solvent B | 99.9 % |
| **1.5** | Solvent B | 99.9 % |
| **4** | Solvent B | 94 % |
| **10.5** | Solvent B | 40 % |
| **11.5** | Solvent B | 0 % |
| **13** | Total flow | 0.55 ml |
| **13.5** | Solvent B | 0 % |
| **13.5** | Total flow | 1 ml |
| **19.1** | Solvent B | 0 % |
| **19.2** | Solvent B | 99.9 % |
| **22.5** | Total flow | 1 ml |
| **23** | Total flow | 0.55 ml |
| **24.5** | Stop | - |

**Table 3.2:** UPLC solvent and gradient information. Adapted with permission from *ACS Nano* 2023, 17, 23913-23923. Copyright 2024 American Chemical Society.

of the MS method was implemented to allow simultaneous analysis of all compounds. The source temperature was lowered for the first segment, with the aim to enhance its ability to detect cholesterol. The sufficient retention time difference (>2.3 min) of cholesterol in comparison to other analysed lipid species made possible the decrease in temperature during the analysis, as it is relatively slow. Lipid analysis was performed on segment 2, which included polarity switching to accommodate the differences in ionizability of the lipid head groups. Negative ionisation mode was implemented for DOPC, despite showing a better response in the positive mode, to avoid detector saturation. Additional samples were measured in segment 3, in which MS starting conditions were reestablished. Figure 3.1 includes all the MS method parameters in detail.

Areas under the curve (AUC) for all analytes and their IS were obtained using the Sciex MultiQuant 3.0.2 software. The IS of each analyte was used to obtain its corrected AUC (triplicates) except for Liss Rhod PE, which did not have a corresponding IS. The coefficient of variations for the IS-corrected AUCs was <5% except for cholesterol, DOPS and DOPI, which was <15%. For data visualisation, a python script was written to calculate the ratio (in percentage) of lipid species in the final SUV solution (Equations 3.1-3.3).[139–144] $AUC_{lipid}$ corresponds to the AUC of every lipid species from the unprocessed lipid sample, while $AUC_{SUV}$ takes the corresponding ones from the SUV sample. $Percentage_{lipids}$ is the calculated ratios of lipid species present in the analysed sample.

**Experiment 1 (POS)**

| | | | | | | | | |
|---|---|---|---|---|---|---|---|---|
| **Segment 1** | Curtain gas (CUR) | 35 | ID | Chol-$NH_4$.1 | Chol-$H_2O$.2 | Chol-$NH_4$.IS-d7 | | |
| | Collision gas (CAD) | 9 | Q1 (Da) | 404.283 | 369.400 | 411.280 | | |
| | Source temperature (TEM) | 210 | Q3 (Da) | 369.400 | 147.300 | 376.400 | | |
| | Nebulizer gas (GS1) | 65 | Dwell | 120.000 | 50.000 | 100.000 | | |
| | Heater gas (GS2) | 70 | DP | 116.000 | 220.000 | 116.000 | | |
| | Ionization voltage (IS) | 5500 | CE | 15.000 | 29.000 | 15.000 | | |
| | Entrance Potential (EP) | 10 | CXP | 11.500 | 10.000 | 11.500 | | |
| **Segment 2** | Curtain gas (CUR) | 35 | ID | LissRhod | SM24 | SM-d9 | PE | PE-d7 |
| from 3.6 min | Collision gas (CAD) | 9 | Q1 (Da) | 1301.605 | 813.664 | 738.500 | 744.498 | 711.400 |
| | Source temperature (TEM) | 350 | Q3 (Da) | 682.000 | 184.100 | 184.000 | 603.500 | 570.500 |
| | Nebulizer gas (GS1) | 65 | Dwell | 30.000 | 30.000 | 25.000 | 25.000 | 25.000 |
| | Heater gas (GS2) | 70 | DP | 40.000 | 120.000 | 130.000 | 91.000 | 120.000 |
| | Ionization voltage (IS) | 5500 | CE | 67.000 | 37.000 | 37.000 | 33.000 | 30.000 |
| | Entrance Potential (EP) | 10 | CXP | 24.000 | 18.000 | 16.000 | 16.000 | 12.000 |
| **Segement 3** | Curtain gas (CUR) | 35 | ID | Chol-$NH_4$.1 | Chol-$H_2O$.2 | Chol-$NH_4$.IS-d7 | | |
| from 18.6 min | Collision gas (CAD) | 9 | Q1 (Da) | 404.283 | 369.400 | 411.280 | | |
| | Source temperature (TEM) | 210 | Q3 (Da) | 369.400 | 147.300 | 376.400 | | |
| | Nebulizer gas (GS1) | 65 | Dwell | 120.000 | 50.000 | 100.000 | | |
| | Heater gas (GS2) | 70 | DP | 116.000 | 220.000 | 116.000 | | |
| | Ionization voltage (IS) | 5500 | CE | 15.000 | 29.000 | 15.000 | | |
| | Entrance Potential (EP) | 10 | CXP | 11.500 | 10.000 | 11.500 | | |

**Experiment 2 (NEG)**

| | | | | | | | | | |
|---|---|---|---|---|---|---|---|---|---|
| **Segment 2** | Curtain gas (CUR) | 35 | ID | PC-OAc | PC-d7-OAc | PS | PS-d7 | PI | PI-d7 |
| from 3.6 min | Collision gas (CAD) | 9 | Q1 (Da) | 844.5 | 811.5 | 786.5 | 753.4 | 861.413 | 828.4 |
| | Source temperature (TEM) | 350 | Q3 (Da) | 281.3 | 288.3 | 281.3 | 288.3 | 281.3 | 288.3 |
| | Nebulizer gas (GS1) | 65 | Dwell | 25 | 25 | 30 | 25 | 25 | 25 |
| | Heater gas (GS2) | 70 | DP | -90 | -115 | -120 | -100 | -185 | -90 |
| | Ionization voltage (IS) | -4500 | CE | -54 | -50 | -55 | -56 | -60 | -60 |
| | Entrance Potential (EP) | -10 | CXP | -7 | -11 | -8.5 | -10 | -11 | -11 |

**Figure 3.1:** Source and MS parameters for the applied segmented LC-MS/MS (MRM) method. Segment 1 is optimised for measuring cholesterol at a low temperature with high dwell times (ms). Segment 2 involves increased temperature and polarity switching during the ionisation process to measure lipids. The parameters for lipid fragment transitions measured in positive ionisation mode are listed in the column labeled Experiment 1 (POS), while those for negative ionisation mode are provided in the column labeled Experiment 2 (NEG). Adapted with permission from *ACS Nano* 2023, 17, 23913-23923. Copyright 2024 American Chemical Society.

$$\frac{\mathrm{AUC_{lipid}}}{\mathrm{AUC_{lipid,\ IS}}} = \mathrm{AUC_{lipid,\ corrected}} \tag{3.1}$$

$$\frac{\mathrm{AUC_{SUV}}}{\mathrm{AUC_{SUV,\ IS}}} = \mathrm{AUC_{SUV,\ corrected}} \tag{3.2}$$

$$\frac{\mathrm{Percentage_{lipid}}}{\mathrm{AUC_{lipid,\ corrected}}} = \frac{\mathrm{Percentage_{SUV}}}{\mathrm{AUC_{SUV,\ corrected}}} \tag{3.3}$$

## 3.8 Mass spectrometry of cell-free *in vitro* translated S

MS measurements were done in collaboration with Dr. Sebastian Fabritz and Mrs. Tatjana Rudi. The SDS-PAGE band corresponding to the molecular weight of S was cut out and digested with trypsin. The sample was dried and dissolved in 15 $\mu$l of 10% ACN, 0.1% formic acid. Examination of peptides was conducted using LC-MS/MS, specifically a Bruker Daltonics maXis II ETD - high-resolution LC-QTOF (Bruker Daltonics, USA). Additionally, a BioResolve RP mAb, Polyphenyl column (450 A, 2.7 $\mu$m, 2.1 x 100 mm) was incorporated in the LC system. From the sample, 5 $\mu$l were injected on-column and elution was done using a solvent system composed of solvent A (water, 0.1% v/v formic acid) and B (ACN, 0.1% v/v formic acid). LCMS grade or higher was guaranteed for all solvents and additives used in these procedures. The used solvent concentration and flow are specified in Table 3.3. Pressure was set to a minimum of 0 and a maximum of 800 bar. Electrospray ionisation parameters were as follows: end plate offset 500 V, capillary 4 kV, nebuliser 2.8 bar, dry gas 10 l/min and dry temperature 250 ºC. Ion polarity was set to positive, mass range was defined from 100 to 200 m/z and spectra range to 4 Hz. BioPharma Compass 2023 software (Bruker, USA) was used to acquire all data and it was analysed following the peptide mapping protocol previously published.[145]

## 3.9 Cell imaging

Vero E6 and A549 cells were seeded in confocal-compatible 8-well chambers at a concentration of $5 \cdot 10^5$ cells/ml and were kept in the incubator overnight to form a monolayer. The next day, cells were first stained with Hoechst (1 $\mu$g/ml) and CellTracker Green CMFDA (20 $\mu$M) for 40 minutes and then fixed for 10 minutes using 2% PFA.

| Time (min) | Flow (ml/min) | Solvent A (%) | Solvent B (%) |
|---|---|---|---|
| **0.00** | 0.4 | 98 | 2 |
| **3.00** | 0.4 | 98 | 2 |
| **20.00** | 0.4 | 65 | 35 |
| **24.00** | 0.4 | 40 | 60 |
| **25.00** | 0.4 | 2 | 98 |
| **28.00** | 0.4 | 2 | 98 |
| **28.10** | 0.4 | 98 | 2 |

**Table 3.3:** LC-QTOF solvent and flow information.

Cells were washed with PBS and incubated with SUVs, Alpha or Omicron MiniVs at a final concentration of 7 $\mu$M for 1h. Before confocal imaging, cells were washed 3 times with PBS to remove all unbound vesicles.

In experiments using C-laurdan as a staining agent, cells had to be first treated with different amounts of cholesterol, 25-hydroxycholesterol or M$\beta$CD. In short, both cell lines were seeded in wells and kept overnight in the incubator as described above. The following day, cells were washed with PBS and cholesterol, 25-hydroxycholesterol or M$\beta$CD (stocks in DMSO) were added at the desired final concentration in PBS 0.5% BSA. Cells were incubated for 1h inside the incubator (37 ºC and 5% $CO_2$ atmosphere), washed and fixed for 10 minutes using 2% PFA. After fixation, C-laurdan (stock in DMSO) was added to a final concentration of 40 $\mu$M and incubated for at least, 30 minutes. Cells were then imaged using an excitation wavelength of 405 nm. Emission was recorded between 415-455 and 490-530 nm.[146]

## 3.10 GUV preparation

GUVs were produced using the previously described emulsion transfer protocol.[84,147,148] In brief, desired phospholipid species were mixed at a final concentration of 643 $\mu$M with mineral oil (1 ml) to create a lipid-in-oil solution, 400 $\mu$l of which was placed on top of an aqueous buffer solution (outer buffer) and left to rest for an hour to obtain a lipid monolayer. The rest of the solution was mixed with the inner aqueous phase (inner buffer) of the vesicle to create a water-in-oil emulsion. The emulsion was placed on the lipid monolayer and vesicles were obtained by centrifugation at 300 rcf for 3 minutes. The residual oil was removed and the GUVs were resuspended in the appropriate buffer. The phospholipid composition was 80% DOPC, 20% DOPG (mol:mol). DGS-NTA($Ni^{2+}$) was added by substituting 2.5 mol% DOPC when needed. When making positively charged GUVs, 20 mol% DOPG was substituted for DOTAP, and the

phospholipid mix was diluted in silicone oil instead of mineral oil. The inner buffer was composed of 20% 5-[acetyl-[3-[acetyl-[3,5-bis(2,3- dihydroxypropylcarbamoyl)-2,4,6-triiodo-phenyl]amino]-2-hydroxy-propyl]amino]- N,N'-bis(2,3-dihydroxypropyl)-2,4,6-triiodo-benzene-1,3-dicarboxamide (OptiPrep) in PBS. SUVs or MiniVs were added to the inner buffer at a final concentration of 80 $\mu$M when needed. In experiments with ACE2, the his-tagged protein was added to the inner or outer buffer at final concentrations of 0.12 $\mu$M and 0.3 $\mu$M, respectively. The outer buffer was composed of 5 mM imidazole-HCl buffer, sucrose (added at a concentration that matched the osmolarity of the inner buffer) and MilliQ water (in 500 $\mu$l). PBS was used as an outer buffer in MiniVs competition assays.

## 3.11 QCM-D

Four $SiO_2$-coated sensors (QSX 303, Biolin Scientific, Sweden) were incubated under $O_3$ and UV atmosphere for, at least, 10 minutes. The sensors were loaded into the open module teflon chambers and placed in the QCM-D machine (QSense Analyzer, Biolin Scientific, Sweden). The shifts in resonance frequency and energy dissipation were simultaneously recorded across multiple harmonics. In each step, the volume added to each sensor surface was always 200 $\mu$l. First, the four sensors were calibrated for 5 minutes by adding PBS to the surface. To form the SLB, SUVs (78 mol% DOPC, 20 mol% DOPG, 2 mol% DGS-NTA($Ni^{2+}$) were diluted in PBS to a final lipid concentration of 1.2 mM, added to the sensor surface and incubated for 30 minutes. Previously, vesicles were produced by swelling the dry lipid film with a 10 mM $MgCl_2$ solution and subsequent extrusion through a 100 nm pore radius membrane. SUVs absorb and eventually rupture when in contact with the activated $SiO_2$ surface. The SLB formation process was monitored by observing changes in frequency and energy dissipation curves, as previously described.[149] The sensors were washed with PBS and a solution containing 300 mM his-tagged ACE2 was added to sensors 1, 2 and 4. After 15 minutes incubation, the sensors were washed again with PBS. MiniVs at a final concentration of 40 $\mu$M were added to sensors 1 and 3, a solution of 40 $\mu$M SUVs was added to sensor 2 and a solution containing 30 nM S was added to sensor 4. All surfaces were incubated with the respective solutions for 2 hours or until a plateau in the frequency and energy dissipation curves was reached. Ultimately, all sensors were washed with PBS and left to equilibrate for, at least, 10 minutes.

$K_D$ values were calculated by applying the Hill equation with the assumption of no cooperativity, using GraphPad Prism version 9.4.1 for Mac OS X. The same program

was used to perform an unpaired t-test on the mean values for frequency and energy dissipation.

## 3.12 SUV characterisation

SUVs were characterised in terms of concentration, size and zeta potential using Nanoparticle Tracking Analysis with the ZetaView® QUATT (Particle Metrix, Germany). First, an alignment was performed using 100 nm polystyrene beads diluted 1:250,000 (v/v) in MilliQ water. Vesicles were diluted in MilliQ water to a final concentration of 60 nM. When measuring proteoliposomes, the vesicle solutions were diluted 1:10,000 (v/v). Before sample injection, MilliQ water (at least 20 ml) was used to equilibrate the observation cell. All 11 positions of the observation cell were included to perform the Nanoparticle Tracking Analysis. The parameters used in all experiments were the following: scatter mode (488 nm laser), temperature of 24 °C, minimal brightness 30, minimal area 10, maximal area 1000, trace length 15, sensitivity 80, frame rate 15 and shutter 100. The continuous mode was used during zeta potential measurements, as the conductivity of the medium - MilliQ water - was lower than 2 mS/cm. Sensitivity was decreased to 70 when vesicles were diluted in DMEM.

## 3.13 Spectroscopy measurements of laurdan

Eight populations of SUVs were prepared as detailed in section 3.2. The standard population was based on the SUV control composition (see Table 3.1) substituting DOPI for DOPC, due to its low availability. From that composition, cholesterol, SM and DOPS were removed or doubled in concentration to form another seven SUV variations. LissRhod PE was excluded from all vesicle populations so that its fluorescence emission would not interfere with that of laurdan. The emission spectrum of laurdan inserted into SUVs of different composition was recorded using the FP-8600 NIR spectrofluorometer (JASCO, Japan). SUVs were measured in PBS at a final lipid concentration of 6 mM and final laurdan concentration of 30 $\mu$M (0.5% final lipid concentration). Previously, a stock solution of laurdan in DMSO was prepared. Excitation was set to 374 nm and emission intensity was recorded every 4 nm, from 405 to 601 nm. General polarisation (GP) values were calculated as follows, as previously described[150]:

$$GP = \frac{I_{440}\text{-}I_{490}}{I_{440}\text{+}I_{490}} \tag{3.4}$$

## 3.14 Molecular cloning by Gibson assembly

To obtain an adequate plasmid for expression with the 1-Step Human Coupled IVT Kit (Thermo Fisher Scientific, USA) I first selected a plasmid that contained his-tagged full-length Wuhan S (pGBW-m4136458 was a gift from Ginkgo Bioworks, USA, and Benjie Chen). The gene corresponding to S was subcloned into the provided plasmid from the IVT kit (pT7CFE1) by Gibson assembly using the Gibson Assembly Master Mix (New England Biolabs, USA).

The final plasmid was transformed into DH5$\alpha$ *E. coli* (New England Biolabs, USA) cells. Single clones were cultured in lysogeny broth (LB) medium containing 100 µg/ml ampicillin. Plasmids were isolated using the QIAprep Spin Miniprep Kit (Qiagen, Germany), their concentration was measured and they were stored at -20 °C until used for cell-free protein expression.

## 3.15 Cell-free expression

The Gibson-assembled plasmid containing the gene coding for full-length S was used for expression using human *in vitro* expression system (1-Step Human Coupled IVT Kit, Thermo Fisher Scientific, USA) or *E. coli*-based *in vitro* protein synthesis kit (PURExpress, New England Biolabs, USA). In both cases, the protocol provided by the manufacturer was followed.

# 4 Results and discussion

## 4.1 MiniV characterisation

Small unilamellar vesicles (SUVs) were produced with a lipid composition resembling that of the ERGIC, the budding site of the SARS-CoV-2 virus (Table 3.1).[25,118] Additionally, DGS-NTA($Ni^{2+}$) and fluorescently labelled lipids were added for biofunctionalisation and labelling of the vesicles, respectively. To ensure that all desired lipid species were found in the final vesicle population, a mass spectrometry assay was developed and implemented. All lipid types were present in the measured samples, with a small enrichment of SM at the expense of DOPE (Figure 4.1A). His-tagged Omicron and Alpha S were bound to the vesicle membrane via NTA($Ni^{2+}$)-functionalised lipids to obtain Omicron and Alpha MiniVs, respectively. The size of both types of MiniVs increased significantly compared to naked SUVs, which is expected given that the size of S is estimated to be around 10 nm.[151] MiniVs presented a peak at around 110 nm, which is in the size range of the natural SARS-CoV-2 virus (Figure 4.1B).[151,152] Surface charge was slightly more positive for MiniVs when compared to SUVs (Figure 4.1C). Both Alpha and Omicron MiniVs presented a negative zeta potential, similar to SARS-CoV-2.[153]

The differences in surface charge between S variants were observed by displaying their crystal structures from the Protein Data Bank (PDB). For that purpose, the Adaptive Poisson–Boltzmann Solver (APBS) software and PyMol (The PyMOL Molecular Graphics System, Version 2.0 Schrödinger, LLC.) were used to exhibit the electrostatic potential surfaces of Omicron (PDB 7WK2) and Alpha (PDB 7LWS) S (Figure 4.2).[154] As previously reported, the surface of Omicron S, specially around the RBD, showed a more positively charged surface in comparison to Alpha.[155]

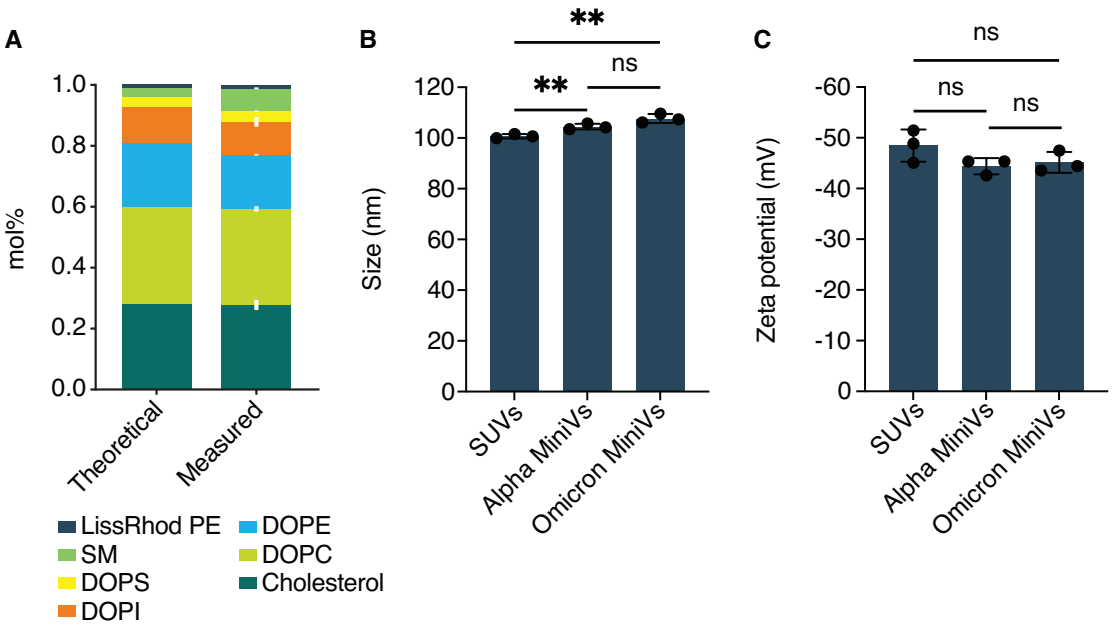


**Figure 4.1: SUV and MiniV characterisation.** A) Theoretical and measured lipid composition of SUVs by mass spectrometry. B) Size of SUVs and MiniVs measured by nanoparticle tracking analysis. C) Zeta potential values of SUVs and MiniVs obtained by dynamic light scattering in MilliQ water. Results correspond the mean ± SD from n = 3 biological replicates in each experimental condition. $**p < 0.005$, n.s. not significant, analysed using an unpaired two-tailed t-test. Adapted with permission from *ACS Nano* 2023, 17, 23913-23923. Copyright 2024 American Chemical Society.

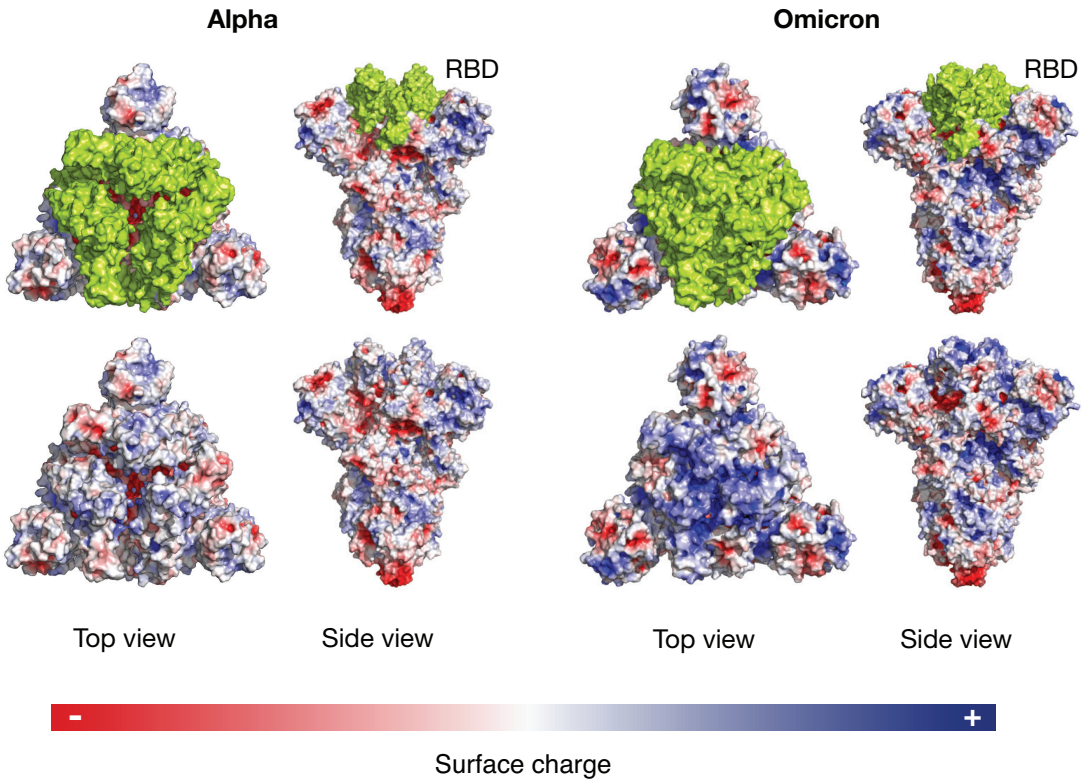


**Figure 4.2: Surface charge of Omicron and Alpha S.** APBS software was used to calculate the surface charge of both S variants, which were displayed in Pymol. RBDs (residues 319-541) are highlighted in green. Adapted with permission from *ACS Nano* 2023, 17, 23913-23923. Copyright 2024 American Chemical Society.

## 4.2 Omicron MiniVs affinity to SLBs on QCM-D

Quartz Crystal Microbalance with Dissipation monitoring (QCM-D) was used to demonstrate the ability of Omicron and Alpha S to bind to the ACE2 receptor. QCM-D is a sensor-based sensitive technique for analysing real-time changes in a surface. The sensor is made up of a thin quartz crystal disk linked to electrodes. By applying a voltage, the crystal can be excited and will start vibrating at a certain frequency. Furthermore, because the crystal oscillates due to an external force, changes in the surface that modify its oscillation can be monitored as energy loss or dissipation. A QCM-D experiment gives us information about changes in crystal thickness (mass) and viscoelasticity of the surface by monitoring frequency and energy dissipation, respectively.[156]

The setup used here has four sensors, which allowed me to compare several conditions (C1-C4) simultaneously (Figure 4.3A). First, a supported lipid bilayer (SLB) was formed on the surface by adsorption and immediate rupture of negatively charged SUVs (section 1 in Figure 4.3B). This was confirmed by an increase and quick decrease of energy dissipation, and the opposite for frequency, as was previously described for SLB formation.[149] The SLB had NTA($Ni^{2+}$)-tagged lipids, which allowed for functionalisation with his-tagged ACE2 receptor (section 2 in Figure 4.3B) in three of the sensors (C1, C2 and C4). This binding of ACE2 led to a mild increase in energy dissipation and decrease in frequency for the aforementioned conditions. In one last step, MiniVs (C1 and C3), SUVs (C2) and soluble S (C4) were added to their respective sensor (section 3 in Figure 4.3B).

SUVs did not interact with the SLB or the ACE2 receptor, yielding no changes in either of the two parameters monitored (C2). As shown in C1 and C4, both Omicron and Alpha S (as part of MiniVs or in their soluble form) were able to strongly bind to the ACE2 receptor, as indicated by an increase in energy dissipation and a decrease in frequency. Changes in energy dissipation and frequency indicate modifications of the viscoelasticity of the monolayer and of mass adsorbed to the monolayer, respectively.[157] In this case, an increase in energy dissipation demonstrates that S is not a rigid protein, but rather brings water molecules to the monolayer, and that it is adsorbed to the SLB via its interaction with the ACE2 receptor. Furthermore, the affinity of Omicron S appeared to be significantly greater to that of Alpha S (C1 and C4), confirming what had been previously documented (Figure 4.4).[24,158] Specifically, the dissociation constant ($K_D$) for Omicron S binding to ACE2 is reported to be half that of Alpha S, with values of 5.5 nM and 11.8 nM, respectively.[31]

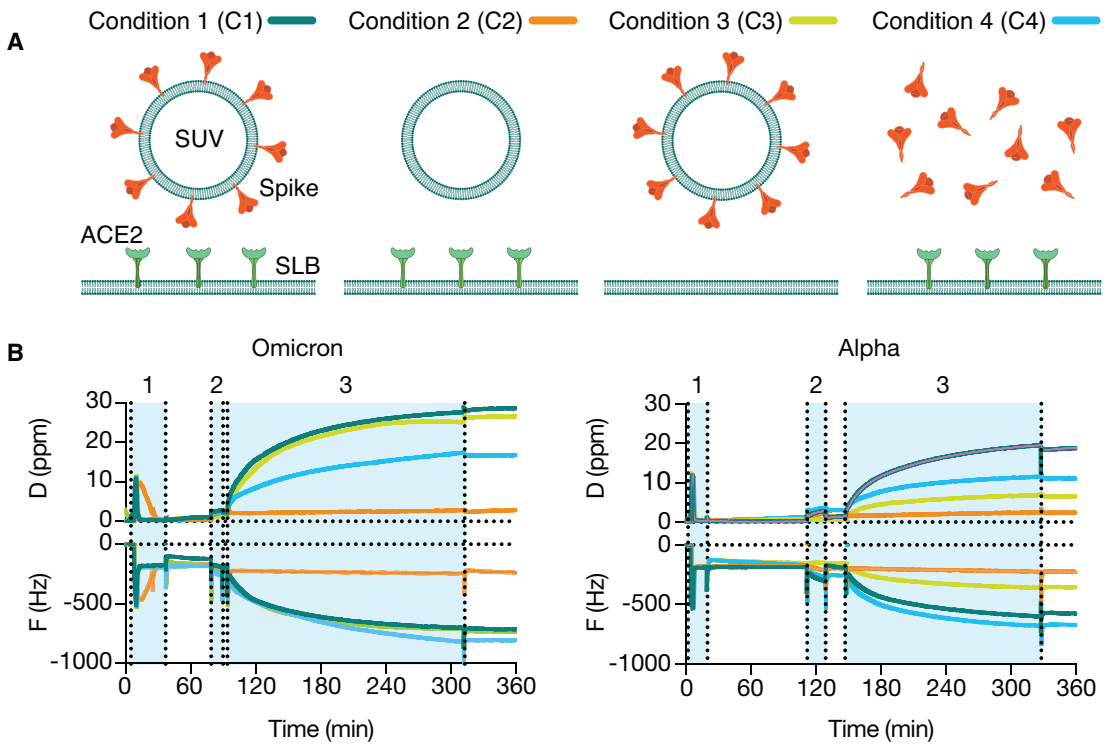


**Figure 4.3: QCM-D experiment with Alpha and Omicron MiniVs.** A) Schematic illustration of the conditions (C1-4) used in the QCM-D experiment. B) Representative QCM-D experiment of Omicron (left) and Alpha (right) S binding to an ACE2-functionalised SLB. Sections highlighted in blue correspond to: 1. SLB formation, 2. Addition of ACE2 receptor, 3. Addition of SUVs, MiniVs or soluble S. D is dissipation and F is frequency. Adapted with permission from *ACS Nano* 2023, 17, 23913-23923. Copyright 2024 American Chemical Society.

Since the appearance of the first studies investigating the Omicron variant, there have been reports of the protein having binding co-factors, independently of the ACE2 receptor, such as polysaccharides.[155] Interestingly, Omicron MiniVs were able to produce a significant response in the absence of ACE2 by interacting with the SLB, which was not observed for Alpha MiniVs (C3) (Figure 4.4).[158] This pointed to a newly discovered affinity of Omicron S to lipid membranes, which had been hypothesised and shown *in silico*, but never *in vitro*.[159]

To further confirm the previously discussed results, I decided to test the opposite QCM-D experiment setup. For that purpose, I functionalised the SLB with either Omicron (C1, C2) or Alpha S (C3, C4) and studied their interaction with naked or with ACE2-decorated SUVs (Figure 4.5A). Similarly to the previous results, Omicron showed a higher affinity to the ACE2 receptor than Alpha (C1 and C3, respectively, in Figure

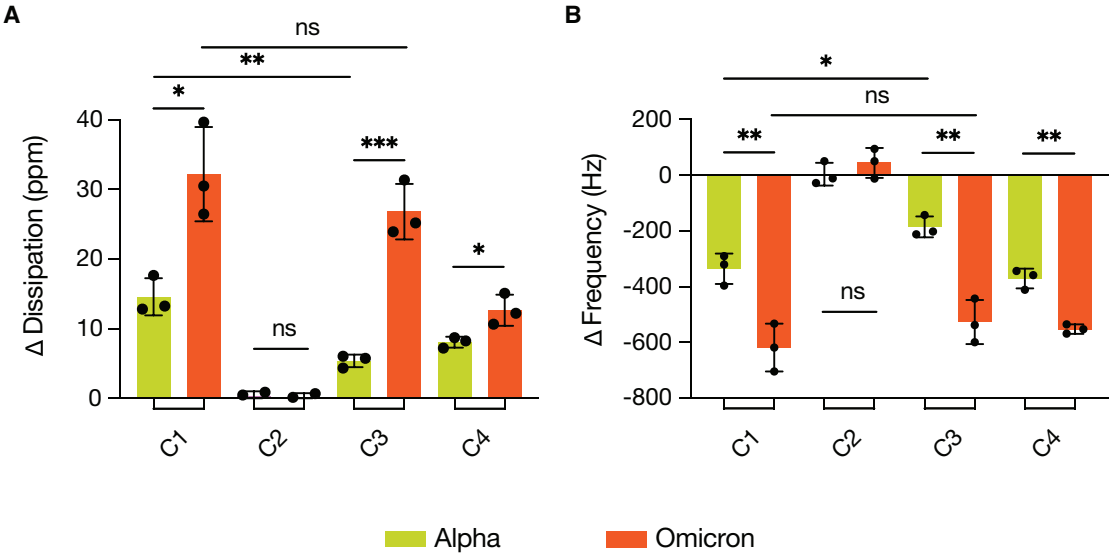


**Figure 4.4: Quantification of QCM-D experiments with Alpha and Omicron MiniVs.** Quantification of energy dissipation (A) and frequency (B) changes in all conditions (C1-4). Results correspond to the mean ± SD from n = 3 biological replicates. $*p < 0.05$, $**p < 0.005$, $***p < 0.001$, n.s. not significant, analysed using an unpaired two-tailed t-test. Adapted with permission from *ACS Nano* 2023, 17, 23913-23923. Copyright 2024 American Chemical Society.

4.5B). Consistent with earlier QCM-D data, there was almost no change in energy dissipation or frequency in C4, indicating no interaction between Alpha S and the naked SUVs. In contrast, Omicron S on the SLB showed strong interaction with the unfunctionalised SUVs (C2, Figure 4.5B).[158]

I set out to quantify the affinity of soluble Omicron and Alpha S to lipid membranes, in this case to an SLB. For that purpose, I developed a new QCM-D experiment consisting of only an SLB to which increasing concentrations of either variant of S were added. The SLB, just as in the previous experiment, was negatively charged as the cell membrane. I plotted the protein concentration against the recorded frequency delta and analysed it using a nonlinear regression and the Hill equation for specific binding. The formula used for equilibrium dissociation constant ($K_D$) determination is the following:

$$F = \frac{F_{max} C^h}{K_D{}^h + C^h} \tag{4.1}$$

In which F is frequency, $F_{max}$ is the maximum specific frequency (binding), C is concentration of S, $K_D$ is the concentration of S needed to achieve a half-maximum frequency at equilibrium and h is the Hill slope. Because there is no cooperativity, h was set to 1. The calculated $K_D$ indicated that the affinity of Omicron S to lipid

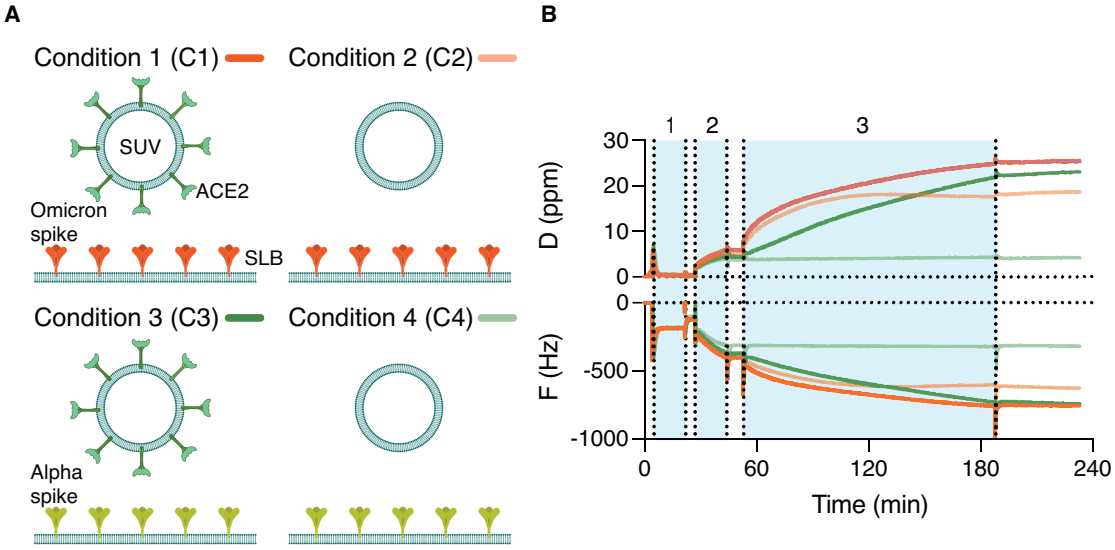


**Figure 4.5: QCM-D experiment of Omicron and Alpha S binding to ACE2-decorated SUVs.** Schematic illustration of the conditions (C1-4) used in the QCM-D experiment (A) and QCM-D experiment of Omicron and Alpha S-functionalised SLBs binding to ACE2-decorated SUVs (B). Areas highlighted in blue correspond to: 1. SLB formation, 2. Addition of Omicron or Alpha S, 3. Addition of SUVs or ACE2-decorated SUVs. D is dissipation and F is frequency. Adapted with permission from *ACS Nano* 2023, 17, 23913-23923. Copyright 2024 American Chemical Society.

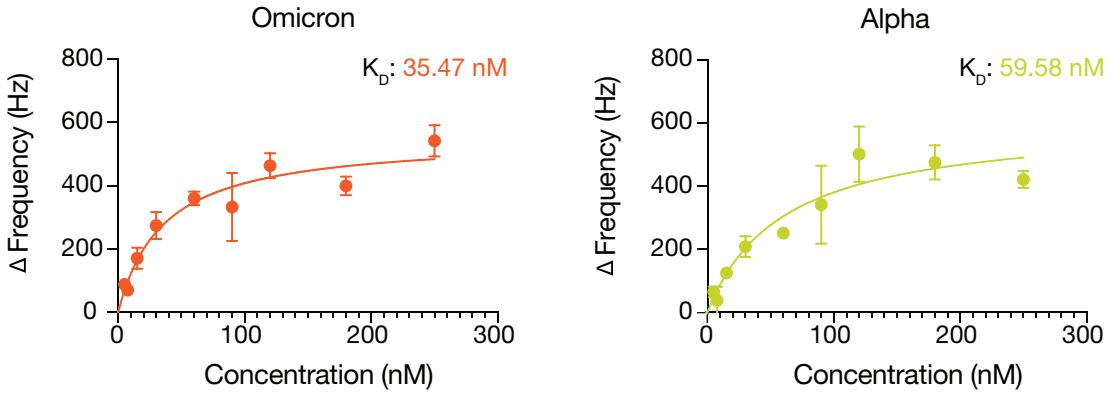


**Figure 4.6: $K_D$ determination of Omicron and Alpha S in contact with a negatively charged SLB.** Frequency change recorded by QCM-D at increasing concentrations of Omicron (left) or Alpha (right) S in contact with a negatively charged SLB. Adapted with permission from *ACS Nano* 2023, 17, 23913-23923. Copyright 2024 American Chemical Society.

membranes is twice as strong as the one of Alpha S (Figure 4.6).[158] However, the affinity was still not as strong as that to ACE2, according to literature.[31]

Despite lower than Omicron S, Alpha S showed an affinity for the negatively charged SLB when performing the $K_D$ determination experiments (Figure 4.6). This is in contrast to

the previous results displayed in Figure 4.3 and Figure 4.5, where the interaction between Alpha S and the unfunctionalised SLB/SUVs was almost negligible. One explanation for this discrepancy could be that I only used the soluble version of the protein when performing the QCM-D experiments for the determination of the $K_D$. By using the soluble and not the MiniV version of Alpha S, I lost the directionality provided by functionalisation of S to vesicles. Because of this, there could be new binding sites of S that were exposed and able to interact with the SLB.

Aside from studying lipid affinity, MiniVs have recently been used to study the difference in affinity between S variants and heparan sulfate molecules.[160] Additionally, similar approaches to MiniVs have been developed. For example, by using extracellular vesicles (EVs) which incorporate S into their membrane instead of SUVs.[115] Although the size might be similar, EVs cannot be unrestrictedly modified like MiniVs, and will have a lipid and protein composition which is dependent on the host cell they bud from. Moreover, EV populations tend to be heterogeneous which challenges reproducibility of experiments.[161] Other types of non-infectious approaches have been used to study the SARS-CoV-2 virus, from pseudoviruses to VLPs.[162,163] These last methods can provide insights into more complex aspects of the viral cycle, e.g. the role of membrane and envelope proteins for efficient production and release of the virus. However, and similarly to the EV approach, the protein and lipid composition of these particles cannot be as extensively controlled as that of MiniVs. Moreover, using these approaches the unique contribution of S cannot be investigated, as done here, due to the other proteins (membrane and envelope proteins) being present in the viral envelope.

## 4.3 Omicron MiniVs affinity to GUVs

To better mimic the 3D geometry of a cell membrane, I next used GUVs to test the affinity of Omicron and Alpha MiniVs towards their membrane. For that purpose, I used the emulsion transfer method to create vesicles with the same composition as the SLB previously used and incubated them in the presence of SUVs or MiniVs. It is important to mention that, in all experiments using both GUVs and SUVs/MiniVs, only the SUVs and MiniVs contained fluorescently labelled lipids. With this one can ensure that all recorded interactions, which are based on the fluorescence signal, do not stem from fluorescent excitation crosstalk or emission bleed-through.

First, I created GUVs and encapsulated either Alpha or Omicron MiniVs on the inside. For some experiments, his-tagged ACE2 was coencapsulated to serve as a positive control. In such experiments, NTA($Ni^{2+}$)-tagged lipids were included in the GUV

composition so that the inner part of the vesicle could be functionalised with ACE2. When the receptor was present, both Alpha and Omicron MiniVs bound to it and formed a visible corona all around the vesicle (Figure 4.7A). Surprisingly, in experiments where no ACE2 was added, both variants were able to interact with the membrane, contradicting the previous QCM-D results. It is important to be noted, that residual fluorescence stemming from the labelled Alpha MiniVs could be observed in the lumen of the not-ACE2-functionalised GUVs (Figure 4.7B). This points to a lower affinity of Alpha S to lipid membranes, as observed in the $K_D$ determination experiment (Figure 4.6).

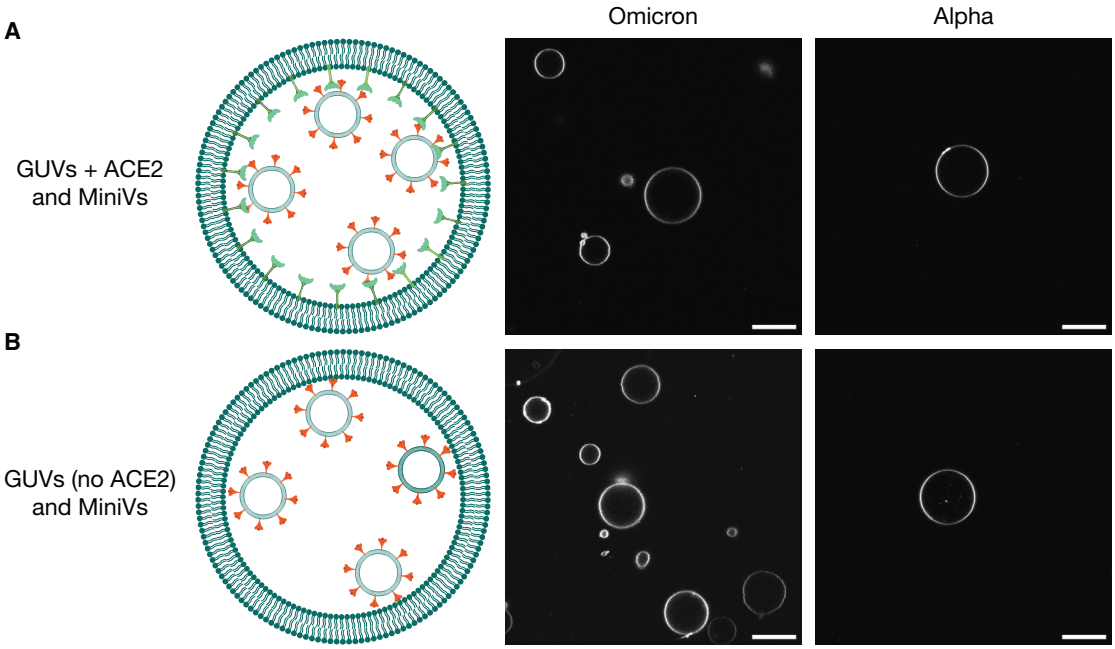


**Figure 4.7: Encapsulation of MiniVs in GUVs.** Representative confocal microscopy images of fluorescently labelled Omicron (left) and Alpha (right) MiniVs (1% Liss Rhod PE) encapsulated in GUVs alongside the ACE2 receptor (A) or alone (B). All scale bars are 20 $\mu$m. Adapted with permission from *ACS Nano* 2023, 17, 23913-23923. Copyright 2024 American Chemical Society.

To ensure that the membrane affinity was S-specific, I then encapsulated naive SUVs in GUVs. To make sure that no other protein used in the system interacted with the GUV membrane, I also functionalized SUVs with ACE2 and encapsulated them inside GUVs. Neither of them interacted with the membrane (Figure 4.8), which proved that the previous observed corona on the inside of the GUVs was induced by the interaction between S and the membrane (Figure 4.7B).[158]

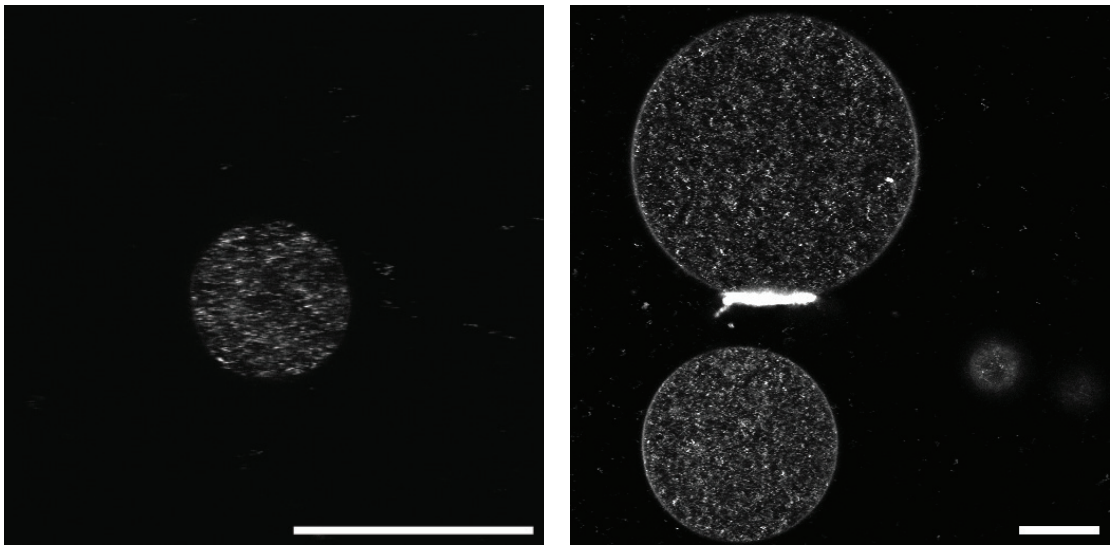

**Figure 4.8: Encapsulation of SUVs in GUVs.** Representative confocal microscopy images of naive SUVs (left, 1% Liss Rhod PE) and ACE2-functionalised SUVs (right, 1% Liss Rhod PE) encapsulated in GUVs. All scale bars are 20 $\mu$m. Adapted with permission from *ACS Nano* 2023, 17, 23913-23923. Copyright 2024 American Chemical Society.

To determine which of the two variants had a higher affinity, I coencapsulated Alpha and Omicron MiniVs together in GUVs. In this case, each MiniV population had a different fluorescently tagged lipid. As expected from earlier QCM-D results, Alpha MiniVs stayed primarily in the lumen of the GUV, while Omicron MiniVs accumulated at the membrane (Figure 4.9).[158]

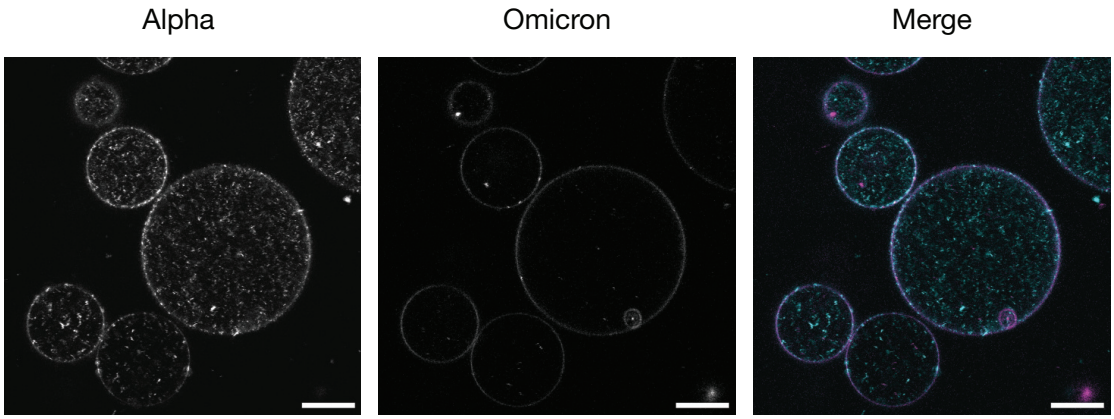


**Figure 4.9: Co-encapsulation of Alpha and Omicron MiniVs in GUVs.** Representative confocal microscopy images of Alpha (1% ATTO647 DOPE) and Omicron (1% ATTO488 DOPE) MiniVs co-encapsulated in GUVs. All scale bars are 20 $\mu$m. Adapted with permission from *ACS Nano* 2023, 17, 23913-23923. Copyright 2024 American Chemical Society.

Next, I studied the interaction of the MiniVs with the GUV outside membrane by adding them to the GUV outside buffer. As expected, neither SUVs nor Alpha MiniVs could interact with the membrane, unlike Omicron MiniVs (Figure 4.10). However, the latter appeared to aggregate when added to the external GUV solution, as indicated by the formation of large fluorescent clusters. I hypothesised that this could be explained by charge-mediated self-interactions between Omicron S of one MiniV and the membrane of another MiniV, as the surface of Omicron is positive and the MiniV vesicle is negatively charged (Figures 4.2 and 4.1). This was confirmed by incubating Omicron MiniVs with the ACE2 receptor, which prevented the self interaction and consequent aggregation by the high affinity of S to the receptor (Figure 4.11). To prevent aggregation within the MiniVs, 4 mol% DOPC was substituted by PEG(2000)-functionalised lipids. PEG molecules have been extensively used to avoid unspecific interactions.[164,165] This change in composition did not lead to significant changes in either size or zeta potential of either SUVs or MiniVs (Figure 4.12), with the exception of a small increase in zeta potential of PEG-functionalised Omicron MiniVs (Figure 4.12B).[158]

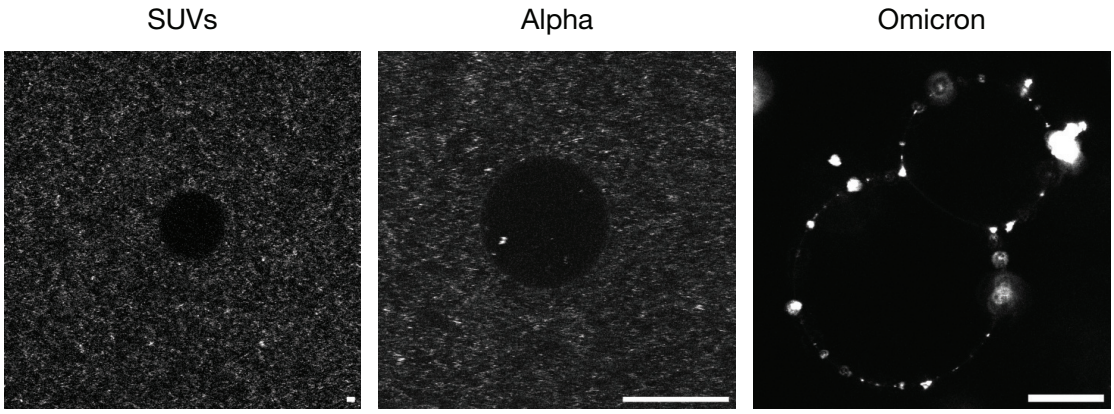


**Figure 4.10: MiniVs incubated with GUVs.** Representative confocal microscopy images of SUVs, Alpha or Omicron MiniVs (1% Liss Rhod PE) added to the outside solution of GUVs. All scale bars are 20 $\mu$m. Adapted with permission from *ACS Nano* 2023, 17, 23913-23923. Copyright 2024 American Chemical Society.

These newly PEG-functionalised MiniVs were incubated with the GUVs and their interaction with the membrane was studied. Following the results from the previous experiment, Alpha MiniVs did not interact with the GUV. In contrast, Omicron MiniVs formed a ring along the GUV outer membrane, the intensity of which increased over time (Figure 4.13).[158] These results confirmed the newly found lipid affinity of Omicron S-decorated MiniVs.

Thus, I have shown that the interaction stems from the positive and negative surfaces of Omicron S and the membrane, respectively. To further confirm this result, I produced

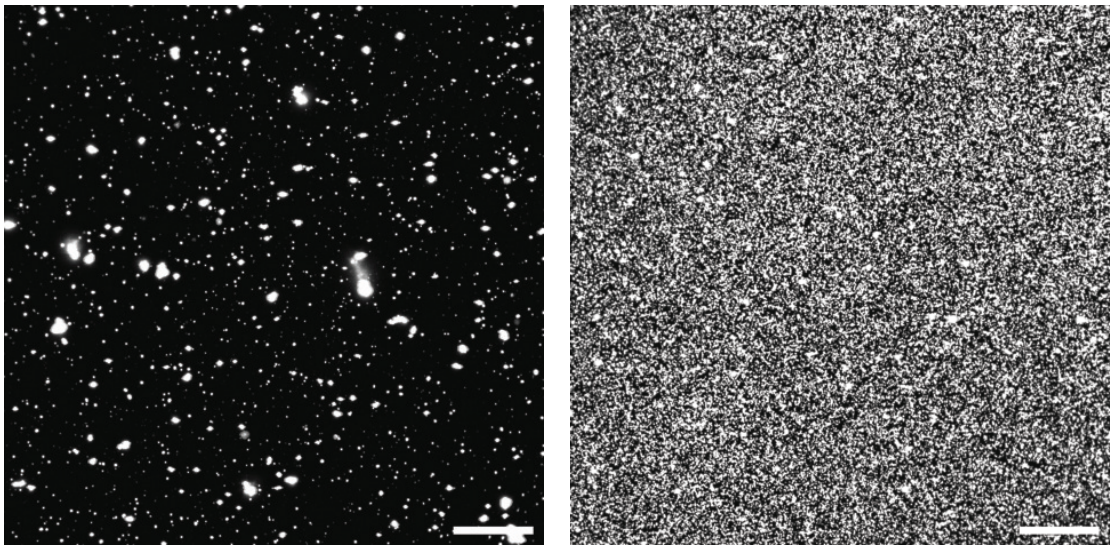

**Figure 4.11: Aggregation of Omicron MiniVs.** Representative confocal microscopy images of Omicron MiniVs alone (left) and incubated with ACE2 receptor (right) (1% Liss Rhod PE). Aggregation of Omicron MiniVs can be seen on the left in the shape of fluorescent clusters. All scale bars are 20 $\mu$m. Adapted with permission from *ACS Nano* 2023, 17, 23913-23923. Copyright 2024 American Chemical Society.

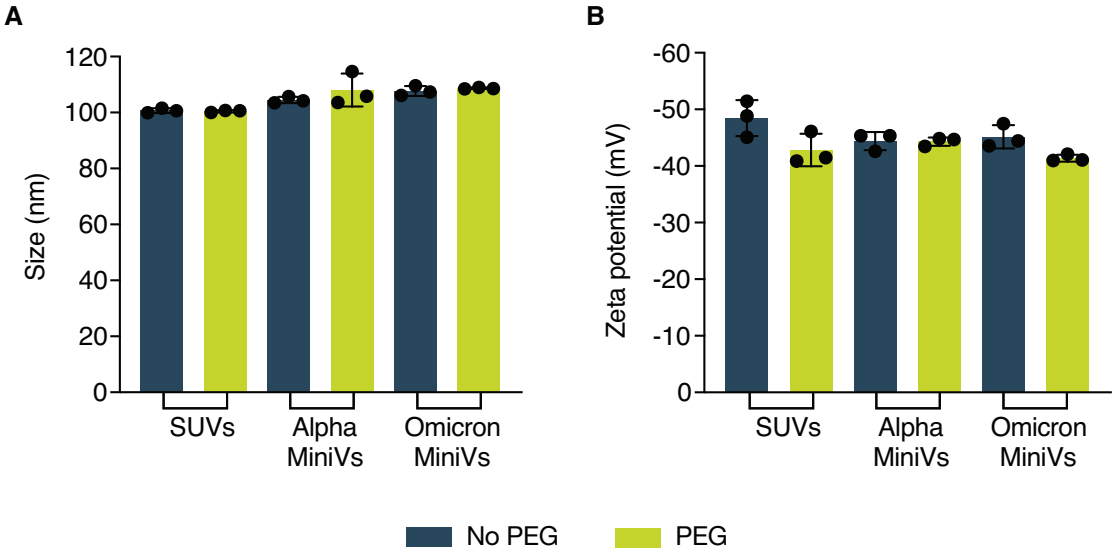


**Figure 4.12: Comparison of MiniVs and PEG-functionalised MiniVs.** Comparison of size (A) and zeta potential (B) of SUVs and MiniVs with and without PEG functionalisation. Size and zeta potential measurements were obtained by nanoparticle tracking analysis and dynamic light scattering in MilliQ water, respectively. Results correspond the mean ± SD from n = 3 technical replicates in each experimental condition. Adapted with permission from *ACS Nano* 2023, 17, 23913-23923. Copyright 2024 American Chemical Society.

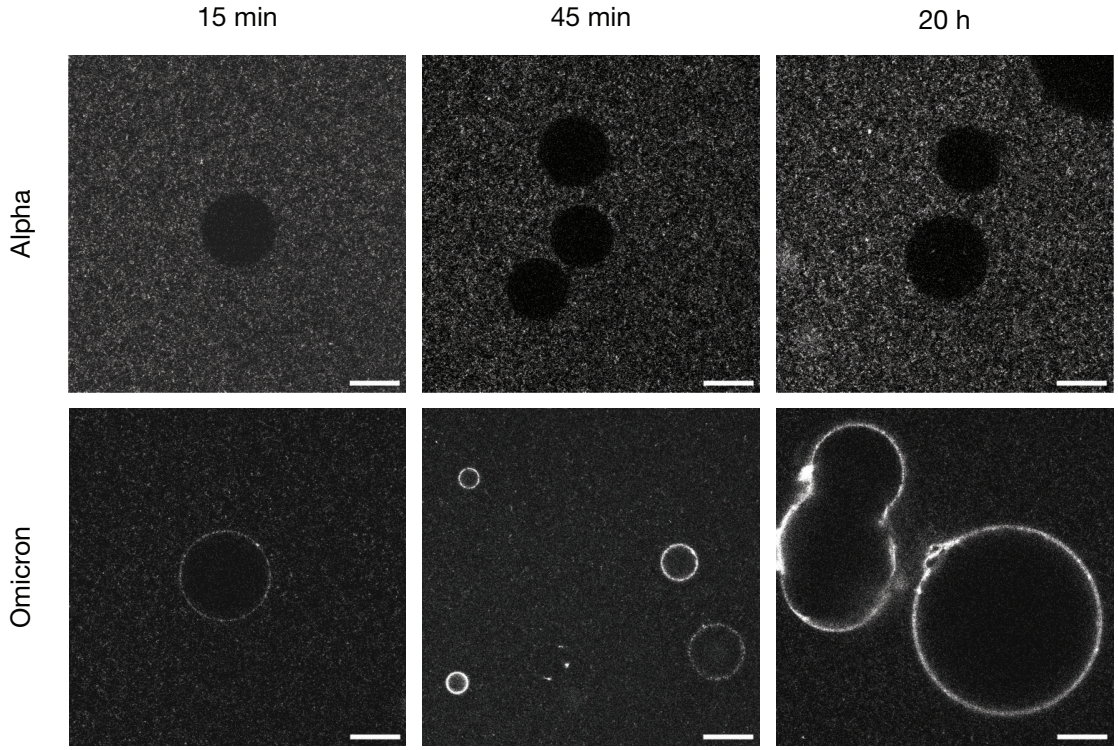


**Figure 4.13: PEG-MiniVs incubated with GUVs.** Representative confocal microscopy images of PEG-functionalised Alpha or Omicron MiniVs (1% Liss Rhod PE) added to the outside solution of GUVs. All scale bars are 20 $\mu$m. Adapted with permission from *ACS Nano* 2023, 17, 23913-23923. Copyright 2024 American Chemical Society.

positively charged GUVs where both Alpha and Omicron MiniVs were co-encapsulated. As seen in Figure 4.14, Alpha MiniVs, which present a more negative surface, are able to establish an interaction with the positive membrane of the GUV. On the other hand, Omicron MiniVs stayed predominantly in the lumen of the vesicle.

GUVs have also been used to study other aspects of the viral cycle, such as budding and fusion. Researchers designed and constructed an artificial viral capsid which could bud outside-to-inside or inside-to outside the GUV to form an enveloped viral capsid.[91] Viral fusion, on the other hand, was obtained by the interaction between GUVs and budded viruses of Baculovirus.[166] Moreover, GUVs with an ER-like composition have also been used as lipid compartments to mimic viral replication.[167] Altogether, these examples demonstrate the versatility of GUVs as simple and easy-to-produce mimics of the cellular plasma membrane or organelles.

In this section, I have used GUVs with the same lipid composition as the previously used SLB to corroborate the results obtained in the QCM-D. Encapsulation of Omicron and Alpha MiniVs inside GUVs demonstrated the high affinity of Omicron MiniVs towards

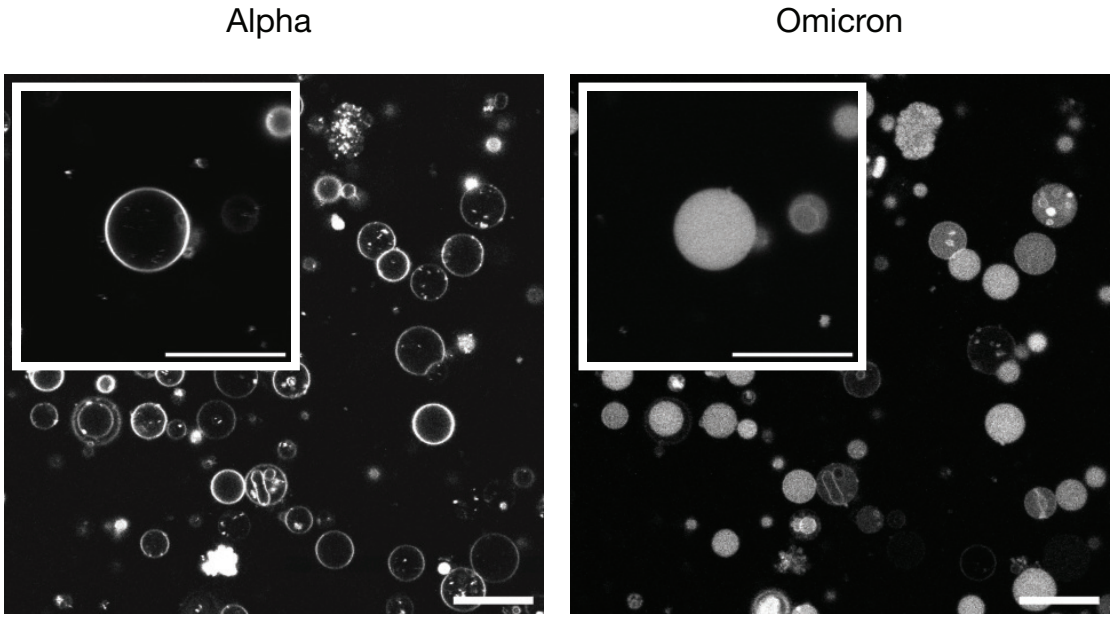


**Figure 4.14: Co-encapsulation of Alpha and Omicron MiniVs in positively charged GUVs.** Representative confocal microscopy images of Alpha (1% ATTO647 DOPE) and Omicron (1% ATTO488 DOPE) MiniVs co-encapsulated in positively charged GUVs. All scale bars are 20 $\mu$m. Adapted with permission from *ACS Nano* 2023, 17, 23913-23923. Copyright 2024 American Chemical Society.

the membrane in a well controlled system. I observed a similar result when I incubated Alpha and Omicron MiniVs with GUVs, in which only the latter could establish an interaction with the outer GUV membrane that increased over time. This affinity can be regulated by producing GUVs with a positive membrane charge. Altogether, I have confirmed the affinity of Omicron S and Omicron MiniVs towards negatively charged membranes, which shows the potential of using GUVs as synthetic minimal mimics of the cellular membrane.

## 4.4 Omicron MiniVs affinity to cells with and without ACE2 receptor

In the next step, I set out to investigate wether the results of the GUV experiments could be translated to interaction with cells. For that purpose, I chose two cell lines one with high and one with low expression of ACE2 receptor: Vero E6 and A549, respectively.[168] The expression of ACE2 was confirmed by flow cytometry using a fluorescently labelled anti-ACE2 antibody. As expected, Vero E6 showed a high ACE2 expression while it was absent in A549 cells (Figure 4.15).[158] Next, I designed a flow cytometry experiment in which cells were incubated with SUVs, Omicron or Alpha MiniVs. The vesicles

were fluorescently labelled, and this fluorescence was detected when the particles were attached to the plasma membrane or taken up by the cells.

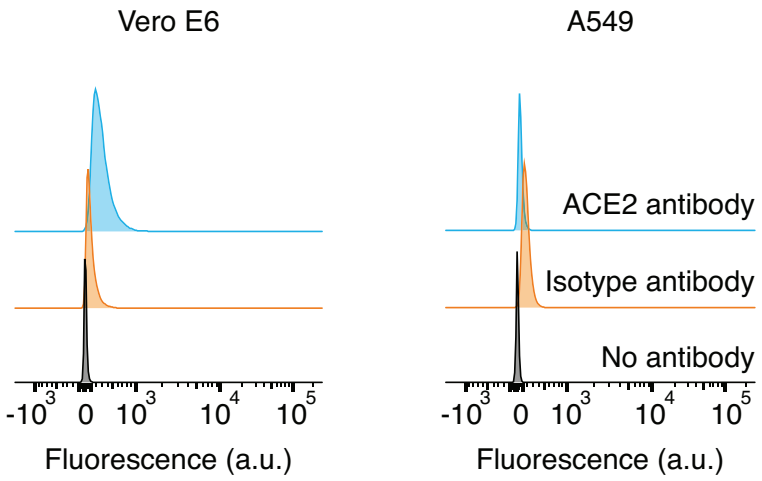


**Figure 4.15: ACE2 expression in Vero E6 and A549 cell lines.** Flow cytometry analysis of ACE2 receptor expression levels in Vero E6 and A549 cell lines. Adapted with permission from *ACS Nano* 2023, 17, 23913-23923. Copyright 2024 American Chemical Society.

I first focused on Vero E6 cells and incubated them with SUVs, Omicron and Alpha MiniVs for 1 h at RT. Despite the cells presenting high levels of ACE2 receptor, I observed a similar level of interaction of Omicron and Alpha MiniVs compared to SUVs (Figure 4.16). I would have expected a higher level of attachment and uptake of MiniVs due to their affinity to ACE2 through functionalisation with S. Studies have shown that functionalisation of liposomes promotes uptake by target cells.[169–171] Moreover, it has been reported that incubation of SUVs with MCF7 epithelial cells does not lead to internalisation of the vesicles.[118] However, this might depend on the cell line used, as researchers found that unfunctionalised liposomes were greatly uptaken by A549 cells after 2 h incubation with the vesicles.[172]

Due to this apparent uptake of SUVs and both types of MiniVs by ACE2-presenting Vero E6 cells, I decided to solely focus on vesicle attachment by halting the cellular uptake process. For that purpose, after detaching and counting the cells I kept them on ice to block endocytosis.[173,174] Unexpectedly, SUVs, Omicron and Alpha MiniVs showed the same level of interaction to Vero E6 cells (Figure 4.17). Due to their high ACE2 receptor presentation, both MiniVs were expected to have displayed an advantage in binding, compared to unfunctionalised SUVs. Since the results were similar to those obtained when the experiment was conducted at RT, I concluded that maintaining the cells at low temperatures did not fully halt the endocytosis process.

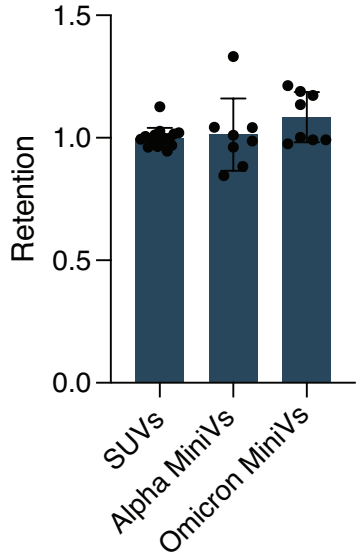


**Figure 4.16: Attachment of SUVs and MiniVs to Vero E6 cells at RT.** Quantification of SUVs, Alpha and Omicron MiniVs attachment to Vero E6 cells at RT by flow cytometry. Retention is calculated by normalising the fluorescence values relative to SUVs. Results correspond to the mean ± SD from, at least, n = 3 biological replicates.

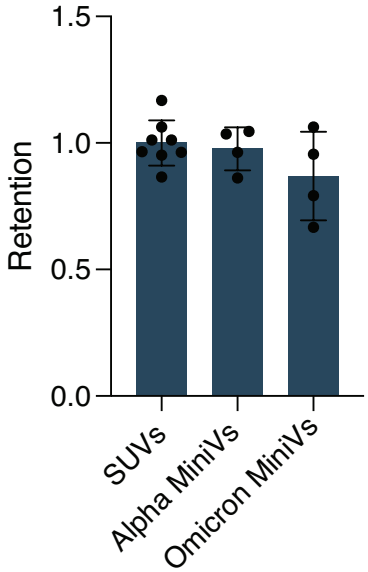


**Figure 4.17: Attachment of SUVs and MiniVs to Vero E6 cells on ice.** Quantification of SUVs, Alpha and Omicron MiniVs attachment to Vero E6 cells on ice by flow cytometry. Retention is calculated by normalising the fluorescence values relative to SUVs. Results correspond to the mean ± SD from, at least, n = 4 technical replicates.

The next experiments were done in collaboration with Duc Thien Bui, who did an internship under my supervision. Due to the fact that endocytosis did not seem to be blocked, I decided to fix the cells prior to the incubation with the vesicles to focus

exclusively on attachment.

SUVs, Alpha and Omicron MiniVs were incubated with Vero E6 and A549 cells at RT, after fixation of the cells. Both types of MiniVs showed a significantly higher retention than SUVs on the cellular membrane of Vero E6 (Figure 4.18A). This was due to the affinity of Alpha and Omicron S to the ACE2 receptor. When looking at the results with A549 cells, I observed that Omicron MiniVs showed a significantly stronger interaction than both Alpha MiniVs and SUVs (Figure 4.18B).[158] These results are consistent with the ones previously discussed, confirming the hypothesis that Omicron S has a newly discovered affinity for negatively charged lipid membranes. Furthermore, blocking the ACE2 receptor with an anti-ACE2 antibody did not prevent Omicron MiniVs from interacting with Vero E6 cells but it did for Alpha MiniVs (Figure 4.18C), mimicking the results observed in the ACE2-low A549 cell line.

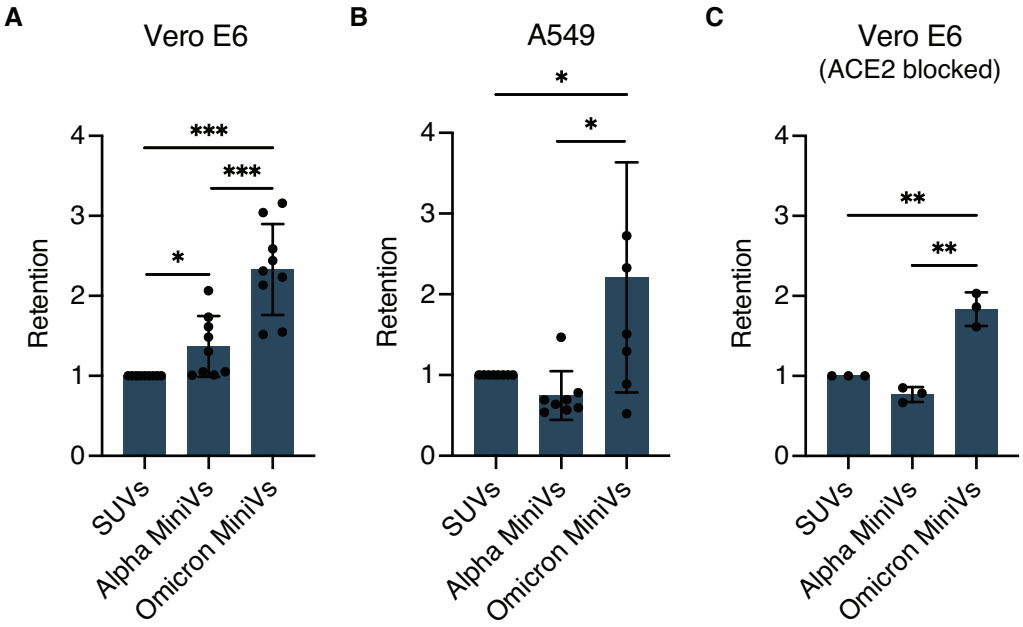


**Figure 4.18: Attachment of SUVs and MiniVs to fixed Vero E6 and A549 cells.** Quantification of SUVs, Alpha and Omicron MiniVs attachment to Vero E6 (A and C) and A549 (B) cell lines by flow cytometry. Retention is calculated by normalising the fluorescence values relative to SUVs. $*p < 0.05$, $**p < 0.005$, $* \ * \ * \ p < 0.001$ analysed using an unpaired two-tailed t-test. Results correspond to the mean ± SD from, at least, n = 3 biological replicates. Adapted with permission from *ACS Nano* 2023, 17, 23913-23923. Copyright 2024 American Chemical Society.

To obtain some qualitative data, I seeded both cell lines in separate glass-bottom wells and left them overnight to form a monolayer. Then, I fixed and stained them and finally added the SUVs, Alpha or Omicron MiniVs for incubation for 1 h. Similarly to the

results obtained with flow cytometry, both Omicron and Alpha MiniVs showed a higher interaction with the cell membrane than SUVs in Vero E6 cells (Figure 4.19). The same

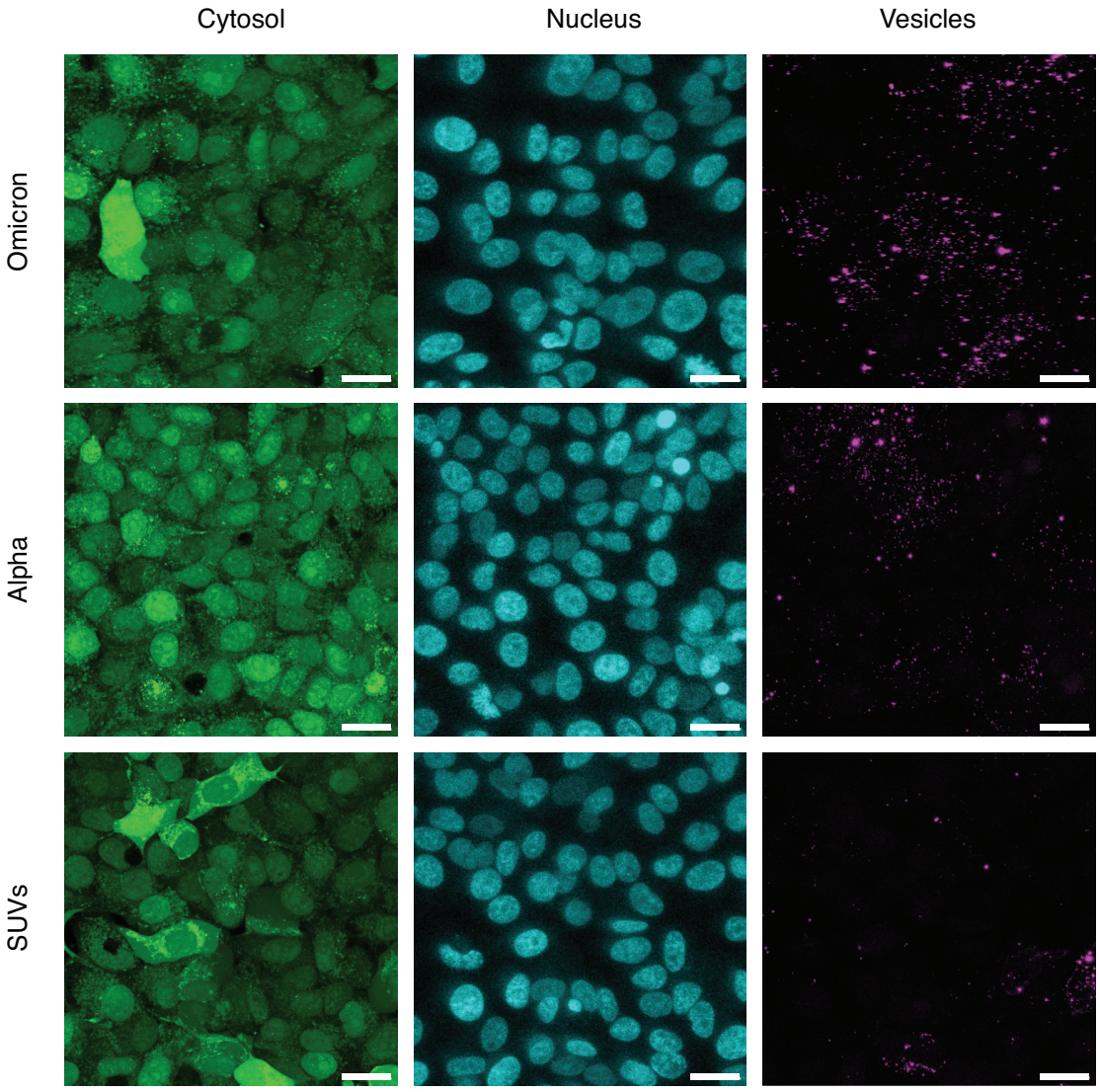


**Figure 4.19: Confocal microscopy of SUVs and MiniVs on Vero E6 cells.** Representative confocal microscopy images of SUVs, Alpha and Omicron MiniVs (magenta, 1% Liss Rhod PE) incubated for 1 h on fixed Vero E6 cells. Cells were stained with CellTracker Green CMFDA (cytosol, green) and Hoechst (nucleus, cyan). All scale bars are 20 $\mu$m. Adapted with permission from *ACS Nano* 2023, 17, 23913-23923. Copyright 2024 American Chemical Society.

experiment with A549 cells also mimicked the previously discussed results. Omicron MiniVs could bind to the cell membrane in the absence of ACE2, while the opposite was true for Alpha MiniVs (Figure 4.20).[158] The amount of Omicron MiniV particles found on A549 cells was much lower than on Vero E6 cells. This is in agreement with the here calculated $K_D$ of Omicron S to lipid membranes and the $K_D$ of the protein to

ACE2, which is at least three times lower.[31]

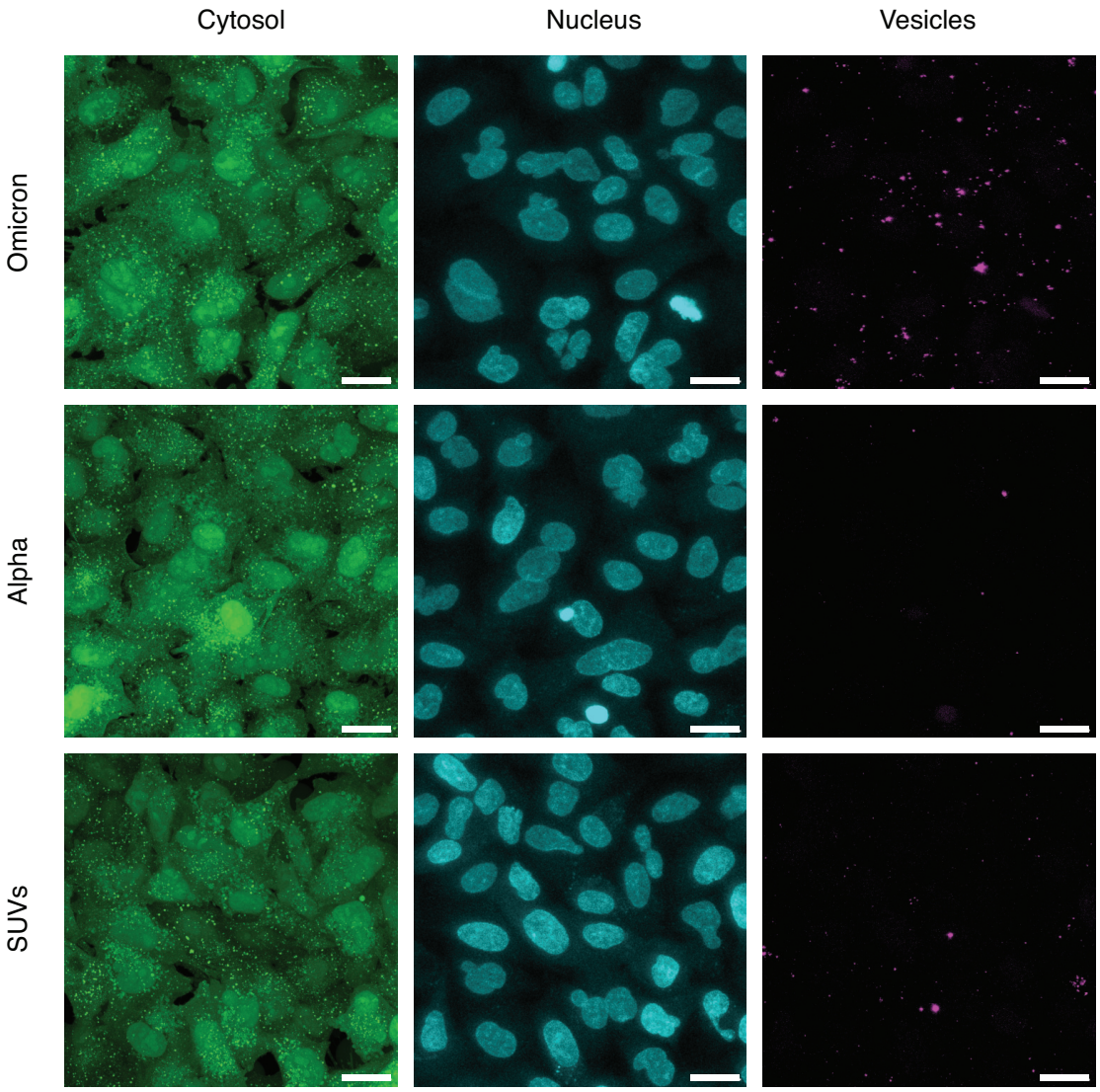


**Figure 4.20: Confocal microscopy of SUVs and MiniVs on A549 cells.** Representative confocal microscopy images of SUVs, Alpha and Omicron MiniVs (magenta, 1% Liss Rhod PE) incubated for 1 h on fixed A549 cells. Cells were stained with CellTracker Green CMFDA (cytosol, green) and Hoechst (nucleus, cyan). All scale bars are 20 $\mu$m. Adapted with permission from *ACS Nano* 2023, 17, 23913-23923. Copyright 2024 American Chemical Society.

Altogether, these results indicate a newly discovered affinity of Omicron S to lipid membranes, synthetic and cellular. Due to the fact that both types of membranes were negatively charged and that the surface of Omicron S is positively charged (in comparison to Alpha S), it can be postulated that the origin of this affinity is electrostatic. This novel interaction could, in part, explain the higher transmissibility found for Omicron SARS-CoV-2 variants.[44] The independence to ACE2 in binding to the plasma membrane

provides the virus with a broader cell tropism. Another argument that supports this hypothesis is the fact that SARS-CoV-2 Omicron appears to enter the cells mainly through the ubiquitous endocytic pathway making use of cathepsins. Other variants, however, rely on TMPRSS2 at the cell surface for fusion, which limits their infection to only those cells that express the protease.[48]

## 4.5 Identification of plasma membrane components relevant for Omicron S affinity

Once determined that the affinity stemmed from electrostatic interactions, the next step was to study which elements of the plasma membrane could be responsible for this interaction. With that aim, I developed a flow cytometry experiment based on the detection of the vesicles interacting with the cellular membrane, similarly to what I described previously (Section 4.4). In a first step, cells were treated with the plasma membrane-modifying compounds, then counted and incubated with SUVs, Alpha or Omicron MiniVs for 1 h. After incubation, cells were analysed using flow cytometry and the fluorescent signal from the vesicles attached to the cell membrane was recorded.

First, I identified three components that could be possible candidates in mediating Omicron S affinity to the plasma membrane: heparan sulfate, sphingomyelin (SM) and cholesterol. All of them had been reported in literature to affect the viral cycle of SARS-CoV-2, specifically the entry process.[22,65,175] Heparan sulfate had been reported to bind the RBD of Wuhan S.[22] Degradation of sphingomyelin to ceramide and cholesterol depletion with M$\beta$CD independently reduced infection of SARS-CoV-2 pseudoviruses.[65,175] However, all of these had been tested for Wuhan S, and could have a different effect on the binding of Omicron S.

I used again both the ACE2-rich and -poor cell lines, Vero E6 and A549, respectively. Cells were either left untreated or incubated with heparinase I, cholesterol or SM. Heparinases are enzymes that cleave heparin and heparan sulfate.[176] The treatment of Vero E6 cells with the enzyme had little effect on the binding of SUVs or Alpha MiniVs, and slightly increased the binding of Omicron MiniVs. Treating the cells with cholesterol led to higher interaction of only SUVs and Omicron MiniVs. The addition of SM reduced the binding in all the conditions (Figure 4.21). However, in A549 cells, the addition of SM affected only the binding of SUVs, leading to an increase, contrary to what was observed in Vero E6 cells. Treatment with heparinase did not change the interaction of either SUVs or MiniVs. The addition of cholesterol showed a similar

trend as in Vero E6, increasing the binding only of SUVs and Omicron MiniVs (Figure 4.21).

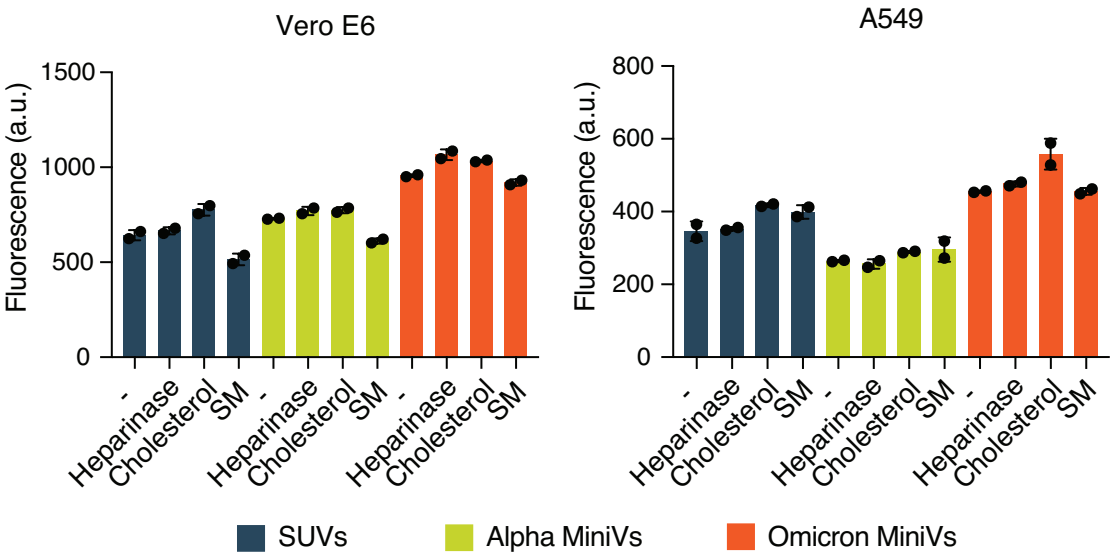


**Figure 4.21: Attachment of SUVs and MiniVs to treated Vero E6 and A549 cells.** Quantification of SUVs, Alpha and Omicron MiniVs attachment to Vero E6 (left) and A549 (right) cell lines by flow cytometry. Cells had been left untreated (-) or treated with heparinase (2850 mU/ml), cholesterol (100 $\mu$M) or SM (100 $\mu$M). Results correspond to the mean ± SD from n = 2 technical replicates in each experimental condition.

I noticed that the SUVs were binding almost as much as both Omicron and Alpha MiniVs (Figure 4.21). This meant that small affinity changes that could be induced by S, could not be confirmed as similar changes could be observed for the SUVs. Since the SUVs lack surface proteins, the interaction with the plasma membrane must have originated from their lipid composition. The original composition of the MiniVs, as explained earlier, is similar to that found in the ERGIC. However, the used S is his-tagged meaning that the protein is not incorporated into the membrane. Consequently, there is no influence of the lipid composition on S, as they are not in contact. That is why, for the sake of these experiments, I decided to change the composition of the vesicles that form the MiniVs to one that does interact as little as possible with the plasma membrane.

I compared control vesicles (see Table 3.1), i.e. those with the ERGIC composition, with three very simple compositions: 100% DOPC (neutral lipid), 80:20 DOPC:DOPG (negatively charged lipid) and 80:20 DOPC:DOTAP (positively charged lipid). First, I measured their zeta potential in water. As expected, DOPC vesicles had an almost neutral charge, while both control vesicles and those containing 20% DOPG had a negative charge (Figure 4.22A). Vesicles containing 20% DOTAP presented a positive

charge (Figure 4.22A). When comparing interaction with A549 cells, DOPC vesicles interacted the least, closely followed by DOPG-containing vesicles. The control vesicles, those with a similar lipid composition as the viral envelope, showed the highest affinity to the cell membrane (Figure 4.22B). This might explain, in part, the complex lipid composition of viral envelopes.

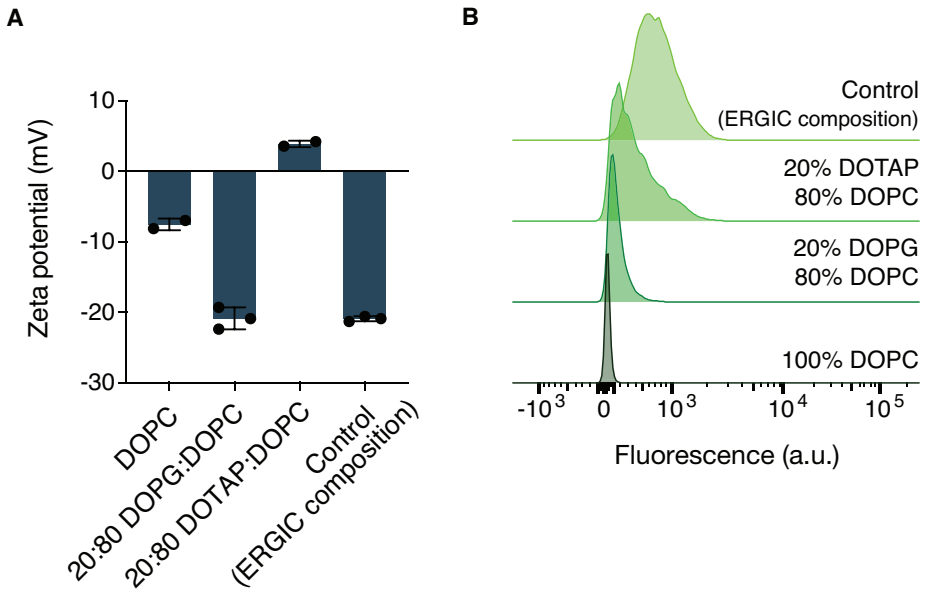


**Figure 4.22: Comparison of SUVs of different composition and charge.** A) Zeta potential of four populations of SUVs with different lipid composition by dynamic light scattering in MilliQ water. B) Flow cytometry histogram of the attachment of the SUV populations to A549 cells. Results on the left correspond to the mean ± SD from n = 3 technical replicates.

For these reasons, in the next experiments I used vesicles composed exclusively of DOPC (substituting 1% when needed for DGS NTA($Ni^{2+}$) and fluorescently tagged lipids). When comparing the binding of DOPC and control vesicles (those mimicking the ERGIC composition), it can be observed that the attachment of DOPC vesicles is almost residual in both cell lines, while the distinctive higher affinity induced by the presence of S is maintained (Figure 4.23).

Given the low affinity of DOPC SUVs for cells, I decided to repeat the experiment previously described, using these vesicles as the scaffold for MiniVs. The previous treatments of the cells had little effect on the binding of MiniVs (Figure 4.21). Therefore, I treated the cells with double the concentration of heparinase, cholesterol and SM compared to the previous experiment, and then incubated them with the vesicles.

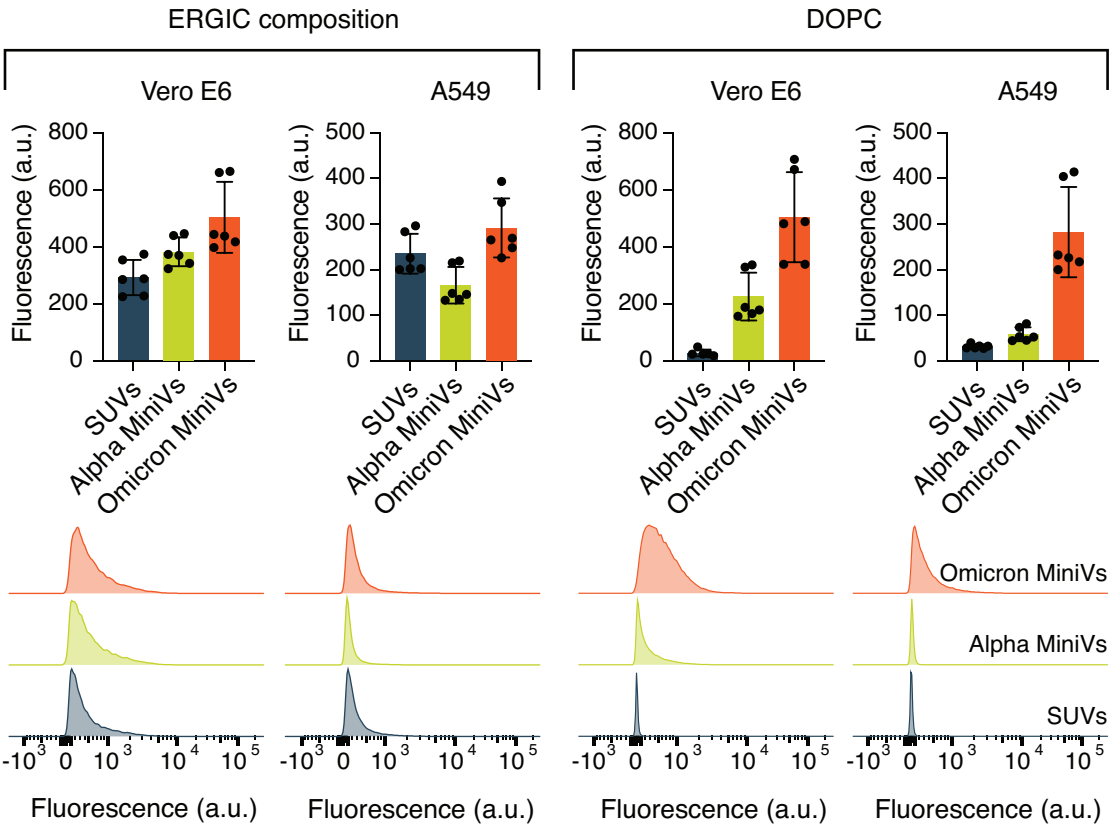


**Figure 4.23: Comparison of cell affinity of MiniVs with ERGIC or DOPC composition.** Comparison of affinity of SUVs and MiniVs with ERGIC (left) or DOPC (right) composition to Vero E6 and A549 cell lines. Quantification of the flow cytometry results (top) and representative graph of flow cytometry experiment (bottom). Results correspond to the mean ± SD from n = 3 biological replicates.

Observing the graphs in Figure 4.24, I could see a small increase in attachment of SUVs, Alpha and Omicron MiniVs when both Vero E6 and A549 cells had been treated with heparinase I, which contradicts previous published findings.[22,160] The inconsistency in results could be due to the chosen enzyme, as heparinase I exhibits greater activity on heparin, not heparan sulfate.[177] Thus, results found in literature could likely be mimicked by using a combination of other heparinases which preferentially cleave heparan sulfate. The addition of SM to Vero E6 cells caused no difference in the attachment of SUVs or MiniVs. This discrepancy in results to the ones obtained with ERGIC composition MiniVs (Figure 4.21), could be attributed by the influence of the lipid composition in the cellular attachment process. On the contrary, in A549 cells, SUVs and Alpha MiniVs showed a slight increase in attachment following treatment with SM (Figure 4.24), similarly to that previously observed (Figure 4.21). Given the fact that the effect of the SM treatment was similar on SUVs and Alpha MiniVs, it could not be assumed that the membrane changes were actually affecting S binding to the plasma membrane.

In both cell lines, the treatment that induced the biggest effect was the addition of cholesterol to the plasma membrane. The significant increase of attachment in A549 could be observed for SUVs, Alpha and Omicron MiniVs. This meant, that I could not attribute the change in attachment to S, but it could also be due to the lipid membrane of the vesicles interacting with the cell membrane. When Vero E6 cells were treated with cholesterol, SUVs showed a small significant increase. Nonetheless, the biggest effects were observed for Omicron and Alpha MiniVs. This effect was, in fact, opposite for each variant. While Omicron MiniVs showed a significantly higher attachment when the cell membrane was loaded with cholesterol, the interaction of Alpha MiniVs diminished (Figure 4.24). This experiment identified cholesterol as one key player in the attachment process of SARS-CoV-2.

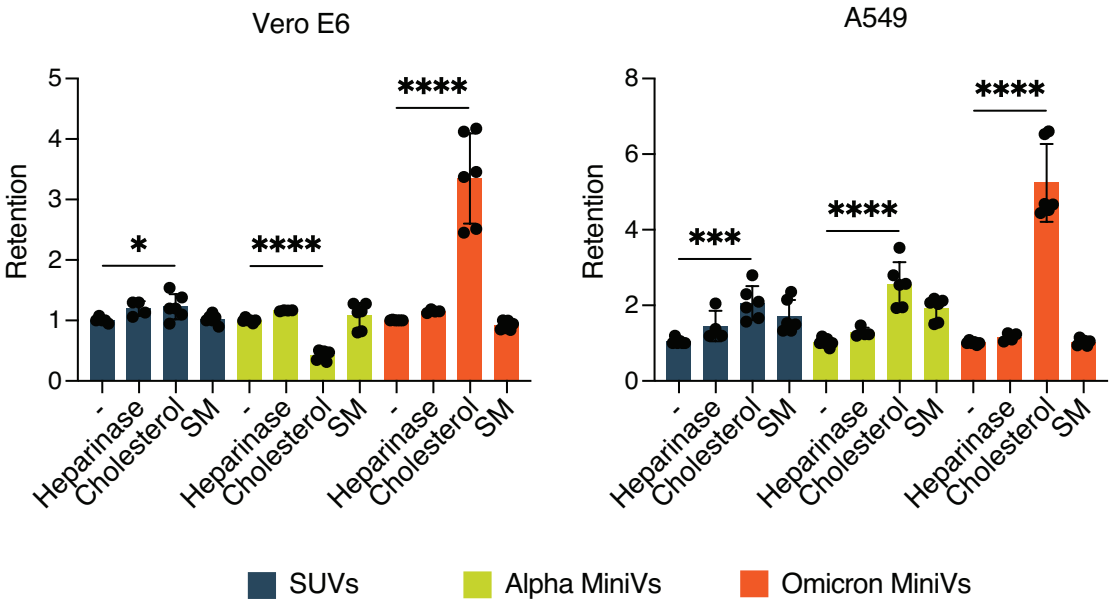


**Figure 4.24: Attachment of DOPC SUVs and MiniVs to treated Vero E6 and A549 cells.** Quantification of DOPC SUVs, Alpha and Omicron MiniVs attachment to Vero E6 (left) and A549 (right) cell lines by flow cytometry. Retention is calculated by normalising the fluorescence values relative to untreated cells for each vesicle population. Cells had been left untreated (-) or treated with heparinase (5714 mU/ml), cholesterol (200 $\mu$M) or SM (200 $\mu$M). Results correspond to the mean ± SD from n = 3 biological replicates. $*p < 0.05$, $***p < 0.001$, $****p < 0.0001$ analysed using an unpaired two-tailed t-test.

Cholesterol had already been identified as an important lipid in the infection process of many viruses, not only for SARS-CoV-2.[59,60] However, the majority of studies are focused on its effect on other parts of the viral cycle, such as fusion or general infectivity.[62,175] Using MiniVs and exclusively studying attachment allows for the discovery of new findings that are often challenging to obtain with more complex systems, such as

natural viruses or pseudoviruses. Although follow-up work will need to be performed with more complex systems, the discussed experiments provide a first glance on the importance of cholesterol in the viral attachment process.

### 4.5.1 The impact of cholesterol in the interaction of Omicron and Alpha S with cell membranes

Considering the impact of adding cholesterol to the plasma membrane on the cellular attachment of Alpha and Omicron MiniVs (Figure 4.24), the subsequent experiments were focused on this component of the cellular membrane. The goal was to investigate various methods to modify the cholesterol content of the plasma membrane and observe their effects on Alpha and Omicron MiniV attachment. As I had already tested the addition of cholesterol to the plasma membrane, I first focused on its removal using two methods: cholesterol extraction with M$\beta$CD or substitution with 25-hydroxycholesterol (25HC).[61,178] Cholesterol can be removed from the plasma membrane with M$\beta$CD, as it presents a hydrophobic cavity where cholesterol can be accommodated.[179] The mode of action of 25HC is different. This modified cholesterol is naturally found in cells and its level can increase during viral and bacterial infections. Due to the fact that 25HC is a homeostatic regulator of cholesterol, it can trigger the mechanisms to lower cholesterol levels in the cell.[180] It has already been used in the past as a cell membrane cholesterol-depleting drug with the aim of inhibiting SARS-CoV-2 membrane fusion.[181]

First, I wanted to ensure that the modification of cholesterol levels from the plasma membrane (both increase and reduction) was indeed taking place. For that purpose, I used the fluorescent probe laurdan. Laurdan is a fluorescent molecule with spectral sensitivity to the polarity of the environment. In the presence of polar solvents, its emission spectrum peak undergoes a 50 nm red shift. It can be utilised to distinguish membranes with different degrees of organisation. In a loosely packed membrane the penetration of water molecules will be higher when compared to an ordered membrane, which will lead to the red-shifting of the emitted fluorescence.[150,182] Due to its higher photostability, brightness and sensitivity to membrane polarity, confocal microscopy experiments were performed using C-laurdan, instead of laurdan.[183]

When imaging laurdan using confocal microscopy, emission is recorded between 415-455 nm and between 490-525 nm. The average intensities in these two channels are used to calculate a general polarisation value (GP) (see Equation 3.4) which ranges from +1 to -1. A high GP value indicates a highly ordered membrane, while a low GP value corresponds to a less ordered membrane. In general terms, a membrane containing high

amounts of cholesterol will present an increased phospholipid order and, consequently, a higher GP value than one lacking cholesterol.[184]

I treated the cells with cholesterol, M$\beta$CD or 25HC. Incorporation of cholesterol should increase the GP value as the membrane becomes more ordered. The treatment with M$\beta$CD should induce the opposite effect, as it depletes cell membrane cholesterol.[185] The only difference between 25HC and cholesterol is the hydroxyl group. Therefore, laurdan emission might not differ much from that obtained in the cholesterol-treated cells.

From the GP distributions in A549 cells we can infer that cholesterol is being added when the distribution shifts to positive values or removed (M$\beta$CD) when the distribution shifts to negative values compared to the untreated control (Figure 4.25). Insertion of 25HC also yields a shift to positive GP values which could be due to its similar structure to cholesterol. However, it has been reported that incorporating 25HC into the membrane counteracts the lipid-condensing effects of cholesterol, thereby reducing the membrane's stiffness.[186] This could explain the smaller shift of cells treated with 25HC in comparison to those treated with cholesterol. Treatment of Vero E6 cells with cholesterol also induced a positive shift in the GP values. However, the curve belonging to cells incubated with 25HC did not have a clear negative or positive peak. Moreover, treating the cells with M$\beta$CD did not cause any difference in the GP value compared to the untreated control. This contrasting results between both cell lines could stem from differences in their basal levels of cholesterol. Therefore, the cholesterol-depleting effect of M$\beta$CD on Vero E6 cells might not have been as big as on A549, hence the similarity of GP curves of M$\beta$CD-treated and untreated Vero E6 cells.

Despite the differences in results of cholesterol-depleting treatments in Vero E6 and A549 cells, I decided to investigate the differences in MiniV affinity in M$\beta$CD-treated cells. Both cell lines were treated with increasing amounts of the drug and incubated with SUVs and MiniVs. I observed a significant increase in attachment of SUVs, Alpha and Omicron MiniVs to A549 cells when comparing untreated and 10 mM M$\beta$CD-treated cells (Figure 4.26). Comparing the same treatment conditions in Vero E6, a smaller but significant increase could only be observed for SUVs and Alpha MiniVs. The results are in agreement with those observed in Figure 4.25, in which Vero E6 cells treated with 10 mM M$\beta$CD presented an almost identical GP curve to that of untreated cells. The GP values pointed out that the depletion of cholesterol of Vero E6 cells had been insufficient. The diminished cholesterol removal in comparison to A549 cells (Figure 4.25) could explain the mild effect of M$\beta$CD on the attachment of Alpha and Omicron MiniVs (Figure 4.26).

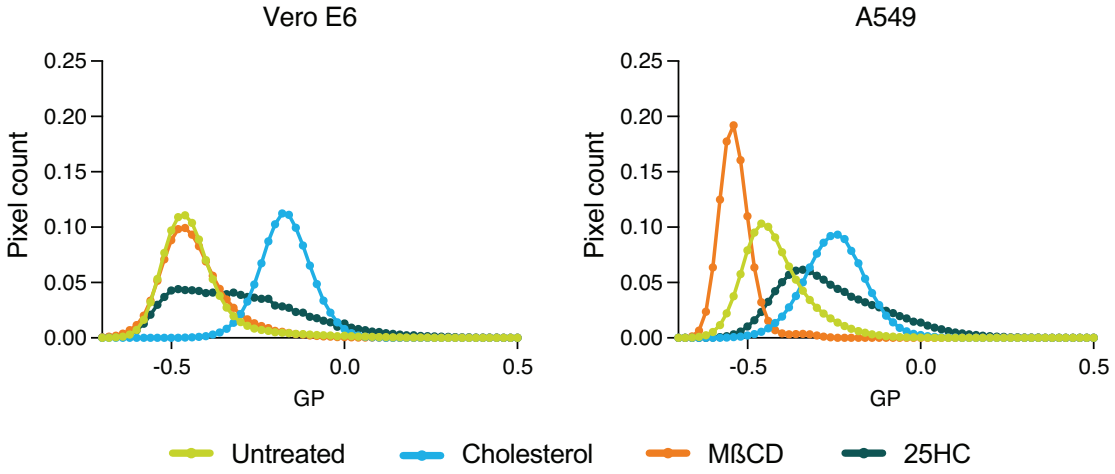


**Figure 4.25: Plasma membrane fluidity measured by C-laurdan.** Distribution of GP values of Vero E6 (left) and A549 (right) cells untreated or treated with 200 $\mu$M cholesterol, 10 mM M$\beta$CD or 200 $\mu$M 25HC.[187]

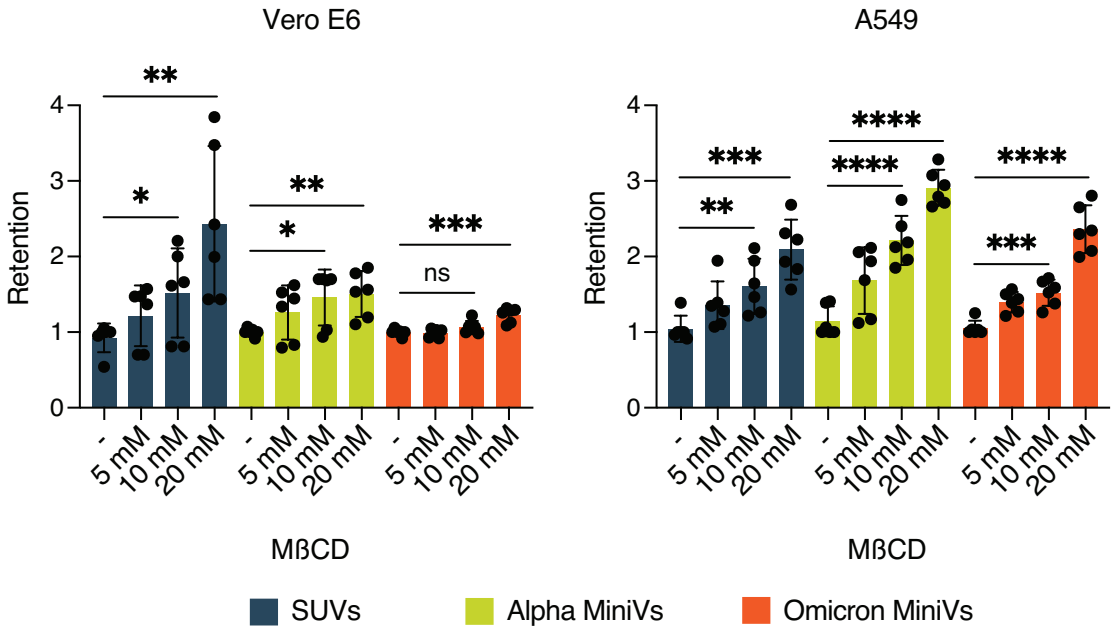


**Figure 4.26: Attachment of DOPC SUVs and MiniVs to M$\beta$CD-treated Vero E6 and A549 cells.** Quantification of DOPC SUVs, Alpha and Omicron MiniVs attachment to untreated (-) or M$\beta$CD-treated Vero E6 (left) and A549 (right) cell lines by flow cytometry. Retention is calculated by normalising the fluorescence values relative to untreated cells for each vesicle population. Results correspond to the mean ± SD from n = 3 biological replicates. $*p< 0.05$, $**p < 0.005$, $***p < 0.001$, $****p < 0.0001$, n.s. not significant, analysed using an unpaired two-tailed t-test.

The retention values for Omicron and Alpha MiniVs in A549 cells doubled and tripled, respectively, at the highest concentration of M$\beta$CD. Again, a significant increase could be observed in a smaller scale in Vero E6 cells, this time for SUVs and both types of

MiniVs. One possible explanation for this result is the high concentration of M$\beta$CD used (20 mM), which was double that of the laurdan experiment and may have induced greater cholesterol depletion.

A similar phenomenon could be seen when the cells were treated with 25HC (Figure 4.27). In A549 cells, there was a significant increase in retention of all vesicles when cells had been treated with 200 $\mu$M 25HC. In contrast, a significant increase was seen for SUVs and Omicron, but not Alpha, MiniVs in treated Vero E6 cells. Similarly to what was observed with M$\beta$CD, the incubation of Vero E6 cells with 25HC did not yield the same effect in terms of laurdan emission and GP values as it did for A549 (Figure 4.25). This might explain the differences in vesicle retention when comparing both 25HC-treated cell lines.

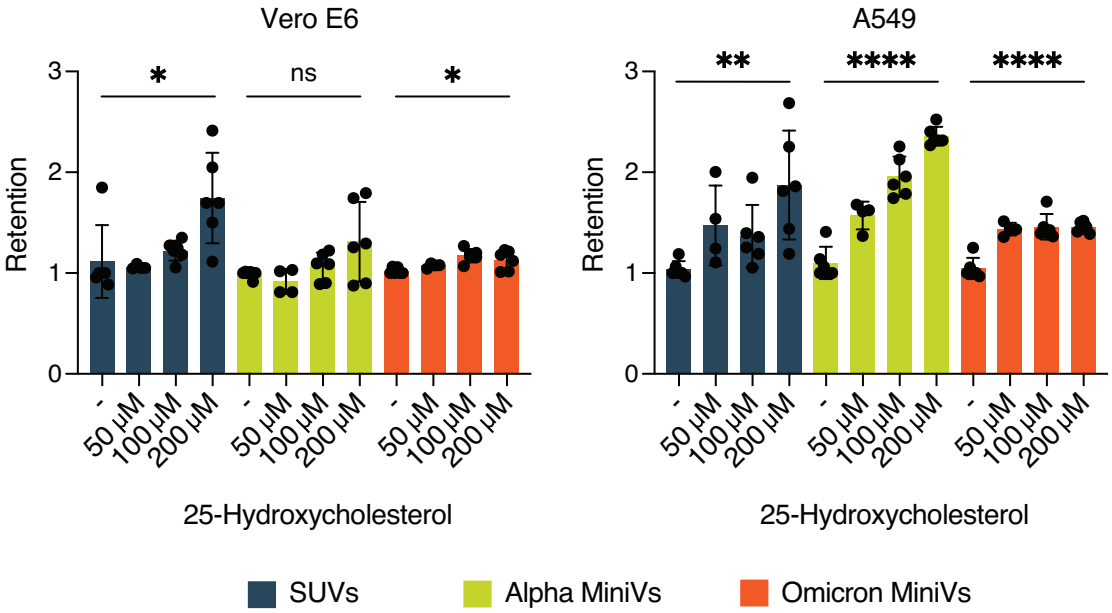


**Figure 4.27: Attachment of DOPC SUVs and MiniVs to 25HC-treated Vero E6 and A549 cells.** Quantification of DOPC SUVs, Alpha and Omicron MiniVs attachment to untreated (-) or 25HC-treated Vero E6 (left) and A549 (right) cell lines by flow cytometry. Retention is calculated by normalising the fluorescence values relative to untreated cells for each vesicle population. Results correspond to the median ± SD from n = 3 biological replicates. $*p< 0.05$, $**p < 0.005$, $****p < 0.0001$, n.s. not significant, analysed using an unpaired two-tailed t-test.

Both experiments share the observation that increases in MiniV attachment were, at least partially, also observed for SUVs. This indicates that the change cannot be solely attributed to Alpha or Omicron S being affected by cholesterol depletion. Instead, the results suggest that the increased interaction may be due to a change in the vesicle membrane's affinity when cholesterol is removed from the cell membrane. It is possible

that S could also be affected in the same way and that cholesterol removal affects the viral entry process.[61,175] However, this cannot be confirmed due to SUVs showing the same behaviour as MiniVs.

Despite having a similar problem as before, i.e. the interaction of the SUV membrane with the plasma membrane shields the affinity effect on S, there were not many alternatives to solve the issue. One would be to use PEGylated lipids, like I did for the GUV experiments to prevent Omicron MiniVs aggregation. PEG is a molecule used specifically to avoid unspecific interactions.[164,165] However, it has been reported that PEGylation of particles induce a higher uptake by cells, which also probably translates to a previous higher attachment, probably through opsonisation with proteins found in the cell media.[188] Another strategy would be to use a different type of nanoparticle (NP) (e.g. polymers, gold or silica NPs) for functionalisation with S, instead of lipid vesicles. Nevertheless, the physical properties of these NPs can be very different to that of liposomes (in terms of stiffness, for example) and their interaction with the cell membrane might still be relevant, as many types of NPs are used for drug delivery purposes.[189]

Since cholesterol removal strategies produced an effect on both SUV and MiniV attachment, I decided to focus exclusively on incorporating cholesterol into the plasma membrane. As observed in previous experiments (Figure 4.24), increasing cholesterol levels on the cellular membrane of Vero E6 induced opposite effects on the attachment of Omicron and Alpha MiniVs. The incorporation of cholesterol was quantified by flow cytometry making use of a fluorescently tagged cholesterol. As observed in Figure 4.28, both cell lines incorporated cholesterol into their membrane in a dose-dependent manner.

After measuring the cholesterol incorporation into the cell membrane of both cell lines, I proceeded to treat the cells and incubate them with SUVs and MiniVs. In a concentration-dependent manner, Alpha MiniVs significantly diminished their interaction with the cell membrane of Vero E6 cells. I observed the opposite effect for Omicron MiniVs, which tripled their retention value when cells had been treated with the highest concentration of cholesterol. SUVs only showed a significant increase in attachment when cells had been treated with 200 $\mu$M cholesterol. Contrarily, in A549 cells the increase was significant and consistent for SUVs, Alpha and Omicron MiniVs, but markedly higher for the latter (Figure 4.29).

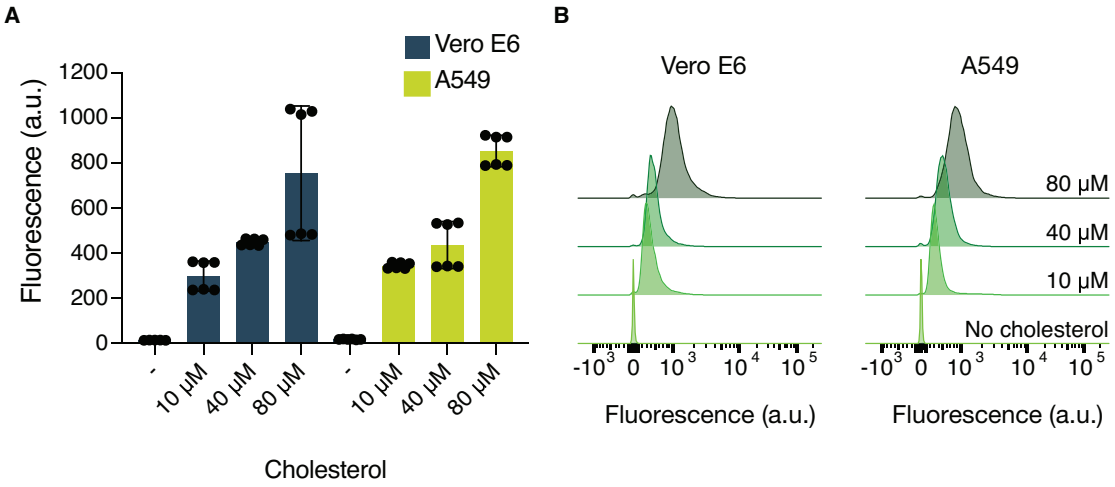


**Figure 4.28: Incorporation of cholesterol into the plasma membrane.** Measurement of cholesterol incorporation into the plasma membrane of Vero E6 and A549 cells by flow cytometry. Quantification of the flow cytometry results (A) and representative graph of flow cytometry experiment (B). Cholesterol is detected by adding 10% wt TopFluor cholesterol of the total cholesterol amount. Results on the left correspond to the median ± SD from n = 2 biological replicates.

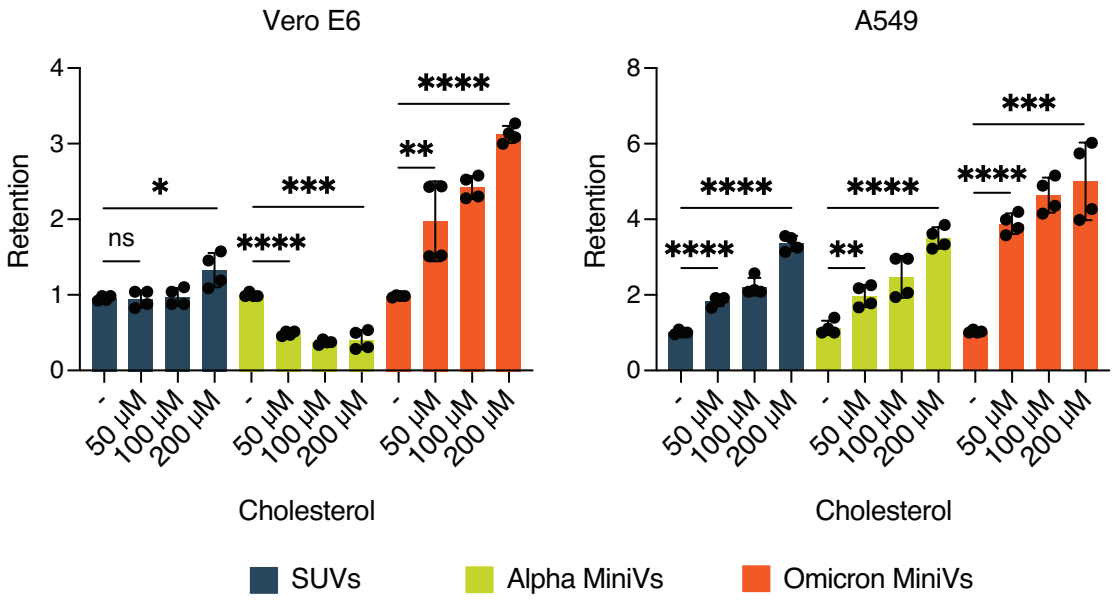


**Figure 4.29: Attachment of DOPC SUVs and MiniVs to cholesterol-treated Vero E6 and A549 cells.** Quantification of DOPC SUVs, Alpha and Omicron MiniVs attachment to untreated (-) and cholesterol-treated Vero E6 (left) and A549 (right) cell lines by flow cytometry. Retention is calculated by normalising the fluorescence values relative to untreated cells for each vesicle population. Results correspond to the mean ± SD from n = 2 biological replicates. $*p < 0.05$, $**p < 0.005$, $***p < 0.001$, $****p < 0.0001$, n.s. not significant, analysed using an unpaired two-tailed t-test.

At the end of these experiments, I noticed that the amount of recorded cells in the flow cytometer was reducing in a cholesterol concentration-dependent manner, specially for Vero E6. I used propidium iodide (PI), a fluorescent DNA-binding dye, to measure the percentage of cells alive after cholesterol treatment. PI can only penetrate the cell membrane of those cells that are dead or in the process of dying.[190] I found that there was a relevant drop in survival when cells were treated with 200 $\mu$M cholesterol (Figure 4.30). This was probably due to the cholesterol concentrations used, as high amounts of cholesterol can induce cell apoptosis.[191] For this reason, I repeated the experiments with

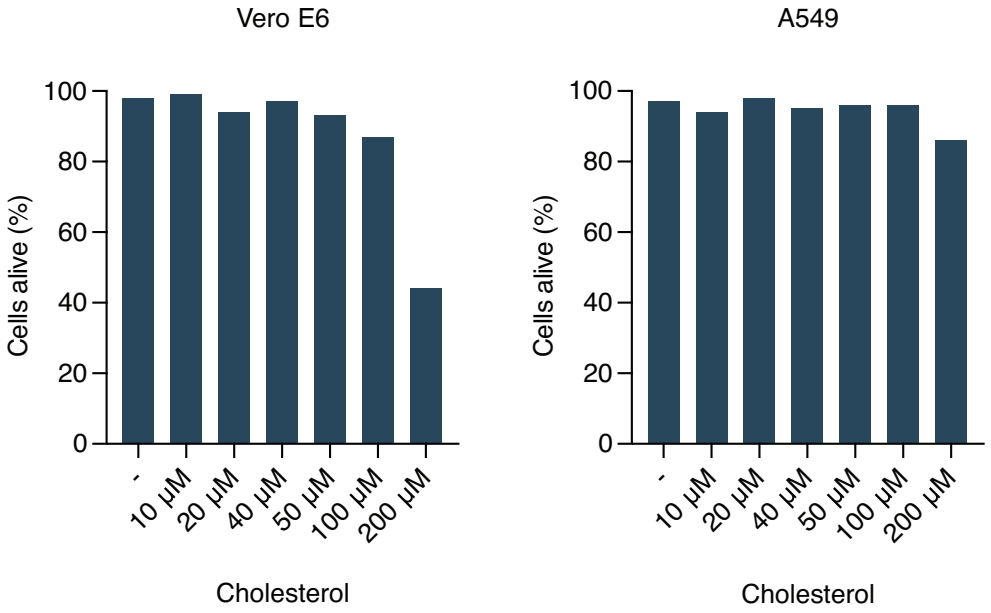


**Figure 4.30: Cell survival after high cholesterol treatment.** Quantification of Vero E6 (left) and A549 (right) cell survival rate after 1 h incubation with different cholesterol concentrations.

a lower range of cholesterol concentrations. The results followed the same trend as the previous ones: in Vero E6 cells, Omicron MiniVs showed a significant dose-dependent increase of attachment to the plasma membrane, while Alpha MiniVs presented a significant decrease in interaction (Figure 4.31). SUVs only showed a significant increase in retention when cells had been treated with the highest concentration of cholesterol. In A549, there was a significant increase in affinity of SUVs and both MiniVs as well.

To investigate the origin of the discrepancy in the interaction pattern of Alpha and Omicron MiniVs in Vero E6 cells, I first tested whether there could be an affinity between Omicron S and cholesterol. Such an affinity had already been hypothesised and reported for the S1 domain of the Wuhan variant.[192] With that aim, I conducted a QCM-

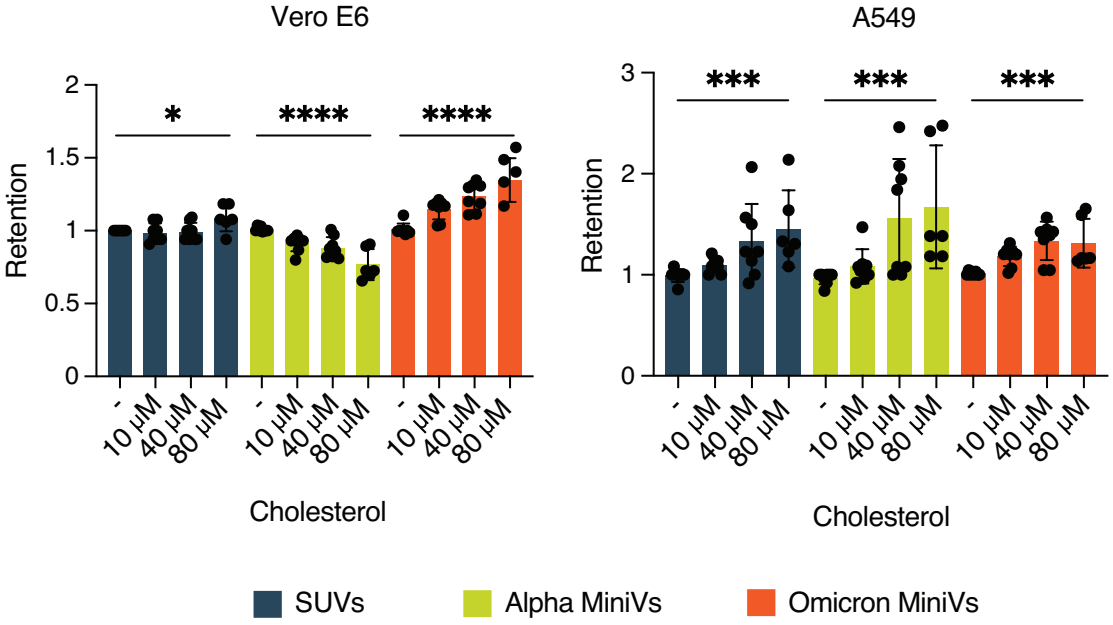


**Figure 4.31: Attachment of DOPC SUVs and MiniVs to low cholesterol-treated Vero E6 and A549 cells.** Quantification of DOPC SUVs, Alpha and Omicron MiniVs attachment to untreated (-) or low cholesterol-treated Vero E6 (left) and A549 (right) cell lines by flow cytometry. Retention is calculated by normalising the fluorescence values relative to untreated cells for each vesicle population. Results correspond to the mean ± SD from, at least, n = 3 biological replicates. $*p < 0.05$, $***p < 0.001$, $****p < 0.0001$ analysed using an unpaired two-tailed t-test (left) or a Mann-Whitney test (right).

D experiment to study the interaction of Omicron MiniVs towards SLBs with increasing amounts of cholesterol (Figure 4.32). As seen in Figure 4.33, there was no correlation between Omicron S attachment to the membrane and the amount of cholesterol in the SLB.

Altogether, I have demonstrated the impact that cholesterol levels on the plasma membrane have on the attachment of Omicron and Alpha MiniVs. The increase and decrease in attachment of Omicron and Alpha MiniVs, respectively, when the cells presented elevated cholesterol levels was observed in Vero E6, but not in A549 cells. Taking into account the difference in ACE2 expression of the two cell lines, one possible explanation for the opposite behaviour of the variants would be a change in receptor organisation. Cholesterol regulates the protein organisation on the cell membrane and can induce clustering of the receptor in lipid nanodomains.[61,193] An increased amount of ACE2 receptors binding to S on the MiniV surface might elevate avidity between the cell and the synthetic virus and, thus, lead to a higher attachment. This would explain the higher interaction of Omicron MiniVs, however it does not clarify the decrease of Alpha MiniVs. Therefore, the effect cannot be due to ACE2 receptor reorganisation.

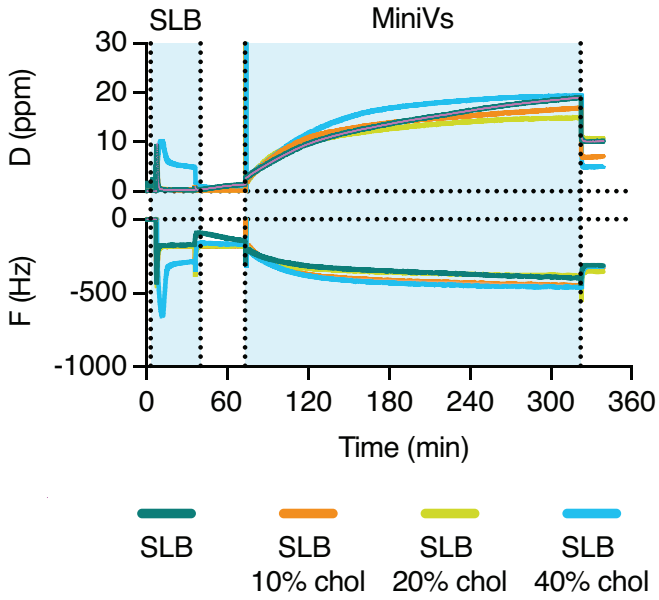


**Figure 4.32: Affinity of Omicron MiniVs to SLBs containing cholesterol.** Representative QCM-D experiment of Omicron MiniVs in contact with SLBs containing increasing amounts of cholesterol. D is dissipation and F is frequency.

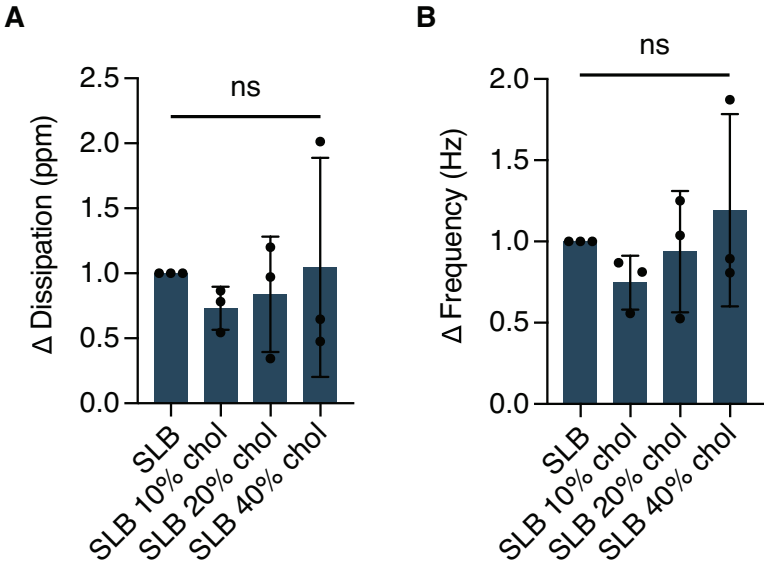


**Figure 4.33: Quantification of affinity of Omicron MiniVs to SLBs containing cholesterol.** Quantification of energy dissipation (A) and frequency (B) changes from QCM-D experiments of Omicron MiniVs in contact with SLBs containing cholesterol. Results correspond to the mean ± SD from n = 3 biological replicates. n.s. not significant, analysed using an unpaired two-tailed t-test.

Cholesterol also has effects on the membrane itself. Zeta potential experiments showed that increasing the amount of cholesterol of a liposomal membrane resulted in a more

negative membrane charge.[194] A more negative charge of the plasma membrane might explain the increase of Omicron S and the decrease of Alpha S. Only Omicron S has shown an affinity to negatively charged membranes, as discussed previously in this thesis (Sections 4.2 and 4.3). Further experiments involving synthetic and cellular membranes will need to be performed in order to elucidate the opposite effect of cholesterol on Alpha and Omicron MiniV attachment.

## 4.6 S proteoliposomes

In order to study the effect of the envelope lipid composition on S, I developed a protocol to introduce full-length transmembrane S into lipid vesicles. The protocol was adapted from Rigaud and Lévy and Lussier *et al.*[136,137] In short, detergent-protected full-length Alpha or Omicron S were incubated with vesicles of the desired lipid composition (Table 4.1).

| **Lipid** | **mol%** |
|---|---|
| DOPC | 84% |
| DOPG | 10% |
| Cholesterol | 5% |
| Atto 488 DOPE | 1% |

**Table 4.1:** Proteoliposome vesicle composition

Two lipid species, DOPG and cholesterol, were essential for facilitating the proteoliposome production process. DOPG has a negative charge which will avoid vesicle fusion and aggregation and cholesterol provides stability and impermeability to the final proteoliposomes.[136] Previously, those vesicles had been loaded with detergent, with the aim to later aid in the insertion of the transmembrane S. Following the incubation, S proteoliposomes were formed and they were mixed with nonpolar polystyrene beads to help remove the detergent. The removal of detergent can be monitored by measuring the absorbance of the solution. The absorbance of untreated SUVs (as a negative control) and SUVs, Omicron and Alpha proteoliposomes which had been incubated with the detergent was monitored for up to 22 h. As can be seen in Figure 4.34, after 22 h of incubation, the absorbance curve of the detergent-treated SUVs and both proteoliposomes was indistinguishable to that of untreated SUVs. The small peak at 488 nm corresponds to the fluorescently tagged lipids present in all vesicles. The final step consisted of removing the remaining detergent and unbound protein by flushing the solution through a gel filtration resin.

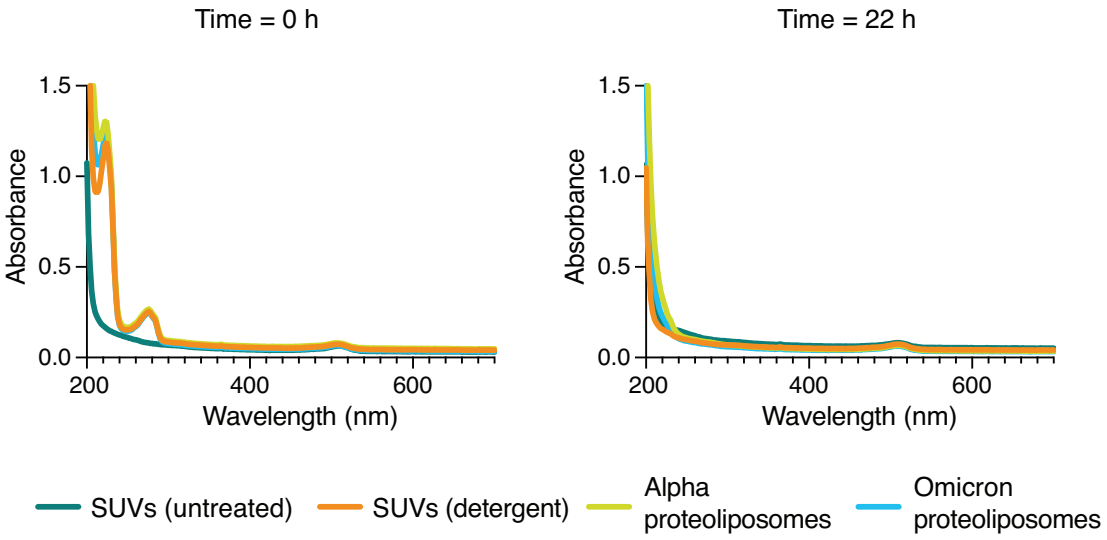


**Figure 4.34: Monitoring of detergent removal.** Absorbance spectrum at time = 0 h and time = 22 h of SUVs and proteoliposomes.

Once the protocol was finished, I measured the size and zeta potential of both proteoliposomes and treated SUVs. As can be seen in Figure 4.35A, both proteoliposome solutions had a diameter that averaged at around 115 nm, while SUVs remained at 90 nm. This was a first indication that the protein had been incorporated into the vesicles. When comparing the zeta potential, SUVs and Alpha proteoliposomes presented a similar charge of -60 mV, while Omicron proteoliposomes showed a more positive charge averaging at -50 mV (Figure 4.35B). This was not surprising as the surface of Omicron S is positively charged in comparison to that of Alpha (Figure 4.2).

To test whether the S inserted in the proteoliposomes was still functional, I conducted a QCM-D experiment. QCM-D showed that both Omicron and Alpha S inserted into proteoliposomes were functional and could bind to the ACE2 receptor, which was bound to an SLB (Figure 4.36). The general lower binding response of Omicron was due to a low amount of protein solution used (in comparison to Alpha S) when producing the proteoliposomes.

The produced S proteoliposomes were in the size range of natural viruses and contained functional S, able to bind to ACE2. Nonetheless, there were still aspects that required optimisation, e.g., the amount of vesicles which did not incorporate any protein. The use of the polystyrene beads and the gel filtration resin aided in the removal of detergent and unbound protein. However, protein-free vesicles probably still remained in the proteoliposome solution.

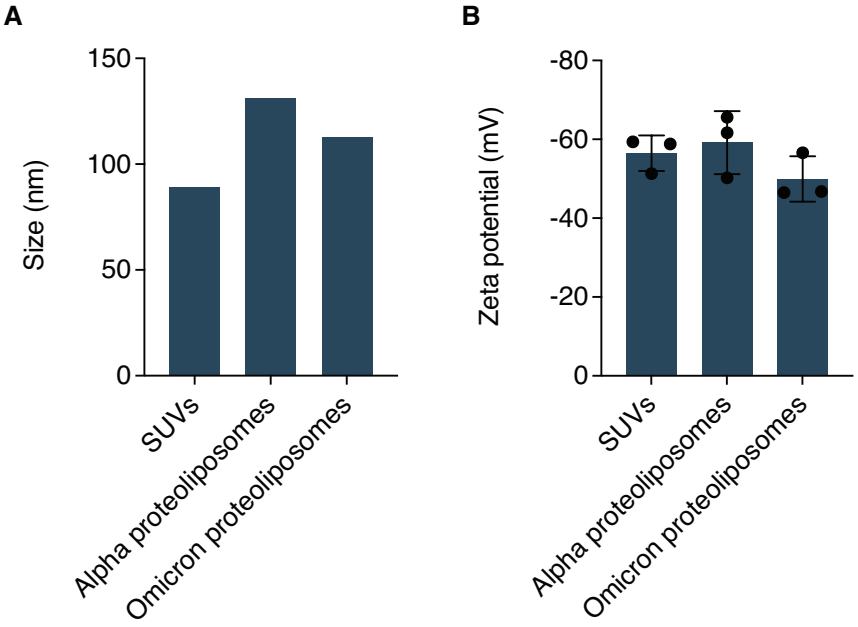


**Figure 4.35: Characterisation of proteoliposomes.** A) Size measurement of Alpha and Omicron proteoliposomes by nanoparticle tracking analysis. B) Zeta potential values of proteoliposomes obtained by dynamic light scattering in MilliQ water. Results on the right correspond the mean ± SD from n = 3 technical replicates.

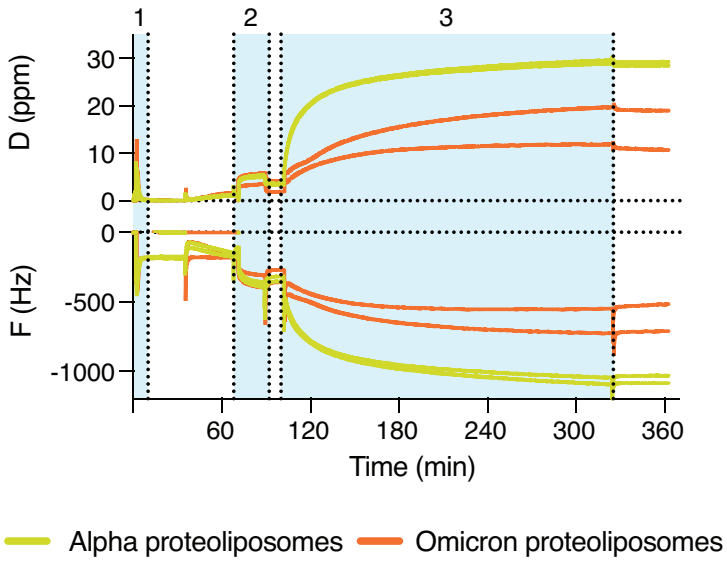


**Figure 4.36: QCM-D of proteoliposomes.** QCM-D experiment of Alpha and Omicron proteoliposomes binding to an ACE2-functionalised SLB. Areas highlighted in blue correspond to: 1. SLB formation, 2. Addition of ACE2 receptor, 3. Addition of Alpha or Omicron proteoliposomes. D is dissipation and F is frequency.

With the aim of minimising the amount of protein-free vesicles, I followed two strategies:

A. Separate proteoliposomes from naive vesicles by immunoprecipitation with anti-S coated beads

B. Reduce the vesicle:protein ratio when producing the proteoliposomes

### 4.6.1 Enhancing proteoliposome efficiency by immunoprecipitation

For the first strategy, I used protein G-coated magnetic beads. Protein G can bind to the Fc domain of antibodies, and thus I could bind an anti-S RBD antibody which would bind to vesicles containing S in their membrane. The collected pellet and supernatant (SN) of Alpha and Omicron proteoliposomes were analysed in terms of size distribution and binding capacity to ACE2. The particles in the SN had a diameter of 100-120 nm, which matched the size of unfunctionalised SUVs (Figure 4.37A). However, the size of the particles in the pellet (which corresponded to everything that bound to the antibody-coated beads) ranged in sizes from 200 nm up to 2.5 $\mu$m. Because the vesicles used for the production of proteoliposomes are normally distributed with an average size of 100 nm, this aberrant sizes could stem from detergent-induced vesicle fusion during protein insertion. Furthermore, the polydispersity index of the pellet solutions lay between 0.6-1, which indicated that the size distribution was broad and probably unfit for DLS measurements.

The QCM-D experiment showed that, specifically for Omicron proteoliposomes, the separation using the beads was successful. The pellet obtained from the Omicron proteoliposomes solution presented a much higher binding to ACE2 in comparison to the SN (Figure 4.37B). However, curves for the pellet and SN stemming from the Alpha proteoliposome solution did not differ much from each other. This could be due to a lower antibody affinity for Alpha S and, thus, a poor separation of the proteoliposomes among the fractions.

Even though there was some removal of naive SUVs from the proteoliposome solution, it was uneven among Alpha and Omicron proteoliposomes. Based on the QCM-D results, the Omicron proteoliposomes population seemed to have properly separated into two fractions of vesicles with high and vesicles with low amount of S into their membrane. However, this did not seem the case for Alpha proteoliposomes, as both SN and pellet fractions showed a similar level of interaction with the ACE2 receptor. Therefore, I could conclude that the success of the immunoprecipitation protocol is dependent on a good-quality antibody that strongly binds to both variants. Another disadvantage of this

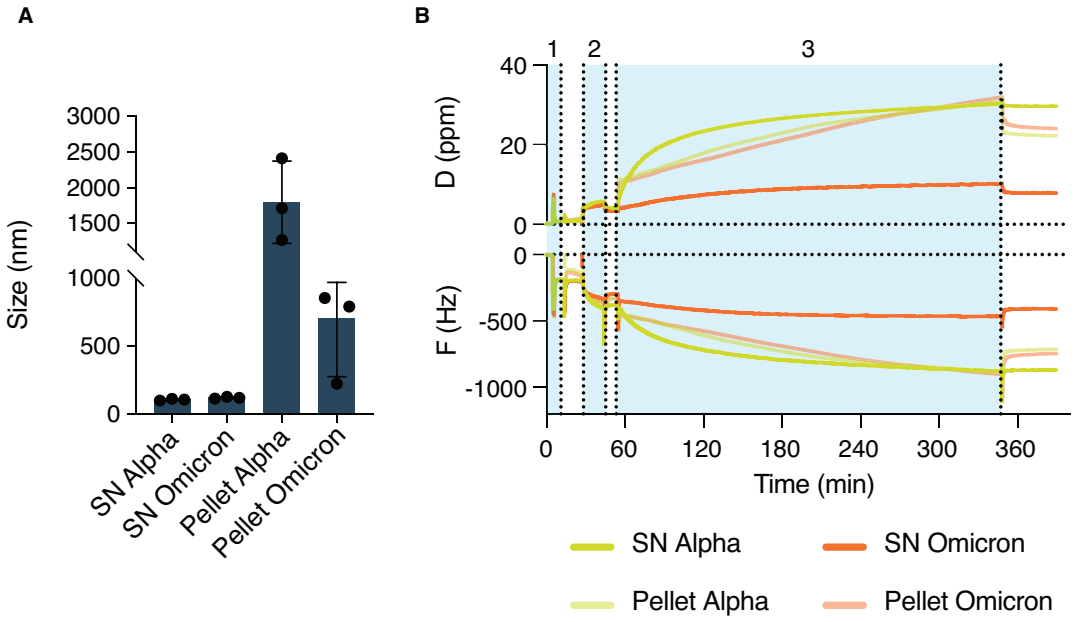


**Figure 4.37: Size and functionality characterisation of immunoprecipitated proteoliposomes.** A) Size measurement by dynamic light scattering of pellet and SN fractions from immunoprecipitated Alpha and Omicron proteoliposomes. Results correspond the mean ± SD from n = 3 technical replicates. B) QCM-D experiment to assess the affinity of the pellet and SN fractions to an ACE2-functionalised SLB. Areas highlighted in blue correspond to: 1. SLB formation, 2. Addition of ACE2 receptor, 3. Addition of pellet or SN of Alpha or Omicron proteoliposomes. D is dissipation and F is frequency.

protocol was the pH of the final elution buffer, which had a value of 2.8. Although the solution was quickly (<5 min) adjusted to pH 7.5, it is known that low pH induces protein denaturing.[195] For all of the aforementioned reasons, I decided to opt for the second approach based on a lower vesicle:protein ratio to minimise the amount of protein-free vesicles.

### 4.6.2 Enhancing proteoliposome efficiency by adjusting vesicle-to-protein ratio

Up to this point I was using a 1:8 (vesicle:protein) ratio based on Rigaud and Lévy.[136] With the aim of minimising the amount of vesicles that do not incorporate any protein, I reduced the amount of vesicles ten times to achieve a final vesicle:protein ratio of 1:80. As a proof of concept, I first created only Alpha proteoliposomes to measure their size and ability to bind to ACE2. I also collected two fractions (A and B) during the filtration process through the gel resin to see if there was actually any difference in terms of removal of unbound protein or amount of naive vesicles. The size appeared to be bigger for the latter fraction (Figure 4.38A) while its concentration was one order of

magnitude lower (Figure 4.38B).

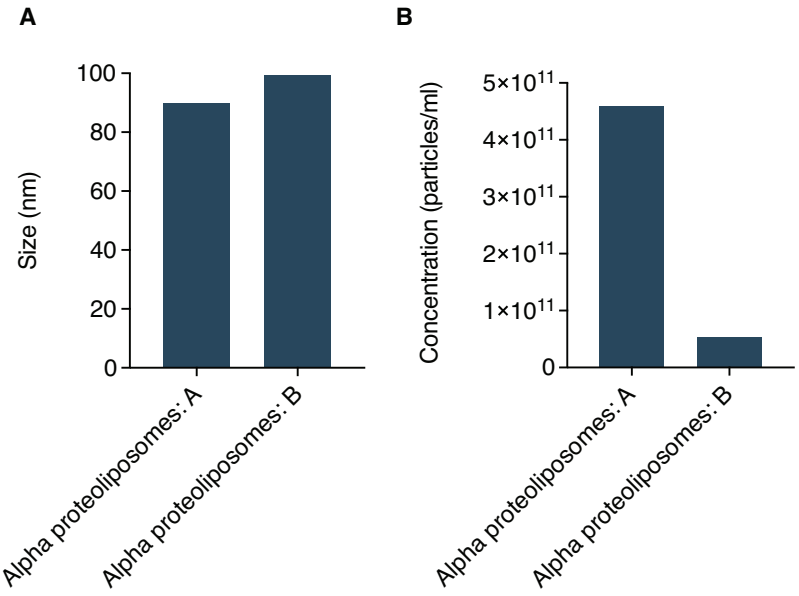


**Figure 4.38: Size and concentration measurements of Alpha proteoliposomes fractions.** Size (A) and concentration (B) of Alpha proteoliposomes fractions by nanoparticle tracking analysis.

Next, I performed a QCM-D experiment to test whether both proteoliposome fractions were able to interact with ACE2. There was no difference in frequency or energy dissipation between fractions, both could bind the ACE2 receptor (Figure 4.39). As I used the same volume from both solutions, and A was one order of magnitude more concentrated, it could be concluded that fraction B presents a higher proteoliposome:naive vesicle ratio or, although less likely, proteoliposomes with a higher S density.

Consequently, I generated both Alpha and Omicron proteoliposomes using the newly developed protocol and utilised the collected B fractions from that point forward. I measured the size of Alpha and Omicron proteoliposomes and observed that the proteoliposome solutions had a bigger diameter than the detergent-treated SUVs which, alongside the previously discussed experiments, indicated a correct incorporation of S into the membrane (Figure 4.40).

Overall, by adjusting the vesicle-to-protein ratio I produced Alpha and Omicron proteoliposomes which had a bigger average size than SUVs and could bind to the ACE2 receptor in a QCM-D experiment. Given the fact that immunoprecipitation was only partially successful for Omicron proteoliposomes and uses a pH range that might potentially affect the functionality of S, I decided to not implement this approach in further experiments. The main goal of the optimisation strategies was to reduce the amount

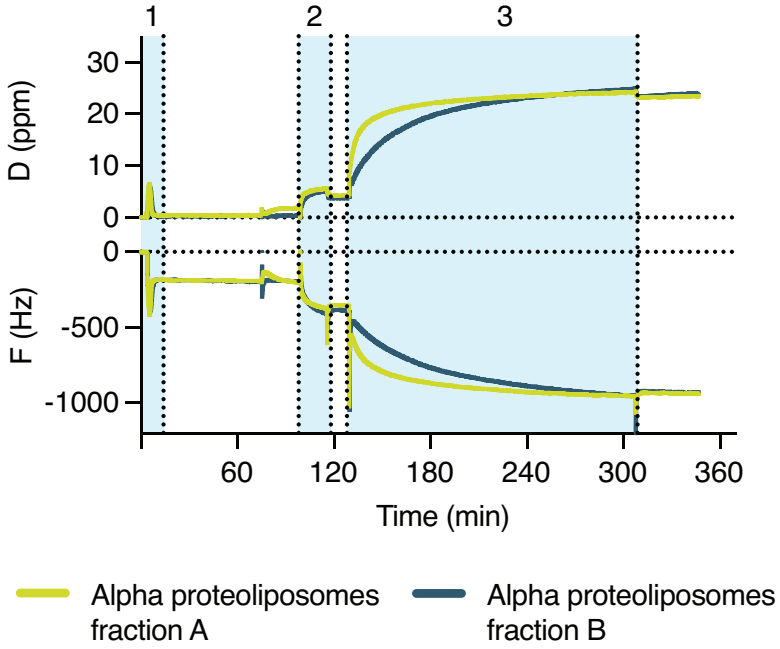


**Figure 4.39: QCM-D of Alpha proteoliposomes fractions.** QCM-D experiment of Alpha proteoliposomes fractions binding to an ACE2-functionalised SLB. Areas highlighted in blue correspond to: 1. SLB formation, 2. Addition of ACE2 receptor, 3. Addition of Alpha proteoliposomes fractions A or B. D is dissipation and F is frequency.

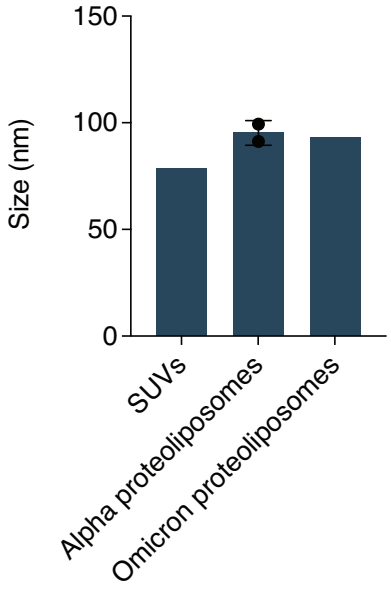


**Figure 4.40: Size measurement of Alpha and Omicron proteoliposomes.** Size of SUVs, Alpha and Omicron proteoliposomes measured by nanoparticle tracking analysis. Results correspond the mean ± SD from n = 2 biological replicates, where applicable.

of vesicles which did not incorporate any protein. To achieve that, I increased the protein:vesicle ratio and separated the fractions obtained during the gel filtration process. I could obtain a population of proteoliposomes which, despite containing less vesicles, showed a very high binding response to ACE2 in QCM-D. This indicated a higher incorporation of S into the general vesicle population.

### 4.6.3 Assessing proteoliposome functionality by flow cytometry

After testing the proteoliposomes on QCM-D, I investigated their ability to bind to cells with and without ACE2 receptor expression (Vero E6 and A549, respectively). With that aim, I incubated SUVs, Alpha and Omicron proteoliposomes with both cell lines. Surprisingly, Alpha proteoliposomes showed a significantly lower interaction than the SUVs when incubated with Vero E6 cells. On the other hand, Omicron proteoliposomes exhibited the highest affinity among all three conditions (Figure 4.41).

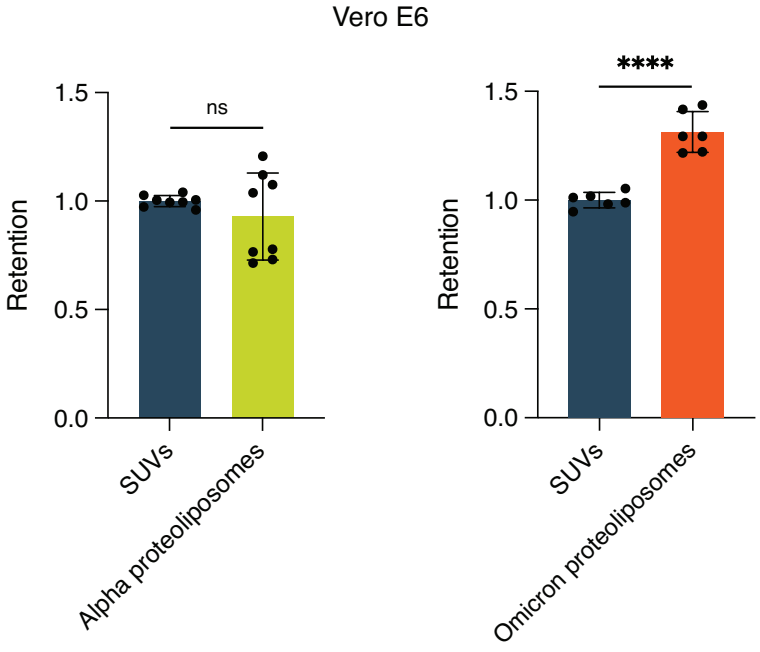


**Figure 4.41: Attachment of Alpha and Omicron proteoliposomes to Vero E6 cells.** Quantification of SUVs, Alpha and Omicron proteoliposomes attached to Vero E6 cells by flow cytometry. Retention is calculated by normalising the fluorescence values relative to SUVs. Results correspond to the mean ± SD from, at least, n = 3 biological replicates. $****p < 0.0001$, n.s. not significant, analysed using an unpaired two-tailed t-test.

The results for Omicron proteoliposomes were similar when looking at A549 cells, showing a significant increase in attachment when compared to SUVs. However, the difference in attachment between Alpha proteoliposomes and SUVs was even more

pronounced than in the previous cell line (Figure 4.42), probably due to the lack of ACE2 receptor expression in A549 cells.

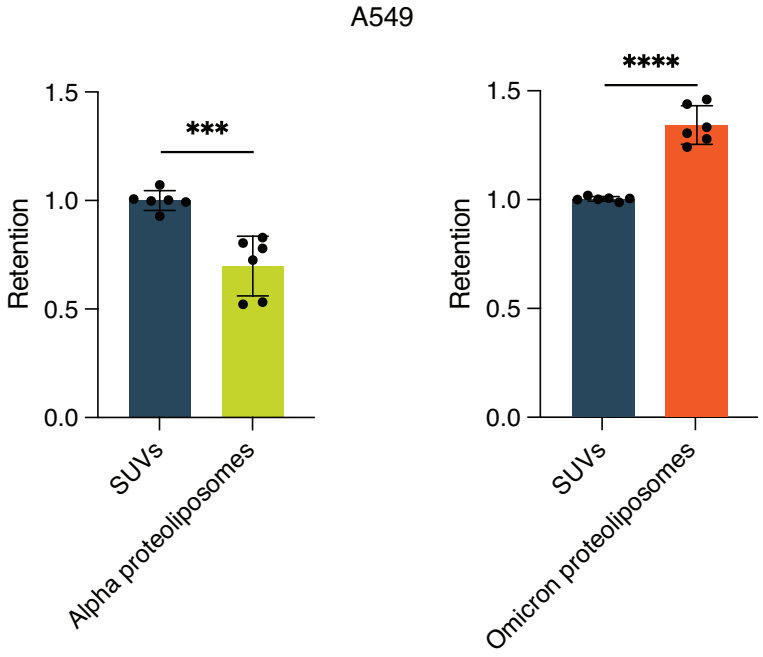


**Figure 4.42: Attachment of Alpha and Omicron proteoliposomes to A549 cells.** Quantification of SUVs, Alpha and Omicron proteoliposomes attached to A549 cells by flow cytometry. Retention is calculated by normalising the fluorescence values relative to SUVs. Results correspond to the mean ± SD from n = 3 biological replicates. $***p < 0.001$, $****p < 0.0001$ analysed using an unpaired two-tailed t-test.

It was unexpected that the detergent-treated SUVs exhibited an affinity for the cells nearly as high as that of the proteoliposomes, and in some cases, even higher than the Alpha ones. Considering that all detergent had been removed as observed in the absorbance assay (Figure 4.34), I decided to repeat the flow cytometry including naive SUVs (not detergent-treated) and MiniVs with the same lipid composition as the proteoliposome membrane. If the detergent had been completely removed, the SUVs should show a similar level of interaction as the detergent-treated SUVs.

Both Omicron and Alpha MiniVs showed a much higher affinity for Vero E6 cells than SUVs, as these cells present ACE2 receptor (Figure 4.43). As expected, in A549 cells only Omicron MiniVs showed a greater interaction, as discussed in previous sections (Figure 4.43). Seeing how the functionalisation of vesicles with Omicron and Alpha S induced more interactions with the cell membrane (specially when ACE2 is present) indicated that there were still aspects to improve in the proteoliposome production process, specially in terms of detergent removal. These results demonstrate that the high

interaction between detergent-treated SUVs and the cell does not stem from the lipid composition of the proteoliposomes, as SUVs with that same composition showed less affinity than MiniVs (Figure 4.43).

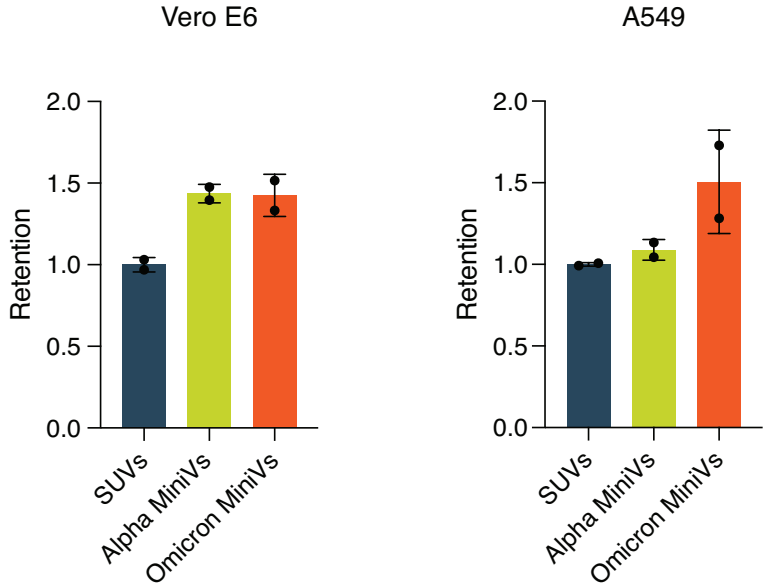


**Figure 4.43: Attachment of SUVs, Alpha and Omicron MiniVs with proteoliposome composition to Vero E6 and A549 cells.** Quantification of attachment of SUVs, Alpha and Omicron MiniVs, with proteoliposome membrane composition, incubated with Vero E6 (left) and A549 (right) cells by flow cytometry. Retention is calculated by normalising the fluorescence values relative to SUVs. Results correspond to the mean ± SD from n = 2 technical replicates.

Altogether, these results indicated two possible origins for this lack of affinity difference between detergent-treated SUVs and proteoliposomes. One reason could be that the detergent had not been fully removed from the membrane and induced more binding between the vesicle and the cell membrane. Even though the absorbance measurements showed no difference between detergent-treated SUVs and naive SUVs after 22 h, it might be possible that the instrument used was not sensitive enough. Another reason could be that S in the proteoliposome membrane was not very stable over time or that it was found in insufficient amounts. However, the results obtained with Omicron proteoliposomes spoke against it.

Since the aim is to study the interactions between Alpha and Omicron proteoliposomes and the cells, I needed to reduce the cell affinity of detergent-treated SUVs. As discussed in the previous section, modifying the lipid composition of the MiniVs to 100% DOPC reduced the background of SUVs binding to cells (Figure 4.23). I followed the same approach and produced proteoliposomes with a lipid composition of 100% DOPC. The

results in Vero E6 cells followed the same trend as the ones obtained with MiniVs (Figure 4.43). Omicron and Alpha proteoliposomes exhibited the highest retention on the cells, while SUVs showed the lowest (Figure 4.44). Also mimicking MiniVs, only Omicron proteoliposomes could show more affinity to the A549 cells than SUVs (Figure 4.44).

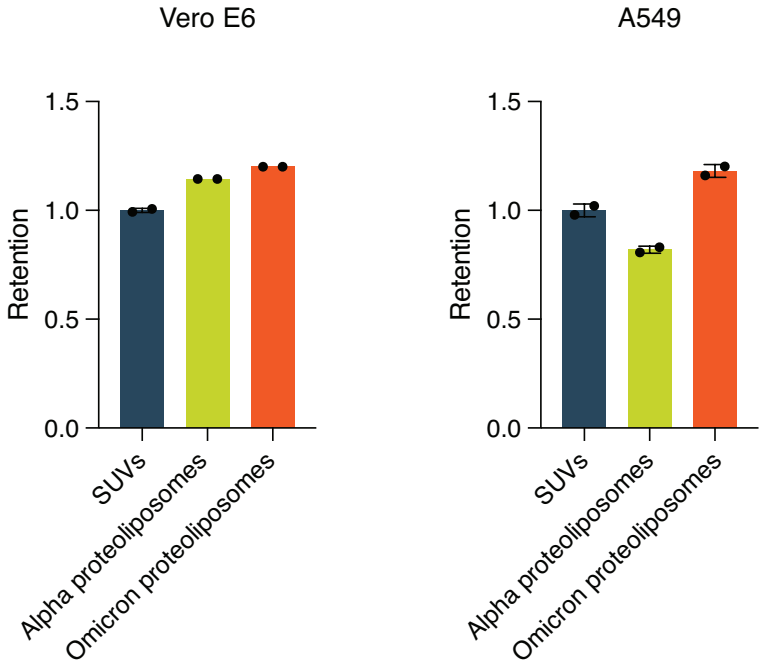


**Figure 4.44: Attachment of SUVs, Alpha and Omicron proteoliposomes with DOPC composition to Vero E6 and A549 cells.** Quantification of attachment of SUVs, Alpha and Omicron proteoliposomes, with a membrane composed of only DOPC, incubated with Vero E6 (left) and A549 (right) cells by flow cytometry. Retention is calculated by normalising the fluorescence values relative to SUVs. Results correspond to the mean ± SD from n = 2 technical replicates.

Despite partially recovering the results obtained with MiniVs, the background binding of SUVs was still significant, specially when compared to non detergent-treated SUVs (Figure 4.45). Due to the composition of both detergent-treated and naive SUVs being the same (in the present case, DOPC), the only cause for the difference in cellular affinity can be residual detergent present in the membrane. These results indicate that the origin of the high affinity of detergent-treated SUVs with the cells is not their membrane composition.

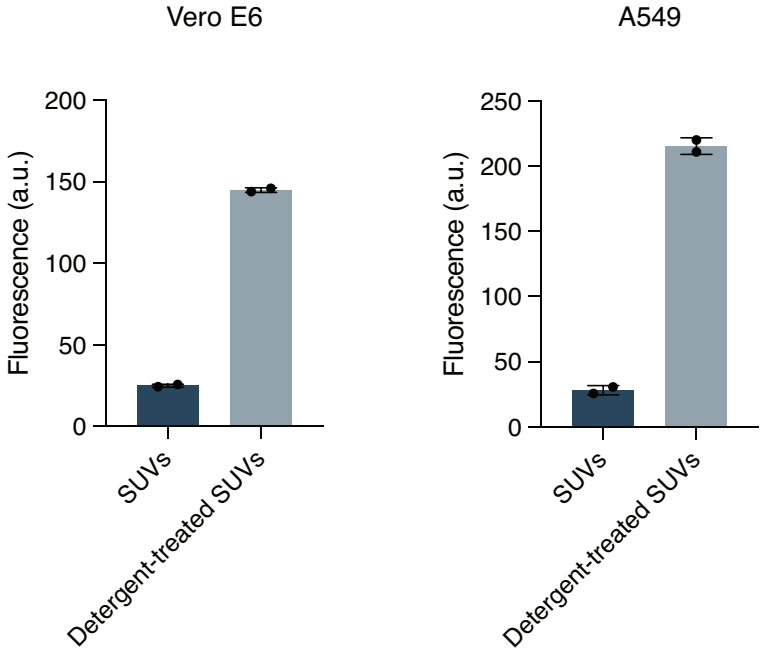


**Figure 4.45: Attachment of DOPC SUVs and DOPC detergent-treated SUVs to Vero E6 and A549 cells.** Quantification of attachment of DOPC SUVs and DOPC detergent-treated SUVs incubated with Vero E6 (left) and A549 (right) cells by flow cytometry. Results correspond to the mean ± SD from n = 2 technical replicates.

Altogether, the results discussed in this section demonstrate that proteoliposomes containing functional S can be produced and bind to ACE2 in synthetic membranes (QCM-D) and natural ones (Vero E6 and A549). However, there are some aspects that need to be optimised, such as the detergent removal and the amount of vesicles not incorporating S.

The protocol used here to obtain S proteoliposomes is not the only way of producing a lipid compartment containing transmembrane S protein. An approach that yields similar results is the production of EVs in cells expressing S.[115] Although their size is comparable to the proteoliposomes created here, their lipid and protein composition cannot be precisely controlled, as these parameters will vary depending on the cell type used for production.[196] Cell passage and culturing conditions might also influence the final composition and yield of the purified EVs, as it was reported that differences in cell passage and seeding density reflect on EV production and bioactivity.[197] A similar methodology was used to produce cell-derived proteoliposomes. This was achieved by inducing blebbing of the plasma membrane in a cell expressing the hemagglutinin fusion protein of the influenza virus.[198] However, in neither of these two methods the lipid or protein composition of the final lipid compartment can be fully controlled. Nevertheless, producing proteoliposomes from blebs or through EV engineering eliminates

the requirement of detergent membrane solubilisation.

Pseudoviruses and VLPs mimicking the SARS-CoV-2 virus have also been extensively studied.[162,163] One advantage they provide is the possibility of including other proteins present in the natural virus, such as the membrane and envelope protein. On the other hand and similarly to EVs, their lipid composition cannot be fully controlled as it is dependent on the host cell they bud from.[74] Moreover, in all the aforementioned methods cells are needed to generate the virus-mimicking particles, while S proteoliposome production is cell-free.

The baculovirus gene expression system provides an alternative to conventional proteoliposome preparation methods. Budded viruses are infectious baculovirus virions which bud from the plasma membrane and are in charge of cell-to-cell infection spread. These can be modified to express the target viral protein for later fusion with synthetic liposomes. One remaining disadvantage is the need to keep some type of fusion protein (e.g. the baculovirus endogenous fusogenic GP64 protein) that will mediate the fusion between the budded virus and the liposome. The method provides other advantages in comparison to standard proteoliposome protocols: it is free from detergent, can ensure directionality of the transmembrane proteins and can be performed with all types of liposomes (SUVs, LUVs or GUVs).[199]

There is one last approach which yields S proteoliposomes that are produced in a very similar way to the proteoliposomes used in the experiments presented in this work. The main difference between both methods is the use of ghost red blood cells (gRBCs) instead of liposomes. However, the process of obtaining gRBC is more complicated and time-consuming than creating liposomes and, furthermore, their lipid and protein composition cannot be controlled.[200]

Overall, there are several methods to obtain lipid vesicles containing viral proteins in their membrane, which mimic the external appearance of a natural virus. More traditional ones include VLPs and pseudoviruses, while recent approaches make use of cellular EVs and gRBCs. Many of these methods provide high production yield and complexity, as they can incorporate more viral proteins than just S. The proteoliposome approach presented here brings control over the system, in terms of lipid and protein composition. However, there are still aspects that remain to be improved, such as complete detergent removal, control over insertion rate and directionality of S.

### 4.6.4 Proteoliposomes of different lipid composition

One final aspect that I did not cover previously, was the effect of the lipid composition of the proteoliposomes on S. Up to this point, I was using vesicles with DOPC as a main component, DOPG and cholesterol. While the negative charge of DOPG prevents vesicle fusion and aggregation, cholesterol ensures stability. However, the composition of the viral envelope is very diverse, as covered previously in this thesis (Figure 4.1). For that purpose, I set out to create vesicles of different composition with the aim of later using them to produce proteoliposomes with a more complex lipid composition.

I started with the base composition (Table 3.1) used for MiniVs which resembles that of SARS-CoV-2 and created vesicles modifying one component at a time. This approach allowed me to study the individual contribution of each lipid species. One readily used characteristic to define membranes is fluidity, which is what I first measured. To that end, I used the fluorescent probe laurdan. The emission spectra of laurdan undergoes a red shift depending on the polarity of its environment, a property which can be exploited to distinguish membranes with different degrees of organisation.[150,182] Due to this intrinsic property, I inserted laurdan into SUVs of different composition to have a relative measure of their fluidity. I used control composition SUVs (see Table 3.1), lacking DOPI, as a starting point, and removed or doubled the mol% of cholesterol, SM and DOPS (Figure 4.46). From the spectrum, a general polarisation (GP) value can be calculated which compares the difference in intensity at 440 and 490 nm (see equation 3.4). A high or low GP value (ranges from +1 to -1) will correspond to a high or low ordered membrane, respectively.

The graph highlights the importance of specific lipid species in maintaining the fluidity of the original membrane. For instance, reducing or doubling the cholesterol content decreased and increased the GP value by 0.2, respectively, compared to the control composition (Figure 4.46B). On the other hand, modification of the SM content did not induce changes in either the spectrum (Figure 4.46A) or the GP values (Figure 4.46B).

Despite the relevance that each lipid could have on the final envelope composition, not all of them have been investigated. Cholesterol is one of the most researched ones. It was already demonstrated that disruption of cholesterol-rich microdomains on the virions affected the fusion and infectivity abilities of SARS-CoV-2.[68] Another lipid species mentioned to be of relevance by Mesquita *et al* is phosphatidic acid (PA). This phospholipid presents a small headgroup but a bulky tail, which contributes to a negative membrane curvature and could aid in vesicle budding.[68,201] The transition from

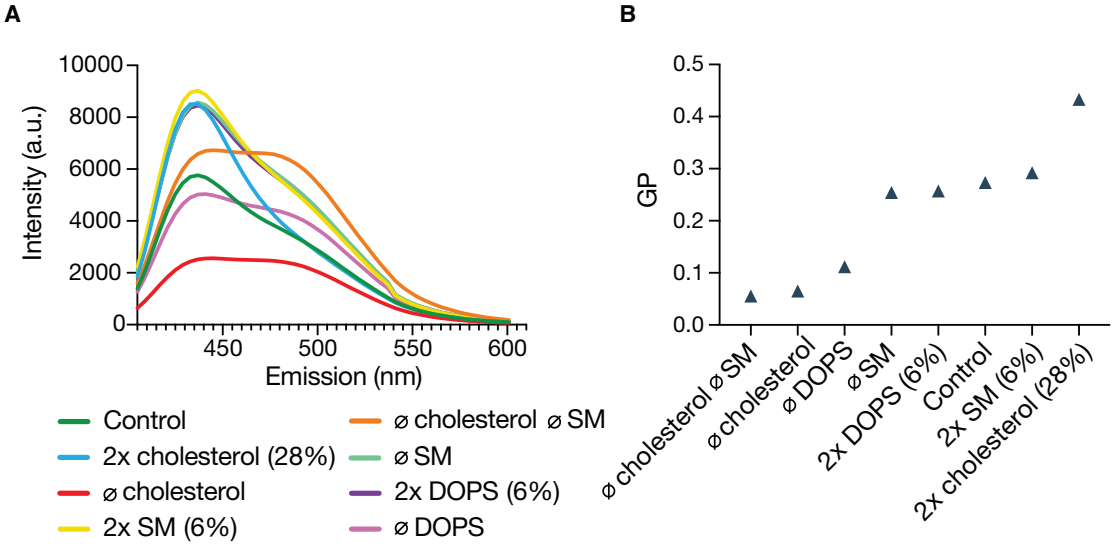


**Figure 4.46: Membrane fluidity of SUV populations of different composition.** Emission spectrum (A) and GP values (B) of laurdan inserted into SUVs of different lipid composition.

a positive membrane curvature into a negative one is an essential step for a successful fusion between the virus and the plasma membrane.[202] For these reasons, I decided to make proteoliposomes with a higher amount of cholesterol or PA. In table 4.2 are detailed the compositions of the three vesicle populations I produced.

| mol% | Normal | PA | Cholesterol |
|---|---|---|---|
| **DOPC** | 75 | 55 | 55 |
| **DOPG** | 20 | 20 | 20 |
| **Cholesterol** | 5 | 5 | 25 |
| **PA** | - | 20 | - |

**Table 4.2:** Vesicle compositions with PA and cholesterol

With these 3 different vesicle populations, I made Alpha proteoliposomes and investigated possible differences in their affinity to the ACE2 receptor using QCM-D. As shown in Figure 4.47, all proteoliposomes populations were able to bind to ACE2. Quantification of frequency changes seemed to indicate that proteoliposomes with a higher content of cholesterol had a higher affinity for the receptor (Figure 4.48A). However, no trend could be spotted when comparing the energy dissipation changes (Figure 4.48B).

Higher binding to ACE2 in the presence of more cholesterol could be explained by protein clustering. It is readily known that cholesterol can control membrane protein organisation in cells. Recently, it has been reported that the Env protein from HIV

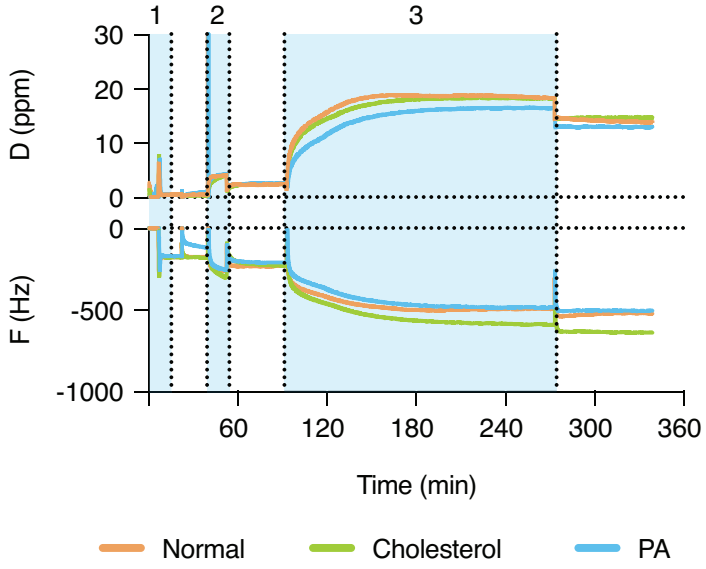


**Figure 4.47: QCM-D experiment of Alpha proteoliposomes of different composition.** Representative QCM-D experiment of Alpha proteoliposomes of different lipid composition binding to an ACE2-functionalised SLB. Areas highlighted in blue correspond to: 1. SLB formation, 2. Addition of ACE2 receptor, 3. Addition of proteoliposomes. D is dissipation and F is frequency.

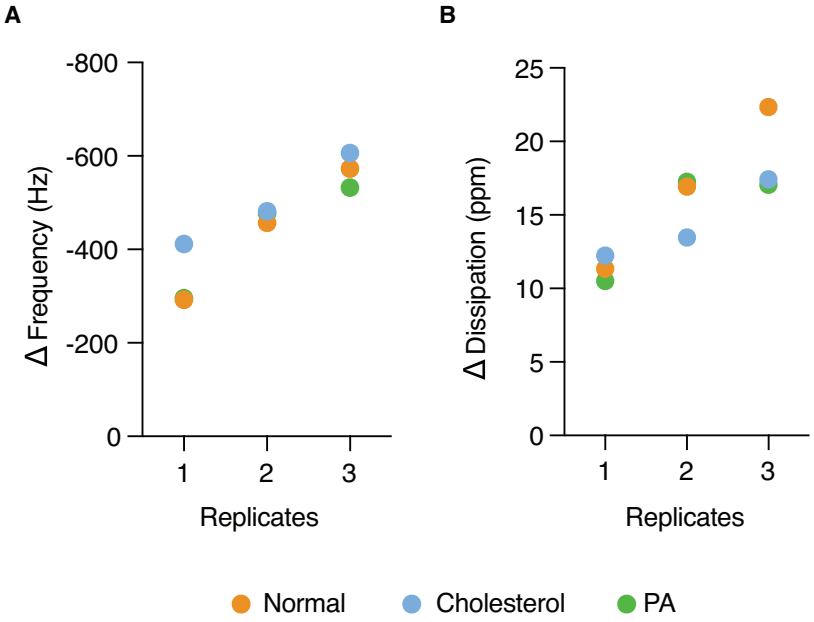


**Figure 4.48: Quantification of QCM-D experiments of Alpha proteoliposomes of different composition** Changes in frequency (A) and energy dissipation (B) of Alpha proteoliposomes with different lipid composition binding to an ACE2-functionalised SLB across all three replicates.

can also form cholesterol-induced clusters on the viral membrane.[203] Clustering in the proteoliposomes could lead to an elevated amount of S available for ACE2 binding,

which would in turn create higher avidity and more attachment recorded in QCM-D. This clustering phenomenon could be an explanation for the results observed with Alpha proteoliposomes with a high cholesterol content.

Another possible reason behind the different behaviour of the proteoliposome populations would be the incorporation rate of Alpha S into the vesicles. As discussed previously in this section, the lipid composition of vesicles determines their stiffness. I showed that cholesterol is the lipid that induces the biggest changes in laurdan emission and, thus, in membrane stiffness (Figure 4.46). The distinct stiffnesses of the produced vesicles might determine the amount of Alpha S that can be incorporated. In that case, stiffer vesicles which contained more cholesterol would have incorporated more Alpha S, and thus showed a higher general affinity to ACE2 as seen in Figure 4.48.

The zeta potential of the membrane could also play a role in protein incorporation. The anionic nature of PA, which adds to the negative charge of DOPG, might have negatively influenced the incorporation of Alpha S into the vesicle, as the protein also presents a negative zeta potential (Figures 4.2 and 4.35).

Altogether, I produced Alpha and Omicron S proteoliposomes and tested several parameters to optimise the method. These proteoliposomes resembled MiniVs and the natural SARS-CoV-2 virus in terms of size, lipid and protein composition and ability to bind to the ACE2 receptor. However, there were still drawbacks, such as incomplete detergent removal from the membrane and limited control over the protein insertion rate. Furthermore, I created Alpha proteoliposomes of various lipid compositions to investigate the individual contribution of lipid species to the functionality of S. I discovered that including cholesterol in the membrane might induce more binding to ACE2. In the future, next experiments should focus on studying the effect that increased membrane cholesterol can induce on Omicron proteoliposomes and their affinity to ACE2.

## 4.7 Cell-free *in vitro* translation of S

Another approach to achieve proteoliposomes is to translate full-length membrane proteins *in situ* in the presence of lipid membranes using cell-free protein synthesis (CFPS).[123,204] CFPS involves the production of proteins *in vitro* using the biological translation machinery without the use of natural living cells. There are several methodologies within CFPS, but one main classification distinguishes between those that use specific purified recombinant elements and those that use cell lysates.[96,205] Depending on the translation needs of the target protein, certain systems may offer advantages over

others. In this case, to ensure proper translation and functionality of S, several specific components were required. Due to the presence of the hydrophobic transmembrane domain of S, I needed the translation to take place in the presence of lipid vesicles, which would mimic the endoplasmic reticulum. Another important element were chaperones, to ensure correct folding of this 136 kDa protein. It has been shown that the activity of specific chaperones is needed for a correct incorporation of S into newly formed virions.[206] For all the aforementioned reasons, I first chose an *in vitro* translation (IVT) system based on a HeLa cell lysate to produce full-length Wuhan S. The HeLa cell lysate contained chaperones and lipid vesicles (endoplasmic reticulum-derived vesicles named microsomes) needed for a potentially successful IVT reaction. The work in this section has been done in collaboration with Elena Bromkamp and Deus Mwesigwa, who did an internship under my supervision.

### 4.7.1 Production of full-length S using a HeLa cell-based system

In order for the HeLa lysate system to work, there are certain requirements that need to be fulfilled. The most important one is to provide a plasmid with the gene of interest flanked by a T7 promoter and the internal ribosomal entry site (IRES) on one side, and a polyA tail and T7 terminator on the other. The IRES is essential for good translation in the absence of an mRNA-cap. With that aim, I chose a plasmid that contained a gene for his-tagged full-length S (pGBW-m4136458 was a gift from Ginkgo Bioworks, USA, and Benjie Chen). I used Gibson cloning to insert the target gene into the provided plasmid in the HeLa lysate kit, which contained all the genetic elements needed for correct transcription and translation. Furthermore, the receiver plasmid contained a green fluorescent protein (GFP) sequence to be incorporated at the C-terminal end of the protein (Figure 4.49A).

When doing electrophoresis of the plasmid in an agarose gel, I could see a band between 6 and 8 kb. The calculated plasmid size was 8.4 kb, and I attributed the small decrease in size to some errors in the cloning method or recombination in the bacteria (Figure 4.49B).

After cloning, I prepared three IVT reactions and incubated them at 30 ºC overnight. The reactions included a positive control, a negative control, and a reaction with the Gibson-cloned S plasmid. The positive control contained a plasmid encoding his-tagged turboGFP (tGFP), while the negative control lacked any plasmid. Since the cloned S gene included a his-tag sequence, I attempted to purify S from the IVT reaction mix using Ni-NTA magnetic beads after the reaction time. One supernatant (SN) and two

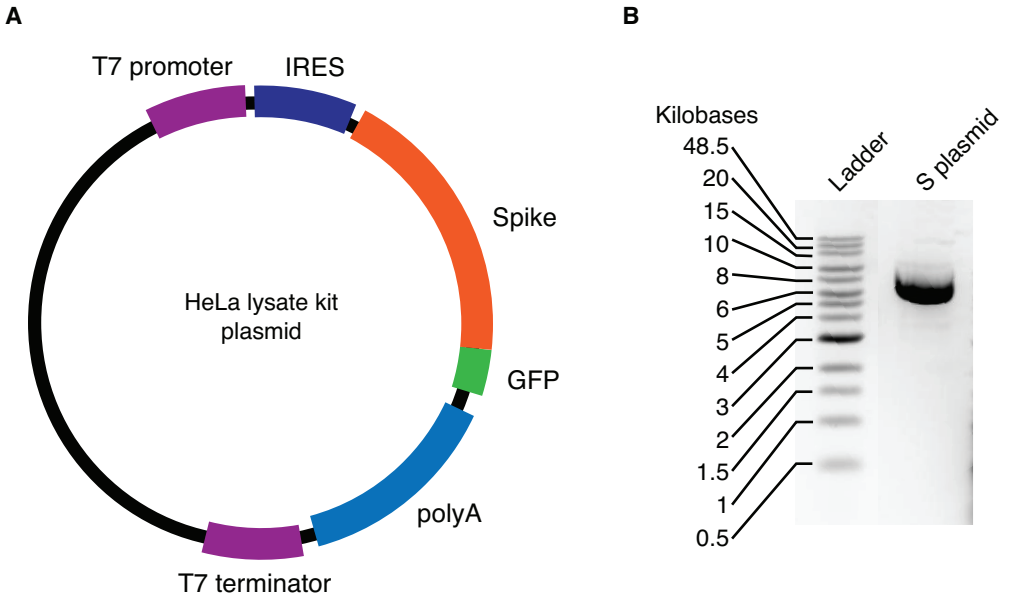


**Figure 4.49: Gibson-assembled plasmid for HeLa lysate system.** Sketch of plasmid obtained by Gibson assembly to use with the cell-free HeLa lysate kit (A) and agarose gel electrophoresis of the plasmid (B).

eluates were collected from each reaction. Next, I performed an SDS-polyacrylamide gel electrophoresis (PAGE) and loaded the SN and the two eluates (Figure 4.50). On the gel it can be observed that the Ni-NTA magnetic beads worked as expected, as all the proteins provided in the IVT kit - which are not his-tagged - can be seen in the loaded SN fractions (Figure 4.50A). Additionally, a band corresponding to his-tagged tGFP (26 kDa) from the positive control reaction can be spotted in both eluates. The negative control reaction also worked as expected as no band could be spotted in the eluate fractions. On the other hand, no band can be observed in eluates corresponding to the reaction containing the S plasmid (Figure 4.50B). Commercially-obtained his-tagged Alpha S was used as a positive control of the size band that should have been visible in the adjacent lanes.

Due to the lack of success in protein translation, I decided to order a full-length sequencing of the Gibson-assembled plasmid. Previously, I had only checked the first and last 1 kb of the S gene, which proved that the gene had been inserted into the plasmid. The new sequencing proved that the gene coding for S and the T7 promoter had been successfully cloned. However, the IRES, polyA and the T7 terminator were missing. Instead of the IRES, I could find a bacterial ribosomal binding site (RBS). This could explain the lack of success in translating S, as all three missing elements were crucial for protein translation using the HeLa lysate IVT kit. One reason behind the missing IRES and the simultaneous insertion of the bacterial RBS could be recombination in the

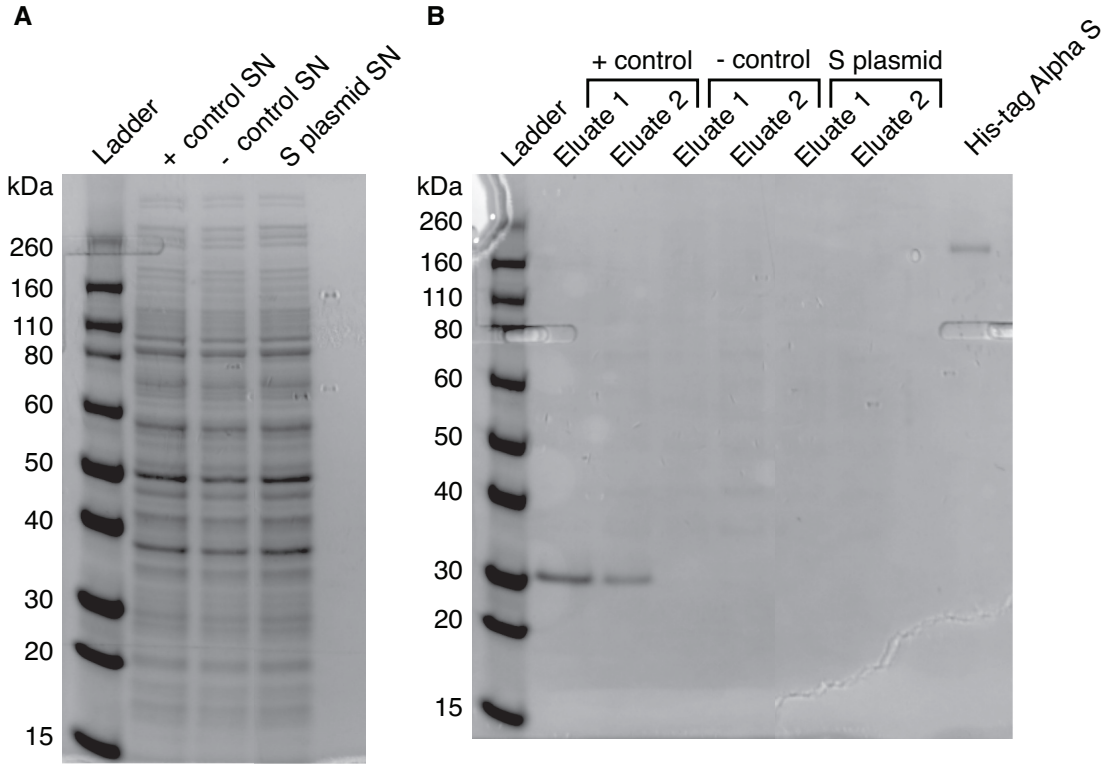


**Figure 4.50: Gel electrophoresis of purified HeLa IVT reactions.** SDS-PAGE of Ni-NTA purified SN (A) and eluate (B) fractions from HeLa IVT reactions (positive and negative controls and the S plasmid reactions).

bacteria during plasmid amplification. Even though I used a recombination-deficient DH5$\alpha$ strain, there are other parameters which can affect recombination, such as bacteria growth temperature.[207]

After several rounds of failed cloning by Gibson or restriction site assembly, I decided to outsource the plasmid production. Despite obtaining correct plasmids (from two different sources, named here plasmids A and B) which contained all the required elements for the HeLa lysate-based IVT reaction to work, I was not able to see any band corresponding to the size of S when performing SDS-PAGE (Figure 4.51). I performed the same purification with the Ni-NTA beads as previously described and did SDS-PAGE of the eluates. Again, commercially-obtained his-tagged Alpha S was used as a positive control of the size band of S. From the images it can be observed that the reaction and purification still worked, as the tGFP band corresponding to the positive control can be clearly spotted. However, there seemed to be no trace of a band belonging to S (Figure 4.51).

Proteins reported to be expressed with such a kit are, in many cases, about half the size of S (136 kDa).[208,209] This might explain, partially, the unsuccessful translation of S.

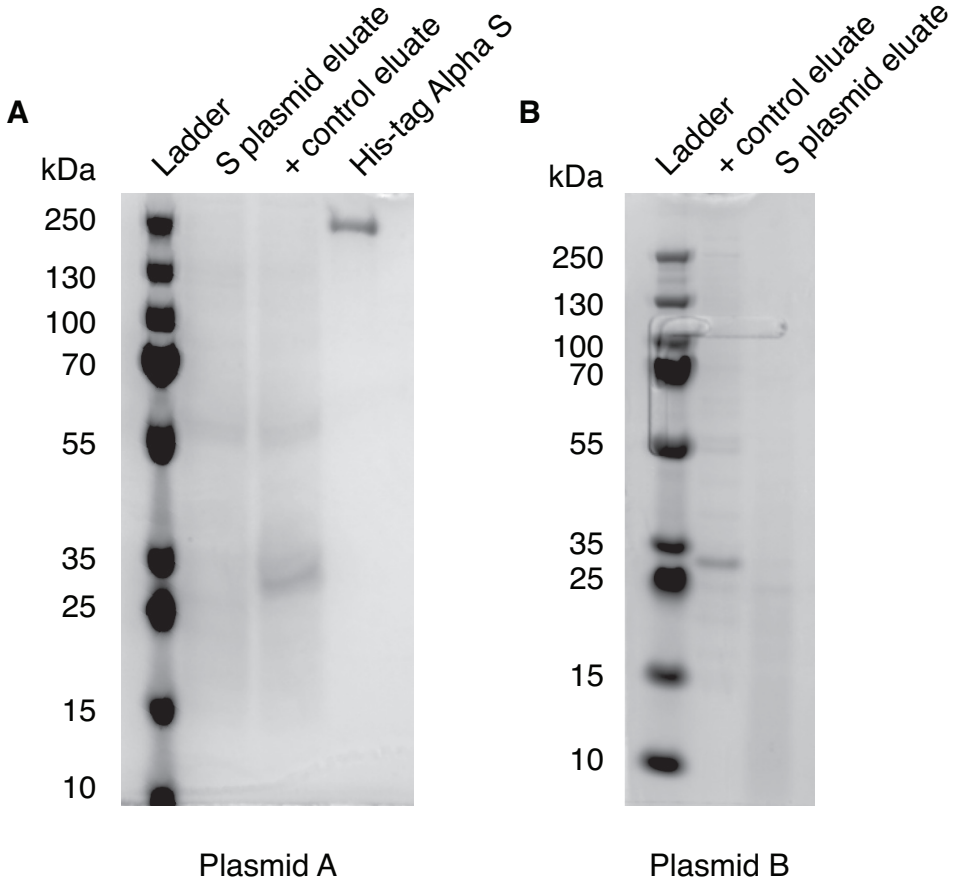


**Figure 4.51: Gel electrophoresis of purified HeLa IVT reactions performed with the new plasmids.** SDS-PAGE of Ni-NTA purified eluate fractions from HeLa IVT reactions (positive control and S plasmid reactions) with the new plasmids A (A) and B (B).

It could also be the case, that the protein is translated but in insufficient amounts, so it cannot be detected in the SDS-PAGE. Coomassie blue staining has a sensitivity of 0.5 $\mu$g of protein and the HeLa IVT kit used can produce yields up to 100 $\mu$g/ml.[210] Due to the reaction mix volume being so small (25 $\mu$l), the maximum protein yield achievable was 2.5 $\mu$g. Ramm *et al* achieved expression of non-structural, structural and accessory proteins from SARS-CoV-2, including S, using a Chinese hamster ovary cells (CHO) lysate. However, expression of S was still low ($\sim$ 8 $\mu$g/ml) and was visible by autoradiography of an SDS-PAGE gel.[211] The sensitivity of autoradiography is much higher than that of coomassie blue staining, up to one order of magnitude, and this might explain their success detecting the production of S in an SDS-PAGE.[212] Other reasons why S was not produced might be poor quality of the DNA plasmid or degradation of the mRNA. The plasmid was precipitated using ethanol, which removes trace amounts of inhibitor or salts acquired during the plasmid purification process. mRNA is susceptible

to RNAses; yet, the kit's tGFP positive control was always translated. This was probably a good indication of a clean RNAse-free environment. Altogether these results indicate that, due to the fact that the all the requirements for a successful reaction were met, S might have been translated but in insufficient and, thus, undetectable amounts.

### 4.7.2 Production of full-length S using an *E. coli*-based system

After failing to translate and/or detect the protein with the HeLa lysate, I decided to test a simpler system. PURExpress (New England Biolabs) is an *in vitro* protein synthesis kit based on the PUREsystem (Protein synthesis Using Recombinant Elements).[97] It contains all the necessary components, purified from *E. coli*, to perform both transcription and translation. It also makes use of the T7 promoter, rendering it ideal for protein production using my previously cloned plasmid. When performing Gibson cloning, as discussed above, the receiver plasmid lost the IRES site but gained a bacterial RBS including a partial Shine-Dalgarno sequence (AGGAGA instead of AGGAGG), which helps recruit the ribosome. Given all these reasons, I decided to set up an IVT reaction using the PURExpress kit. I included the kit's GFP positive control and the tGFP positive control from the HeLa lysate kit, which should yield no protein as it contains no RBS. After overnight incubation at 37 ºC, I performed an SDS-PAGE. The PURExpress GFP positive control showed a clear band at around 30 kDa (Figure 4.52). Another band could be observed from the reaction containing the S plasmid, at around 140-150 kDa which is consistent with the molecular weight of one S monomer (Figure 4.52). The lack of a tGFP band from the HeLa lysate positive control is a good proof of the specificity of the system, which is not able to transcribe and translate proteins from DNA lacking the bacterial RBS.

To further ensure the band corresponded to S, I cut out the band from the gel and sent it for mass spectrometry analysis. Within the almost 1400 aminoacid residues that form S, 37 peptides that covered around 30% of the sequence were detected (Figure 4.53). More importantly, the coverage of the peptides stretched all along the S peptide sequence, which was a good indicator that the full protein had been translated. To ensure that the peptides truly corresponded to S, I compared some detected peptides against the expression (*E. coli*) and origin (SARS-CoV-2) proteomes. Finding a unique peptide allows for an unambiguous identification of S. For that purpose, I performed a protein BLAST (basic local alignment search tool) to compare the peptide "LQDVVNQNAQALNTLVK" detected in the mass spectrometry experiment to the proteome of both *E. coli* and SARS-CoV-2. The sequence was chosen as it is long enough to diminish the probability being found in the *E. coli* proteome by chance.

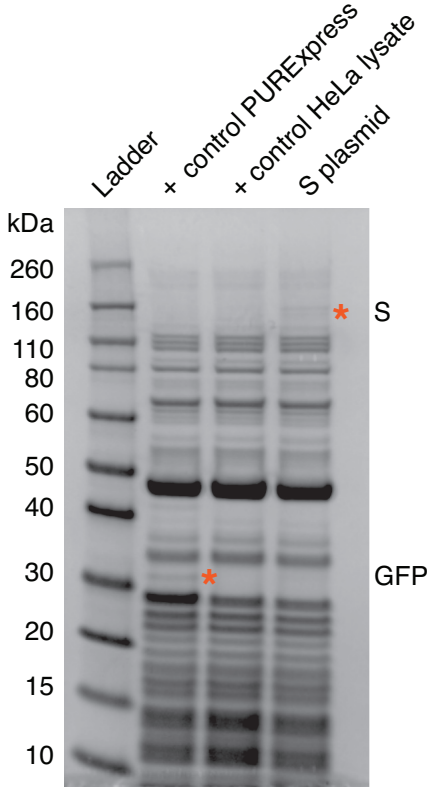


**Figure 4.52: Gel electrophoresis of PURExpress reactions.** SDS-PAGE of PURExpress reactions: positive control from PURExpress and HeLa kits and S plasmid reactions. Orange stars indicate the bands corresponding to S and to GFP.

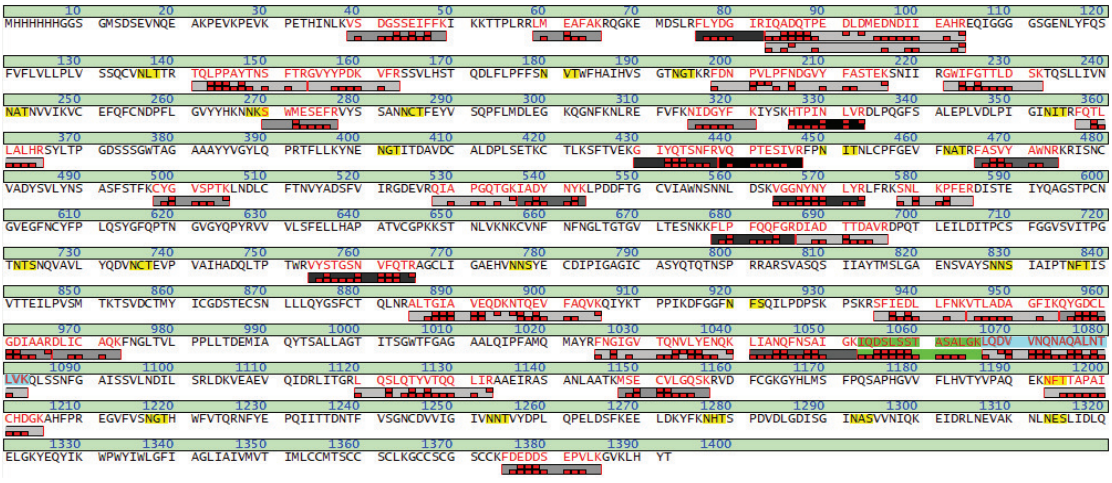

**Figure 4.53: Peptide mapping of S.** The aminoacid sequence of S is in black, the mass spectrometry-detected peptides in red. Red rectangles indicate the amount of peptide hits in that sequence area. An area with high coverage is highlighted in green as an example, while the selected peptide for pBLAST is shown in cyan. The NXT/S motifs in yellow are the N-glycosylation sites of the protein.

The results from the first three hits with the highest score from the pBLAST against SARS-CoV-2 and *E. coli* are summarised in table 4.3 and table 4.4, respectively. pBLAST provides a series of scores that correlate to the percentage of identity and coverage of the provided peptide sequence with the target organism. One of them is the E-value, which describes the number of expected hits found by chance that hold a similar score. In summary, a lower E-value indicates a more reliable hit. The E-values obtained when comparing the peptide sequence to the viral genome is orders of magnitude lower compared to those obtained with *E. coli*. Despite the fact that the identity of two out of the three hits found in the bacterial proteome is 100%, their coverage is low. This means that the peptide sequence is only partially detected in the found protein hit. Altogether, these results identified the purified gel band as the S from SARS-CoV-2 and proved that S was successfully translated by the *E. coli*-based IVT kit.

| Description | Species | Coverage (%) | E-value | Identity (%) | PDB |
|---|---|---|---|---|---|
| **Chain A, S S2** | SARS-CoV-2 | 100 | 2e-08 | 100 | 7R95A |
| **Chain A, S S2'** | SARS-CoV-2 | 100 | 2e-08 | 100 | 6X45A |
| **Chain B, S** | SARS-CoV-2 | 100 | 2e-08 | 100 | 7LX5B |

**Table 4.3:** First three hits with highest score from pBLAST of mass spectrometry peptide against the SARS-CoV-2 proteome.

| Description | Species | Coverage (%) | E value | Identity (%) | Reference |
|---|---|---|---|---|---|
| **SCP2** | *E. coli* | 47 | 52 | 100 | HCO5180341.1 |
| **YadA** | *E. coli* | 76 | 53 | 100 | WP171460152.1 |
| **GPO** | *E. coli* | 82 | 74 | 58.82 | WP253180027.1 |

**Table 4.4:** First three different hits with highest score from pBLAST of mass spectrometry peptide against the *E. coli* proteome.

The success of the prokaryotic against the eukaryotic method can be mainly explained by the protein production efficiency. The yield produced by the PURExpress system can go up to 200 $\mu$g/ml, which is double the yield of the HeLa lysate kit. This concentration translates to a maximum protein amount of 5 $\mu$g in a 25 $\mu$l reaction volume. Another advantage of using a prokaryotic system is the lack of lipid structures it contains. Lysates from cultured cell lines usually contain microsomal structures, endoplasmic reticulum-derived vesicles.[213] Supplementation of the system with some kind of lipid membrane might be necessary for the correct translation and folding of a membrane protein, in this case, full-length S. The presence of microsomes in the HeLa lysate implies that, if the protein were to be translated and incorporated into a microsome, there would be no control over the lipid composition of such membrane. However, by using a system which

lacks these structures, vesicles of the desired lipid composition could be supplemented. Specifically in the case of viral proteins, Hu *et al* demonstrated recently the expression and integration into liposomes of two proteins from the deadly Nipah virus. Moreover, they prove the importance of vesicle lipid composition for the incorporation of the protein in its membrane.[123] To express membrane proteins in an *E. coli*-based system is challenging as it is not particularly well suited to produce them, specially if they are complex.[214] However, several research groups have successfully produced membrane proteins using the PURE system.[123,215,216]

In summary, I have tested one eukaryotic- and one prokaryotic-based cell-free system with the aim to translate full-length S. Despite providing all the necessary components, the eukaryotic system based on a HeLa lysate did not yield any detectable protein probably due to low translation efficiency. On the other hand, the prokaryotic system which used recombinant elements from *E. coli* successfully produced full-length S, with its identity confirmed by mass spectrometry. In the future, next steps will involve incorporating S into supplied liposomes with varying lipid compositions and testing the protein's functionality in binding to ACE2, functionalised on synthetic membranes and in cells. The technology introduced here advances us closer to synthetically replicating the entire SARS-CoV-2 viral cycle, without the need of using living cells.

# 5 Summary

## 5.1 Omicron S affinity to negatively charged lipid membranes

This work focused on the role of lipid species in the attachment process of SARS-CoV-2. Towards this end, I designed and assembled synthetic miniviruses, named MiniVs, which allowed me to investigate aspects of the viral infectivity in low biosafety level environment. MiniVs are based on SUVs functionalised with his-tagged Alpha or Omicron S, that have a similar size and zeta potential to those of the natural SARS-CoV-2 virus.

Viral infection starts when S binds to the ACE2 receptor on the cell membrane. Therefore, to test the binding ability of MiniVs to ACE2 I performed a QCM-D assay and showed that both Omicron and Alpha MiniVs could bind to the receptor. As expected, the assay revealed that Omicron S had a higher affinity to ACE2 in comparison to Alpha S. Moreover, Omicron S presented an interaction with the negatively charged lipid membrane. I also demonstrated that Omicron S has a higher affinity for the unfunctionalised lipid membrane compared to Alpha S, and quantified its $K_D$ at 35.47 and 59.58 nM, respectively. This affinity can be attributed to the electrostatic potential surface of Omicron S. The high amount of mutated aminoacid residues on Omicron S RBD make its surface more positively charged when compared to Wuhan or Alpha S. Consequently, this change made the protein more susceptible to interaction with negatively charged membranes.

Similar results were obtained when SLBs were replaced by GUVs that better mimic the plasma membrane. Moreover, producing GUVs with a positively charged membrane and encapsulating both Omicron and Alpha MiniVs yielded the opposite results. Only Alpha MiniVs were able to bind to the membrane. Finally, I used Vero E6 and A549

cell lines, with high and low ACE2 presentation, respectively. Flow cytometry analysis of the attachment of Alpha and Omicron MiniVs to the plasma membrane confirmed the higher affinity of Omicron S for the ACE2 receptor and the negatively charged cellular membrane, consistent with previous experimental observations.

## 5.2 The impact of cholesterol in Omicron and Alpha S binding to the cellular membrane

The next step focused on identifying which plasma membrane components might be responsible for the interaction between Omicron S and the cell membrane. Heparan sulfate, SM and cholesterol were selected as they had been reported in literature to be relevant for the entry and attachment process of SARS-CoV-2. Heparan sulfate appeared to be a good candidate due to its intrinsic negative charge. However, its cleavage from the membrane did not induce any significant changes in the interaction of either Omicron or Alpha MiniVs with the membrane. Similarly, the increase of SM in the plasma membrane caused little effect. In contrast, raising membrane cholesterol levels led to a significant increase in the interaction of Omicron MiniVs. Interestingly, the opposite trend was observed with Alpha MiniVs. I tested whether Omicron S could have an unreported affinity to cholesterol by studying its interaction with SLBs containing increasing amounts of the lipid. However, no direct affinity of Omicron S to cholesterol was observed. The change in membrane affinity of MiniVs when cholesterol levels were elevated was only seen in Vero E6, but not in A549 cells. Given that the latter cell line does not express ACE2 receptor, it could be hypothesised that the increase and decrease in attachment of Omicron and Alpha MiniVs, respectively, might be due to ACE2 receptor reorganisation. This would lead to a higher ACE2 clustering and might have led to more avidity between the cell and the MiniV. However, this would only explain the behaviour of Omicron, but not Alpha MiniVs. Cholesterol was reported to decrease the surface charge of membranes. This effect might explain the disparity of results, as only Omicron S proved to have an affinity for negatively charged membranes.

## 5.3 Optimisation of S proteoliposomes and study of the influence of membrane lipid composition

MiniVs present his-tagged S on their surface, which means that the protein is not inserted into the membrane as it is the case in the natural virus. With the aim to study the influence of specific lipid species on S, I produced proteoliposomes that incorporated full-length S in their membrane. I adapted a protocol by Rigaud and Lévy and Lussier *et al* to produce Alpha and Omicron proteoliposomes, and changed conditions over time to optimise their production in terms of protein incorporation and detergent removal. Proteoliposomes were characterised in terms of size and zeta potential, which were similar to those of MiniVs and the natural SARS-CoV-2 virus. Moreover, the incorporated S remained functional as proteoliposomes showed binding to ACE2 on SLBs, measured by QCM-D, and to cells presenting high and low ACE2 presentation, measured in flow cytometry experiments.

I also investigated the effect of different lipids on S binding to ACE2. I produced Alpha proteoliposomes using SUVs enriched in either PA or cholesterol, two lipid species reported to be relevant in the viral envelope. QCM-D experiments showed a slight increase in attachment of proteoliposomes that contained higher levels of cholesterol, in comparison to the other two populations. This increase in ACE2 affinity could be explained by protein clustering, which might increase the amount of S available for ACE2 binding, resulting in higher avidity and greater attachment. Differences in physical properties of the vesicles, such as zeta potential or stiffness, could also influence the insertion rate of S during proteoliposome formation. This, in turn, could enhance the binding to ACE2 if those proteoliposomes had indeed incorporated more S into their membrane.

## 5.4 Cell-free S expression using eukaryotic and prokaryotic-based systems

IVT provides a platform to produce proteins of interest, with the main requirement being the cloning of a plasmid with the desired gene. In this thesis, IVT has been implemented as a platform to study the cell-free translation of S. Due to the fact that S is a big protein with many glycosylated residues, I first chose an eukaryotic-based system (HeLa lysate) to translate it. I cloned a plasmid with the specifications needed by the HeLa lysate system but I could not detect any band corresponding to S in an SDS-PAGE. When

looking at the results from the plasmid sequencing, I noticed that the element needed for ribosomal binding (IRES) was missing. New plasmids containing the IRES were tested. However, the protein was still undetectable in SDS-PAGE. Considering that the plasmids contained all the essential components necessary for transcription and translation, S might have been translated but not in necessary amounts for detection.

The sequencing of the plasmid also revealed the inclusion of the prokaryotic RBS, which made the plasmid fit for using with an *E. coli*-based system. SDS-PAGE analysis of the prokaryotic IVT reaction mix proved that S was translated as a band around 140 kDa could be observed. The identity of the band was confirmed by mass spectrometry. Peptides covering 30% of the sequence were detected and one of them was used for protein alignment against the SARS-CoV-2 and *E. coli* proteomes. The peptide was found to be unique for SARS-CoV-2, which confirmed the identity of the band as S.

# 6 Conclusions

The rapid evolution of the SARS-CoV-2 pandemic has motivated researchers to find novel, simple and safe ways to study the virus and its life cycle. In this thesis I explore the effect of lipid composition of the cellular and viral membrane in the attachment process of SARS-CoV-2. I used bottom-up synthetic biology to assemble functional synthetic miniviruses, named MiniVs. Functional assays of Alpha and Omicron MiniVs revealed that Omicron MiniVs and Omicron S have a higher affinity for the ACE2 receptor, functionalized on SLBs or GUVs. I further demonstrated an increased affinity of Omicron S towards the unfunctionalised negatively charged lipid membrane in comparison to Alpha S and quantified its $K_D$ (35.47 and 59.58 nM, respectively). This interaction could be tuned by changing the membrane charge of GUVs. Only Alpha MiniVs, but not Omicron, interacted with positively charged GUVs. To corroborate the results found in synthetic membranes, I used two cell lines with high and low ACE2 presentation. I could confirm the higher affinity of Omicron MiniVs for the receptor as well as its interaction with negatively charged lipid membranes. Given the negative charge of the membranes (both synthetic and cellular) and the positive charge of Omicron S RBD, the origin of this affinity can be explained by electrostatic interactions. Independence from ACE2 in binding to the plasma membrane might explain the shifted cellular tropism and the higher transmissibility of the Omicron lineage in comparison to previous variants. Altogether these results highlight the advantage of using bottom-up synthetic biology to study the affinity of MiniVs to synthetic and cellular lipid membranes and receptors. The findings might be translated to the natural SARS-CoV-2 virus.

Building on the discovery that Omicron S has an affinity for the plasma membrane, I set out to investigate which components of the plasma membrane are responsible for this affinity. Using GUVs, I demonstrated that tuning the membrane charge affects the affinity of Omicron and Alpha MiniVs to it. Therefore, I focused on modifying the cell membrane amounts of the polysaccharide heparan sulfate, the lipid SM and

cholesterol, which had been reported in literature to impact the viral cycle of SARS-CoV-2. I found that modification of the cholesterol levels on the cell membrane induced the biggest changes in affinity of both Alpha and Omicron MiniVs. Omicron MiniVs showed a higher affinity to the cellular membranes with elevated cholesterol. Contrarily, Alpha MiniVs showed reduced affinity to the same conditions. These differences in affinity among variants were observed in Vero E6 cells, which have high ACE2 receptor expression, but not in A549 cells, where ACE2 expression is low. Thus, the increase in affinity of Omicron MiniVs for Vero E6 cells presenting high cholesterol levels pointed towards a change in ACE2 receptor organisation. Nevertheless, that did not explain the opposite behaviour of Alpha S, which also presents a high affinity for ACE2. Affinity experiments revealed no specific interaction between cholesterol and Omicron MiniVs. It was reported in literature that increasing cholesterol in a liposomal membrane makes it more negatively charged. This more negative charge likely explains the increased binding of Omicron MiniVs and decreased binding of Alpha MiniVs, as specifically Omicron MiniVs and S showed affinity for negatively charged membranes. Using bottom-up synthetic viruses allowed for the discovery of the double-sided effect of cholesterol on the binding affinity of Omicron and Alpha MiniVs to cellular membranes, which would have been difficult to decipher utilising more complex systems.

After analysing plasma membrane components relevant to S binding affinity, I chose to investigate how the envelope lipid composition influences the binding ability of S. It is important to mention that, for this type of investigation, the full-length transmembrane S was required. For that purpose, I tested two different methods to obtain S proteoliposomes, which would have full-length S incorporated into their membrane. The first approach involved the insertion of detergent-protected S into liposomes of the desired lipid composition. I optimised the protocol to obtain these proteoliposomes and studied their size, zeta potential and ability to bind to the ACE2 receptor. The final proteoliposome populations contained either Alpha or Omicron S into their membrane, presented a size similar to that of the natural SARS-CoV-2 virus and were able to bind to an ACE2-functionalised synthetic membrane and ACE2-presenting cells. Moreover, I created proteoliposomes with different lipid composition and showed that an increased amount of cholesterol on the membrane led to a higher affinity to ACE2. This result might have an origin on the protein clustering effect attributed to cholesterol or to differences in protein insertion during the reconstitution process. Overall, the production of proteoliposomes offers a valuable approach for studying the impact of lipid species in the envelope membrane on different S variants. This effect is challenging to investigate using other non-infectious viral particles, such as VLPs or pseudoviruses, as their lipid

membrane composition cannot be so easily tuned.

Furthermore, I investigated an alternative method to produce proteoliposomes making use of the IVT technology. With that aim, I used eukaryotic and a prokaryotic-based systems to produce S in a cell-free manner. I used the HeLa lysate IVT system to express S, but no protein was detectable after performing gel electrophoresis. This was likely due to the size of the protein and the low translation efficiency of the system. Using the *E. coli*-based system I was able to yield detectable amounts of S and confirm its identity by mass spectrometry. The protein production efficiency doubles that of the HeLa lysate system, which accounts for the success of the prokaryotic system. Expressing proteins using cell-free technology has the potential to investigate the production and incorporation of membrane proteins into vesicles of the desired lipid composition, in a controlled and detergent-free environment.

Altogether, in this work I have demonstrated an affinity of Omicron S to negatively charged lipid membranes. The independence of Omicron S from ACE2 in cell binding partially contributes to the broad tropism and increased transmissibility of the SARS-CoV-2 Omicron variant. Supporting this hypothesis is the fact that the Omicron variant mainly utilises the ubiquitous endocytic pathway for cell entry, which contrasts with other variants that rely on TMPRSS2 expression on the cell surface. I have also discovered that increased levels of cholesterol in the plasma membrane lead to increased and decreased affinity of Omicron and Alpha S, respectively. This is likely due to the reported effect of cholesterol in reducing membrane charge, thereby increasing its negative charge. Furthermore I have tested different methods to produce these synthetic viruses. Cell-free technology was able to produce S, however I could only produce proteoliposomes using the standard detergent-based protocol. S proteoliposomes with high cholesterol content exhibited increased binding to the ACE2 receptor, underscoring the significant role cholesterol plays in S, both within the cellular membrane and the viral envelope. The research presented here underscores the advantage of using MiniVs to study the affinity of S variants to both synthetic and cellular membranes of specific lipid compositions. Furthermore, S proteoliposomes enable the investigation of how envelope lipid composition affects the affinity of S to ACE2. Overall, this thesis highlights the importance of synthetic biology and virology to investigate the relevance of lipid species, both in the viral and cellular membrane, in the attachment process of SARS-CoV-2. The technology presented here brings us one step closer in synthetically mimicking the complete SARS-CoV-2 viral cycle from the bottom-up.

# 7 Outlook

As the culmination of this thesis has provided valuable insights and findings on the implementation of bottom-up assembled virions for SARS-CoV-2 research, it has also opened up many possibilities for future research. In this section I will outline potential research directions, which will build upon the foundation established by this work.

## 7.1 Effect of plasma membrane components on SARS-CoV-2 attachment and entry

Many components of the plasma membrane have been postulated as co-factors for SARS-CoV-2 attachment and entry process. Among those are heparan sulfate, sphingomyelin and cholesterol.[22,65,192] Cholesterol specifically influenced the binding of Alpha and Omicron MiniVs, having opposite effects on each variant. It was reported in literature that increasing the amount of cholesterol in liposomes led to a more negative zeta potential, which would explain the higher binding of Omicron MiniVs following cholesterol treatment of cells. This hypothesis could be tested in the future by incubating Omicron and Alpha MiniVs with GUVs containing different amounts of cholesterol.

Furthermore, there are other elements for which S could have an affinity, for example those found in the vicinity of ACE2-rich plasma microdomains. One of them could be ganglioside GM1, which colocalises with ACE2 specially in cholesterol-rich clusters.[217] S has been reported to bind specifically to many species of gangliosides, because of the sialic acid residues in their structure.[218,219] Anionic phospholipids, such as phosphatidylserine (PS) or phosphatidylinositol (PI), could also serve as binding points for S, specially for the Omicron variant due to its positively charged surface. PS externalisation to the outer membrane was found to be crucial for SARS-CoV-2 entry into cells.[220]

However, many of these studies do not address how the various SARS-CoV-2 variants might respond differently to these plasma membrane components. Currently, researchers implement pseudoviruses or similar types of non-infectious viral particles to investigate the effect that the plasma membrane components have on SARS-CoV-2 attachment and entry. Nonetheless, these viral particles often present a more complex composition than MiniVs. Consequently, many of these binding co-factors could be validated for all the different SARS-CoV-2 variants in a simple and efficient assay, using MiniVs and synthetic or natural cell membranes.

## 7.2 Effect of viral envelope lipid composition on S

In this thesis I reconstituted full-length S into vesicles of different lipid composition, creating proteoliposomes. After production, I tested their ability to bind to ACE2 in a QCM-D experiment, which proved the functionality of the reconstituted S. Furthermore, I observed changes in S binding to ACE2 when incorporated into vesicles of increased cholesterol content. However, the direct effects of specific lipid species on S and its interactions with the receptor are still left to be investigated.

Another approach which might give more insight into the real influence of the lipid environment around S would be to study the insertion rate, as well as the directionality of the insertion. Specific lipid species may induce or hinder the incorporation of full-length S into the vesicles. This effect could be investigated by transmission electron microscopy, for example. Images of SARS-CoV-2 have been published, with enough resolution to count the number of S per virion.[152] Moreover, the envelope lipid composition can influence other aspects of SARS-CoV-2, such as its fusion capability.[68] This effect could also be investigated by using GUVs or cells.

## 7.3 Cell-free S production and incorporation into membranes

After translation of S with the *E. coli*-based IVT kit, the next step would be to investigate the functionality of the produced protein. Due to the high amount of proteins found in the IVT reaction mix, ideally the protein would be first isolated. All the protein components of the PURExpress system are his-tagged (with the exception of the ribosome), as well as the produced S. For that purpose, a new plasmid coding for a non-tagged S will need to be designed. After purification of the new untagged S, next steps would focus on studying the ability of the protein to bind to ACE2 in synthetic and natural membranes.

Moreover, expression should be made in the presence of lipid membranes, to avoid protein misfolding and aggregation. Thus, protein incorporation and directionality should also be investigated.

Despite the success of the PURExpress kit in translating S, there are still many parameters that need optimisation which could be tackled by using other IVT systems. There are many CFPS kits available, and each of them has specific advantages and disadvantages. The use of a HeLa lysate was not adequate because of the expected yield, specially for such a big protein like S with 136 kDa each monomer. However, utilising *E. coli*-based methods, despite their higher yield, might not be the right solution either. Differences between prokaryotic and eukaryotic systems can lead to big changes in the final translated protein. One of such changes is protein glycosylation patterns, which can be very distinct among species.[221] Glycosylation of S is specially relevant due to its role during S incorporation into the virion and antibody neutralisation.[222] Therefore, next experiments should be performed with more powerful eukaryotic CFPS systems. One example is a coupled transcription/translation system from an eukaryotic lysate obtained from rabbit reticulocytes.[96]

Furthermore full-length S, being a transmembrane protein, should be translated in the presence of lipid membranes, such as liposomes, microsomes or others. Next attempts to produce the protein will include lipid vesicles. Using a system devoid of lipid compartments implies that the supplied lipid membranes will have a controlled composition. This can also serve as a system to study the effect of specific lipid species in the incorporation rate and behaviour of S. Incorporation of full-length S into a lipid vesicle, in comparison to functionalisation of liposomes with his-tagged S, is essential to study further aspects of the viral cycle other than attachment, such as fusion. The transmembrane domain of S contributes to the stabilisation of its trimeric structure and serves as an anchor between the viral and the cellular membranes, facilitating successful fusion.[223,224]

## 7.4 MiniVs of other viral species: dengue and HIV

The synthetic minimal virus technology could be applied to other enveloped viruses as well. One example is HIV. The virus is decorated with the envelope (Env) glycoprotein trimer, which has a similar role to S serving as the main surface protein that interacts with the cells to initiate viral entry. Both proteins have a trimeric form and are classified as class I fusion proteins, as they undergo a conformational change preceding membrane fusion.[225] Because of these reasons, HIV would be a good candidate virus to mimic

using MiniV and other bottom-up synthetic technologies.

In fact, HIV has already been studied with this kind of system. Ingale *et al* produced liposomes and decorated them with Env, which showed to be superior than soluble Env in activating B cells.[119] Similarly to SARS-CoV-2, HIV MiniVs could be used to study the importance of the lipid composition. HIV MiniVs could be employed to investigate the role of plasma membrane elements in viral attachment and entry. Additionally, HIV proteoliposomes could offer insights into the essential lipid species of the viral envelope. It has been reported that cholesterol and SL serve an important role in the virion as their removal reduces HIV infectivity.[70,71] Other lipidic components of the envelope that could be further investigated are PS and PE.[226]

Another virus that would be interesting to assemble synthetically is dengue (DENV). The surface of the virus is covered by the envelope (E) protein, which is found as a dimer and is important in the first attachment to the host cell. The outer protein shell composed of E proteins organises into an icosahedral scaffold.[122] Infection by one of its main four serotypes confers immunity to only that specific strain, as residue identity when comparing all four E proteins goes as low as 63%.[227] Consequently, reinfection by another serotype often leads to antibody-dependent enhancement, which aids in the advancement of the DENV infection.[228]

The lipid and protein compositions of the DENV are known, which make it a good candidate for synthetic minimal virus production. Similar approaches have been reported. Zheng *et al* produced gold nanoparticles covered in virus lysate, which served to detect positive patients from plasma samples with higher sensitivity.[229] However, by using this methodology all viral proteins are exposed on the surface of the nanoparticle and with no specific directionality. The use of MiniV technology to mimic DENV would be a simple and scalable approach to perform antibody neutralisation assays, which are needed for several purposes, e.g. identifying the serotype of a DENV infection. Even though synthetic minimal DENV are easier to produce than, for example, VLPs, the high organisation of the E protein might be difficult to mimic synthetically. His-tagged proteins might not assemble in the same strict organisation as in the mature DENV virus.

## 7.5 Synthetic SARS-CoV-2 viral cycle

In this thesis I have focused on investigating the cellular attachment process of the SARS-CoV-2 virus using bottom-up synthetic biology. The ultimate goal of this project would

be to replicate the complete viral cycle of SARS-CoV-2 synthetically.[4] The missing steps to reproduce would be: entry, release of genetic material, replication of genome and translation of proteins, assembly of virions and exocytosis from the cell (Figure 1.1).[6] The entry is only considered in those cases in which the virus fuses with the endosomal compartment membrane after endocytosis, instead of fusing directly at the cellular membrane. For the release of the genetic material fusion with the endosome or the plasma membrane needs to take place. To achieve viral and cell membrane fusion full-length S can be used, which will undergo a conformational change after cleavage at the plasma membrane surface or at the endosomal compartment.[15,51] However, other approaches could be used to achieve fusion, from lipid species that fuse with endosomal membranes upon acidification, to recombinant proteins or DNA.[230–232]

The SARS-CoV-2 genome could be synthesised by using recombinant DNA technology.[233] However, the size of the natural virus genome (around 30 kb) will pose encapsulation challenges into viral-sized particles.[18] Certain aspects of the process can be tuned to increase encapsulation yield, such as the liposome formation method and initial lipid and genetic material concentration.[234] Furthermore, the genetic material could contain the whole viral genome or maintain only specific elements required for viral replication.

Viral assembly and exit of the cell could be achieved by exploiting the intrinsic cellular machinery. However, following this approach compromises the control over the created synthetic viral system. Therefore, making use of the aforementioned cell-free systems, genome replication and translation of proteins could be achieved without the need of using living cells, while modifying the system for specific needs.[130,235] Using a cell-free system substitutes the exocytosis for a purification step of viral particles. This could be achieved by density gradient centrifugation or column affinity purification in the case of the PUREsystem, as most of its components are his-tagged.[97,236]

# 7 Acknowledgements

I would like to express my deepest gratitude to my advisor, Prof. Dr. Joachim P. Spatz, for the opportunity of doing my PhD in the group, for the support, guidance and encouragement throughout my research. I am profoundly thankful to my supervisor, Dr. Ilia Platzman, for the invaluable insights, feedback, discussions, and constant support during this journey.

I am grateful to my TAC committee members, Dr. Alessia Ruggieri and Prof. Dr. Hans-Georg Kräusslich for their valuable feedback and suggestions. I would like to thank Prof. Dr. Oliver Fackler for showing interest in my project and agreeing to be part of my dissertation committee.

I want to extend my gratitude towards Dr. Sebastian Fabritz and Mrs. Tatjana Rudi for performing the mass spectrometry experiments, as well as Dr. Martin Schröter for his help analysing the results. I want to thank the wonderful students I had the pleasure to supervise: Thien, Elena and Deus.

I want to thank my lab friends (not only colleagues anymore!), Ann-Kathrin, Yannik, Mai, Michelle, Julia, Meline, Anastassiya and Niklas for always being there for coffee breaks, bouldering, swimming, flohmarkts, GNTM nights and even occasionally partying. Specially Ann-Kathrin, I hope we can continue being friends and travelling for many years to come. I would also like to thank everyone who took the time to help review and correct my thesis.

A mis amigos de la universidad, Suky, Rebe, Eva, Víctor, Xavi, Alba y María, por los años de amistad desde que empezamos la universidad hasta hoy. A les meves amigues des dels 3 anys, Laura, Eli i Judit, per sempre ser-hi, en persona o a distància.

Por supuesto quiero agradecer a mis padres, Silvia y Roger, y a mi hermano, Jaime, su apoyo durante todos estos años desde que empecé la carrera. Desde pequeña me han animado a seguir el camino que yo quisiera y han estado a mi lado siempre que lo he necesitado. Os quiero mucho.

Last but, of course, not least, I want to thank my favourite person and my best cheerleader, Andy. You have been a great support during these last 3.5 years (and ever since we met more than six years ago), always there to motivate me when I needed it. And, of course, to discuss and argue science which made mine better.

# 7 Bibliography


1. The species Severe acute respiratory syndrome-related coronavirus: classifying 2019-nCoV and naming it SARS-CoV-2. *Nature Microbiology* **5,** 536–544 (2020).
2. Li, G., Hilgenfeld, R., Whitley, R. & De Clercq, E. Therapeutic strategies for COVID-19: progress and lessons learned. *Nature Reviews Drug Discovery* **22,** 449–475 (2023).
3. Kaufer, A. M., Theis, T., Lau, K. A., Gray, J. L. & Rawlinson, W. D. Laboratory biosafety measures involving SARS-CoV-2 and the classification as a Risk Group 3 biological agent. *Pathology* **52,** 790–795 (2020).
4. Staufer, O. *et al.* Bottom-up assembly of viral replication cycles. *Nature Communications* **13,** 6530 (2022).
5. Walls, A. C. *et al.* Structure, Function, and Antigenicity of the SARS-CoV-2 Spike Glycoprotein. *Cell* **181,** 281–292.e6 (2020).
6. Carter, J. & Saunders, V. A. *Virology: principles and applications* (John Wiley & Sons, 2007).
7. Garoff, H., Hewson, R. & Opstelten, D.-J. E. Virus maturation by budding. *Microbiology and molecular biology reviews* **62,** 1171–1190 (1998).
8. Mebatsion, T., Weiland, F. & Conzelmann, K.-K. Matrix protein of rabies virus is responsible for the assembly and budding of bullet-shaped particles and interacts with the transmembrane spike glycoprotein G. *Journal of virology* **73,** 242–250 (1999).
9. Rohrmann, G. F. Baculovirus molecular biology (2019).
10. Geisbert, T. & Jahrling, P. Differentiation of filoviruses by electron microscopy. *Virus research* **39,** 129–150 (1995).
11. Booy, F., Ruigrok, R. & Van Bruggen, E. Electron microscopy of influenza virus: a comparison of negatively stained and ice-embedded particles. *Journal of molecular biology* **184,** 667–676 (1985).

12. Wildy, P, Russell, W. & Horne, R. The morphology of herpes virus. *Virology* **12,** 204–222 (1960).
13. Oshiro, L., Schieble, J. & Lennette, E. Electron microscopic studies of coronavirus. *Journal of General Virology* **12,** 161–168 (1971).
14. Dimmock, N. J., Easton, A. J. & Leppard, K. N. *Introduction to modern virology* (John Wiley & Sons, 2015).
15. Jackson, C., Farzan, M., Chen, B. & Choe, H. Mechanisms of SARS-COV-2 entry into cells. *Nature Reviews Molecular Cell Biology* **23,** 3–20 (2021).
16. For Disease Prevention, E. C. & Control. *SARS-COV-2 variants of concern as of 15 March 2024* 2024.
17. Klein, S. *et al.* SARS-CoV-2 structure and replication characterized by in situ cryo-electron tomography. eng. *Nature communications* **11,** 5885–10. ISSN: 2041-1723 (2020).
18. Khailany, R. A., Safdar, M. & Ozaslan, M. Genomic characterization of a novel SARS-CoV-2. *Gene reports* **19,** 100682 (2020).
19. Yan, W., Zheng, Y., Zeng, X., He, B. & Cheng, W. Structural biology of SARS-COV-2: Open the door for novel therapies. *Signal Transduction and Targeted Therapy* **7** (2022).
20. Wang, K. *et al.* CD147-spike protein is a novel route for SARS-COV-2 infection to host cells. *Signal Transduction and Targeted Therapy* **5** (2020).
21. Wang, S. *et al.* AXL is a candidate receptor for SARS-CoV-2 that promotes infection of pulmonary and bronchial epithelial cells. *Cell research* **31,** 126–140 (2021).
22. Clausen, T. M. *et al.* SARS-CoV-2 Infection Depends on Cellular Heparan Sulfate and ACE2. *Cell* **183,** 1043–1057.e15 (2020).
23. Hoffmann, M. *et al.* SARS-CoV-2 Cell Entry Depends on ACE2 and TMPRSS2 and Is Blocked by a Clinically Proven Protease Inhibitor. *Cell* **181,** 271–280.e8 (2020).
24. Meng, B. *et al.* Altered TMPRSS2 usage by SARS-CoV-2 Omicron impacts infectivity and fusogenicity. *Nature* **603,** 706–714 (2022).
25. V'kovski, P., Kratzel, A., Steiner, S., Stalder, H. & Thiel, V. Coronavirus Biology and replication: Implications for SARS-COV-2. *Nature Reviews Microbiology* **19,** 155–170 (2020).
26. Wu, F. *et al.* A new coronavirus associated with human respiratory disease in China. *Nature* **579,** 265–269 (2020).
27. Rothe, C. *et al.* Transmission of 2019-nCoV infection from an asymptomatic contact in Germany. *New England journal of medicine* **382,** 970–971 (2020).

28. Volz, E. *et al.* Evaluating the effects of SARS-CoV-2 spike mutation D614G on transmissibility and pathogenicity. *Cell* **184,** 64–75 (2021).
29. Organization, W. H. *et al.* Historical working definitions and primary actions for SARS-CoV-2 variants. *World Health Organization: Geneva, Switzerland* (2023).
30. Haycroft, E. R. *et al.* Antibody Fc-binding profiles and ACE2 affinity to SARS-CoV-2 RBD variants. *Medical Microbiology and Immunology* **212,** 291–305 (2023).
31. Kim, S. *et al.* Binding of human ACE2 and RBD of omicron enhanced by unique interaction patterns among SARS-CoV-2 variants of concern. *Journal of computational chemistry* **44,** 594–601 (2023).
32. Davies, N. G. *et al.* Increased mortality in community-tested cases of SARS-CoV-2 lineage B. 1.1. 7. *Nature* **593,** 270–274 (2021).
33. Tian, F. *et al.* N501Y mutation of spike protein in SARS-CoV-2 strengthens its binding to receptor ACE2. *elife* **10,** e69091 (2021).
34. Meng, B. *et al.* Recurrent emergence of SARS-CoV-2 spike deletion H69/V70 and its role in the Alpha variant B. 1.1. 7. *Cell reports* **35** (2021).
35. Thomson, E. C. *et al.* Circulating SARS-CoV-2 spike N439K variants maintain fitness while evading antibody-mediated immunity. *Cell* **184,** 1171–1187 (2021).
36. Motozono, C. *et al.* SARS-CoV-2 spike L452R variant evades cellular immunity and increases infectivity. *Cell host & microbe* **29,** 1124–1136 (2021).
37. Wang, P. *et al.* Antibody resistance of SARS-CoV-2 variants B. 1.351 and B. 1.1. 7. *Nature* **593,** 130–135 (2021).
38. Ou, J. *et al.* Tracking SARS-CoV-2 Omicron diverse spike gene mutations identifies multiple inter-variant recombination events. *Signal Transduction and Targeted Therapy* **7,** 138 (2022).
39. Li, L. *et al.* Structural basis of human ACE2 higher binding affinity to currently circulating Omicron SARS-CoV-2 sub-variants BA. 2 and BA. 1.1. *Cell* **185,** 2952–2960 (2022).
40. Shi, G. *et al.* Omicron Spike confers enhanced infectivity and interferon resistance to SARS-CoV-2 in human nasal tissue. *Nature Communications* **15,** 889 (2024).
41. Suzuki, R. *et al.* Attenuated fusogenicity and pathogenicity of SARS-CoV-2 Omicron variant. *Nature* **603,** 700–705 (2022).
42. Wolter, N. *et al.* Early assessment of the clinical severity of the SARS-CoV-2 omicron variant in South Africa: a data linkage study. *The Lancet* **399,** 437–446 (2022).

43. Bálint, G., Vörös-Horváth, B. & Széchenyi, A. Omicron: increased transmissibility and decreased pathogenicity. *Signal Transduction and Targeted Therapy* **7,** 151 (2022).
44. Suzuki, R. *et al.* Attenuated fusogenicity and pathogenicity of SARS-CoV-2 Omicron variant. *Nature* **603,** 700–705 (2022).
45. Johnson, B. A. *et al.* Loss of furin cleavage site attenuates SARS-CoV-2 pathogenesis. *Nature* **591,** 293–299 (2021).
46. Braga, L. *et al.* Drugs that inhibit TMEM16 proteins block SARS-CoV-2 spike-induced syncytia. *Nature* **594,** 88–93 (2021).
47. Buchrieser, J. *et al.* Syncytia formation by SARS-CoV-2-infected cells. *The EMBO journal* **40,** e107405 (2021).
48. Hui, K. P. *et al.* SARS-CoV-2 Omicron variant replication in human bronchus and lung ex vivo. *Nature* **603,** 715–720 (2022).
49. Planas, D. *et al.* Considerable escape of SARS-CoV-2 Omicron to antibody neutralization. *Nature* **602,** 671–675 (2022).
50. Basso, L. G. M., Zeraik, A. E., Felizatti, A. P. & Costa-Filho, A. J. Membranotropic and biological activities of the membrane fusion peptides from SARS-CoV spike glycoprotein: The importance of the complete internal fusion peptide domain. *Biochimica et Biophysica Acta (BBA)-Biomembranes* **1863,** 183697 (2021).
51. Lavie, M., Dubuisson, J. & Belouzard, S. SARS-CoV-2 spike furin cleavage site and S2 basic residues modulate the entry process in a host cell-dependent manner. *Journal of Virology* **96,** e00474–22 (2022).
52. Zhang, L. *et al.* SARS-CoV-2 spike-protein D614G mutation increases virion spike density and infectivity. *Nature communications* **11,** 6013 (2020).
53. Papa, G. *et al.* Furin cleavage of SARS-CoV-2 Spike promotes but is not essential for infection and cell-cell fusion. *PLoS pathogens* **17,** e1009246 (2021).
54. Rajah, M. M., Bernier, A., Buchrieser, J. & Schwartz, O. The mechanism and consequences of SARS-CoV-2 spike-mediated fusion and syncytia formation. *Journal of molecular biology* **434,** 167280 (2022).
55. Belouzard, S., Chu, V. C. & Whittaker, G. R. Activation of the SARS coronavirus spike protein via sequential proteolytic cleavage at two distinct sites. *Proceedings of the National Academy of Sciences* **106,** 5871–5876 (2009).
56. Winstone, H. *et al.* The polybasic cleavage site in SARS-CoV-2 spike modulates viral sensitivity to type I interferon and IFITM2. *Journal of virology* **95,** 10–1128 (2021).

57. Raffy, S. & Teissié, J. Control of lipid membrane stability by cholesterol content. *Biophysical journal* **76,** 2072–2080 (1999).
58. Simons, K., Ehehalt, R., *et al.* Cholesterol, lipid rafts, and disease. *The Journal of clinical investigation* **110,** 597–603 (2002).
59. Li, G.-M., Li, Y.-G., Yamate, M., Li, S.-M. & Ikuta, K. Lipid rafts play an important role in the early stage of severe acute respiratory syndrome-coronavirus life cycle. *Microbes and infection* **9,** 96–102 (2007).
60. Liao, Z., Cimakasky, L. M., Hampton, R., Nguyen, D. H. & Hildreth, J. E. Lipid rafts and HIV pathogenesis: host membrane cholesterol is required for infection by HIV type 1. *Journal of Virology* **97** (2004).
61. Glende, J. *et al.* Importance of cholesterol-rich membrane microdomains in the interaction of the S protein of SARS-coronavirus with the cellular receptor angiotensin-converting enzyme 2. *Virology* **381,** 215–221 (2008).
62. Niort, K. *et al.* Cholesterol and Ceramide Facilitate Membrane Fusion Mediated by the Fusion Peptide of the SARS-CoV-2 Spike Protein. *ACS omega* **8,** 32729–32739 (2023).
63. Grassmé, H., Riehle, A., Wilker, B. & Gulbins, E. Rhinoviruses infect human epithelial cells via ceramide-enriched membrane platforms. *Journal of Biological Chemistry* **280,** 26256–26262 (2005).
64. Yoo, S.-W. *et al.* Inhibition of neutral sphingomyelinase 2 impairs HIV-1 envelope formation and substantially delays or eliminates viral rebound. *Proceedings of the National Academy of Sciences* **120,** e2219543120 (2023).
65. Carpinteiro, A. *et al.* Pharmacological inhibition of acid sphingomyelinase prevents uptake of SARS-CoV-2 by epithelial cells. *Cell Reports Medicine* **1** (2020).
66. Ivanova, P. T. *et al.* Lipid Composition of the Viral Envelope of Three Strains of Influenza Virus: Not All Viruses Are Created Equal. *ACS infectious diseases* **1,** 435–442 (2015).
67. Lorizate, M. *et al.* Comparative lipidomics analysis of HIV-1 particles and their producer cell membrane in different cell lines. *Cellular microbiology* **15,** 292–304 (2013).
68. Mesquita, F. S. *et al.* S-acylation controls SARS-CoV-2 membrane lipid organization and enhances infectivity. *Developmental cell* **56,** 2790–2807 (2021).
69. Ono, A. & Freed, E. O. Plasma membrane rafts play a critical role in HIV-1 assembly and release. *Proceedings of the National Academy of Sciences* **98,** 13925–13930 (2001).
70. Graham, D. R., Chertova, E., Hilburn, J. M., Arthur, L. O. & Hildreth, J. E. Cholesterol depletion of human immunodeficiency virus type 1 and simian im-

munodeficiency virus with $\beta$-cyclodextrin inactivates and permeabilizes the virions: evidence for virion-associated lipid rafts. *Journal of virology* **77,** 8237–8248 (2003).

71. Brügger, B. *et al.* The HIV lipidome: a raft with an unusual composition. *Proceedings of the National Academy of Sciences* **103,** 2641–2646 (2006).
72. Barman, S. & Nayak, D. P. Lipid raft disruption by cholesterol depletion enhances influenza A virus budding from MDCK cells. *Journal of virology* **81,** 12169–12178 (2007).
73. Sun, X. & Whittaker, G. R. Role for influenza virus envelope cholesterol in virus entry and infection. *Journal of virology* **77,** 12543–12551 (2003).
74. Saud, Z. *et al.* The SARS-CoV2 envelope differs from host cells, exposes procoagulant lipids, and is disrupted in vivo by oral rinses. *Journal of Lipid Research* **63** (2022).
75. Göpfrich, K., Platzman, I. & Spatz, J. P. Mastering complexity: towards bottom-up construction of multifunctional eukaryotic synthetic cells. *Trends in biotechnology* **36,** 938–951 (2018).
76. Hirschi, S., Ward, T. R., Meier, W. P., Müller, D. J. & Fotiadis, D. Synthetic biology: bottom-up assembly of molecular systems. *Chemical reviews* **122,** 16294–16328 (2022).
77. Hutchison III, C. A. *et al.* Design and synthesis of a minimal bacterial genome. *Science* **351,** aad6253 (2016).
78. Yuan, S., Shi, J., Jiang, J. & Ma, Y. Genome-scale top-down strategy to generate viable genome-reduced phages. *Nucleic Acids Research* **50,** 13183–13197 (2022).
79. Ro, D.-K. *et al.* Production of the antimalarial drug precursor artemisinic acid in engineered yeast. *Nature* **440,** 940–943 (2006).
80. Peralta-Yahya, P. P., Zhang, F., Del Cardayre, S. B. & Keasling, J. D. Microbial engineering for the production of advanced biofuels. *Nature* **488,** 320–328 (2012).
81. Donald, R. G. *et al.* A novel approach to generate a recombinant toxoid vaccine against Clostridium difficile. *Microbiology* **159,** 1254–1266 (2013).
82. Mitra, A. *et al.* From bench to bedside: the history and progress of CAR T cell therapy. *Frontiers in Immunology* **14,** 1188049 (2023).
83. Bedau, M. A., Parke, E. C., Tangen, U. & Hantsche-Tangen, B. Social and ethical checkpoints for bottom-up synthetic biology, or protocells. *Systems and synthetic biology* **3,** 65–75 (2009).
84. Fink, A. *et al.* Extracellular Cues Govern Shape and Cytoskeletal Organization in Giant Unilamellar Lipid Vesicles. *ACS Synthetic Biology* **12,** 369–374 (2023).

85. Gavriljuk, K. *et al.* A self-organized synthetic morphogenic liposome responds with shape changes to local light cues. *Nature Communications* **12,** 1548 (2021).
86. Litschel, T. *et al.* Reconstitution of contractile actomyosin rings in vesicles. *Nature communications* **12,** 2254 (2021).
87. Litschel, T., Ramm, B., Maas, R., Heymann, M. & Schwille, P. Beating vesicles: encapsulated protein oscillations cause dynamic membrane deformations. *Angewandte Chemie International Edition* **57,** 16286–16290 (2018).
88. Osawa, M. & Erickson, H. P. Liposome division by a simple bacterial division machinery. *Proceedings of the National Academy of Sciences* **110,** 11000–11004 (2013).
89. Jahnke, K., Huth, V., Mersdorf, U., Liu, N. & Göpfrich, K. Bottom-up assembly of synthetic cells with a DNA cytoskeleton. *ACS nano* **16,** 7233–7241 (2022).
90. Jahnke, K. *et al.* Proton gradients from light-harvesting E. coli control DNA assemblies for synthetic cells. *Nature communications* **12,** 3967 (2021).
91. Matsuura, K., Hirahara, M., Sakamoto, K. & Inaba, H. Alkyl anchor–modified artificial viral capsid budding outside-to-inside and inside-to-outside giant vesicles. *Science and Technology of Advanced Materials* **25,** 2347191 (2024).
92. Stephan, M. S. *et al.* Biomimetic asymmetric bacterial membranes incorporating lipopolysaccharides. *Biophysical journal* **122,** 2147–2161 (2023).
93. Beygmoradi, A., Homaei, A., Hemmati, R. & Fernandes, P. Recombinant protein expression: challenges in production and folding related matters. *International Journal of Biological Macromolecules* **233,** 123407 (2023).
94. Sosa-Carrillo, S., Galez, H., Napolitano, S., Bertaux, F. & Batt, G. Maximizing protein production by keeping cells at optimal secretory stress levels using real-time control approaches. *Nature Communications* **14,** 3028 (2023).
95. Lu, Y. Cell-free synthetic biology: Engineering in an open world. *Synthetic and systems biotechnology* **2,** 23–27 (2017).
96. Gregorio, N. E., Levine, M. Z. & Oza, J. P. A user's guide to cell-free protein synthesis. *Methods and protocols* **2,** 24 (2019).
97. Shimizu, Y. *et al.* Cell-free translation reconstituted with purified components. *Nature biotechnology* **19,** 751–755 (2001).
98. Gao, W., Cho, E., Liu, Y. & Lu, Y. Advances and challenges in cell-free incorporation of unnatural amino acids into proteins. *Frontiers in pharmacology* **10,** 611 (2019).
99. Blanken, D., Foschepoth, D., Serrão, A. C. & Danelon, C. Genetically controlled membrane synthesis in liposomes. *Nature communications* **11,** 4317 (2020).

100. Meier, S., Güthe, S., Kiefhaber, T. & Grzesiek, S. Foldon, the natural trimerization domain of T4 fibritin, dissociates into a monomeric A-state form containing a stable $\beta$-hairpin: atomic details of trimer dissociation and local $\beta$-hairpin stability from residual dipolar couplings. *Journal of molecular biology* **344,** 1051–1069 (2004).
101. Amanat, F. *et al.* A serological assay to detect SARS-CoV-2 seroconversion in humans. *Nature medicine* **26,** 1033–1036 (2020).
102. DeFrancesco, L. Synthetic virology: the experts speak. *Nature Biotechnology* **39,** 1185–1193 (2021).
103. Wang, Y. *et al.* Teicoplanin inhibits Ebola pseudovirus infection in cell culture. *Antiviral research* **125,** 1–7 (2016).
104. Somiya, M., Liu, Q. & Kuroda, S. Current progress of virus-mimicking nanocarriers for drug delivery. *Nanotheranostics* **1,** 415 (2017).
105. Wholey, W.-Y. *et al.* Synthetic liposomal mimics of biological viruses for the study of immune responses to infection and vaccination. *Bioconjugate chemistry* **31,** 685–697 (2020).
106. Huang, W.-C., Chiem, K., Martinez-Sobrido, L. & Lovell, J. F. Intranasal immunization with liposome-displayed receptor-binding domain induces mucosal immunity and protection against SARS-CoV-2. *Pathogens* **11,** 1035 (2022).
107. Nooraei, S. *et al.* Virus-like particles: preparation, immunogenicity and their roles as nanovaccines and drug nanocarriers. *Journal of nanobiotechnology* **19,** 1–27 (2021).
108. Santi, L., Huang, Z. & Mason, H. Virus-like particles production in green plants. *Methods* **40,** 66–76 (2006).
109. Huang, X., Wang, X., Zhang, J., Xia, N. & Zhao, Q. Escherichia coli-derived virus-like particles in vaccine development. *npj Vaccines* **2,** 3 (2017).
110. Bundy, B. C., Franciszkowicz, M. J. & Swartz, J. R. Escherichia coli-based cell-free synthesis of virus-like particles. *Biotechnology and bioengineering* **100,** 28–37 (2008).
111. Xiang, Q., Li, L., Wu, J., Tian, M. & Fu, Y. Application of pseudovirus system in the development of vaccine, antiviral-drugs, and neutralizing antibodies. *Microbiological Research* **258,** 126993 (2022).
112. Crawford, K. H. *et al.* Protocol and reagents for pseudotyping lentiviral particles with SARS-CoV-2 spike protein for neutralization assays. *Viruses* **12,** 513 (2020).
113. Nie, J. *et al.* Nipah pseudovirus system enables evaluation of vaccines in vitro and in vivo using non-BSL-4 facilities. *Emerging microbes & infections* **8,** 272–281 (2019).

114. Moeschler, S., Locher, S., Conzelmann, K.-K., Krämer, B. & Zimmer, G. Quantification of lyssavirus-neutralizing antibodies using vesicular stomatitis virus pseudotype particles. *Viruses* **8,** 254 (2016).
115. Verta, R. *et al.* Generation of spike-extracellular vesicles (S-EVs) as a tool to mimic SARS-CoV-2 interaction with host cells. *Cells* **11,** 146 (2022).
116. Ando, H., Lemire, S., Pires, D. P. & Lu, T. K. Engineering modular viral scaffolds for targeted bacterial population editing. *Cell systems* **1,** 187–196 (2015).
117. Lenneman, B. R., Fernbach, J., Loessner, M. J., Lu, T. K. & Kilcher, S. Enhancing phage therapy through synthetic biology and genome engineering. *Current Opinion in Biotechnology* **68,** 151–159 (2021).
118. Staufer, O. *et al.* Synthetic virions reveal fatty acid-coupled adaptive immunogenicity of SARS-CoV-2 spike glycoprotein. *Nature Communications* **13,** 868 (2022).
119. Ingale, J. *et al.* High-density array of well-ordered HIV-1 spikes on synthetic liposomal nanoparticles efficiently activate B cells. *Cell reports* **15,** 1986–1999 (2016).
120. Sia, Z. R. *et al.* A liposome-displayed hemagglutinin vaccine platform protects mice and ferrets from heterologous influenza virus challenge. *Proceedings of the National Academy of Sciences* **118,** e2025759118 (2021).
121. Polack, F. P. *et al.* Safety and efficacy of the BNT162b2 mRNA Covid-19 vaccine. *New England journal of medicine* **383,** 2603–2615 (2020).
122. Kuhn, R. J. *et al.* Structure of dengue virus: implications for flavivirus organization, maturation, and fusion. *Cell* **108,** 717–725 (2002).
123. Hu, V. T. *et al.* Cell-free expression of Nipah virus transmembrane proteins for proteoliposome vaccine design. *bioRxiv,* 2024–07 (2024).
124. McColman, S. *et al.* SARS-CoV-2 virus-like-particles via liposomal reconstitution of spike glycoproteins. *Nanoscale Advances* **5,** 4167–4181 (2023).
125. Chen, K., Jiang, M., Liu, J., Huang, D. & Yang, Y. R. DNA nanostructures as biomolecular scaffolds for antigen display. *Wiley Interdisciplinary Reviews: Nanomedicine and Nanobiotechnology* **16,** e1921 (2024).
126. Wamhoff, E.-C. *et al.* Enhancing antibody responses by multivalent antigen display on thymus-independent DNA origami scaffolds. *Nature communications* **15,** 795 (2024).
127. Chaudhary, A. & Yadav, R. D. A review on virus protein self-assembly. *Journal of Nanoparticle Research* **21,** 1–13 (2019).
128. Brooks, R., Morici, L. & Sandoval, N. Cell Free Bacteriophage Synthesis from Engineered Strains Improves Yield. *ACS Synthetic Biology* **12,** 2418–2431 (2023).

129. Levrier, A. *et al.* PHEIGES: all-cell-free phage synthesis and selection from engineered genomes. *Nature communications* **15,** 2223 (2024).
130. Shin, J., Jardine, P. & Noireaux, V. Genome replication, synthesis, and assembly of the bacteriophage T7 in a single cell-free reaction. *ACS synthetic biology* **1,** 408–413 (2012).
131. Aoki, K. *et al.* Synthesis of the full-length hepatitis B virus core protein and its capsid formation. *Organic & Biomolecular Chemistry* (2024).
132. Spice, A. J., Aw, R., Bracewell, D. G. & Polizzi, K. M. Synthesis and assembly of hepatitis B virus-like particles in a Pichia pastoris cell-free system. *Frontiers in Bioengineering and Biotechnology* **8,** 72 (2020).
133. Wang, Z. & Zhang, X. Adenovirus vector-attributed hepatotoxicity blocks clinical application in gene therapy. *Cytotherapy* **23,** 1045–1052 (2021).
134. Singh, R., Al-Jamal, K. T., Lacerda, L. & Kostarelos, K. Nanoengineering artificial lipid envelopes around adenovirus by self-assembly. *Acs Nano* **2,** 1040–1050 (2008).
135. Colom, J. *et al.* Liposome-encapsulated bacteriophages for enhanced oral phage therapy against Salmonella spp. *Applied and environmental microbiology* **81,** 4841–4849 (2015).
136. Rigaud, J.-L. & Lévy, D. in *Liposomes, Part B* 65–86 (Academic Press, 2003).
137. Lussier, F. *et al.* pH-Triggered Assembly of Endomembrane Multicompartments in Synthetic Cells. *ACS Synthetic Biology* **11,** 366–382 (2022).
138. Schindelin, J. *et al.* Fiji: an open-source platform for biological-image analysis. *Nat Meth* **9,** 676–682. ISSN: 15487091 (July 2012).
139. Van Rossum, G. & Drake, F. L. *Python 3 Reference Manual* (CreateSpace Independent Publishing Platform, Scotts Valley, CA, 2009).
140. Waskom, M. L. Seaborn: statistical data visualization. *Journal of Open Source Software* **6,** 3021 (2021).
141. McKinney, W. *et al. Data structures for statistical computing in Python.* in *SciPy* **445** (2010), 51–56.
142. Hunter, J. D. Matplotlib: A 2D graphics environment. *Computing in science & engineering* **9,** 90–95 (2007).
143. Harris, C. R. *et al.* Array programming with NumPy. *Nature* **585,** 357–362 (Sept. 2020).
144. Kluyver, T. *et al.* Jupyter Notebooks-a publishing format for reproducible computational workflows. *Elpub* **2016,** 87–90 (2016).

145. Mouchahoir, T. & Schiel, J. E. Development of an LC-MS/MS peptide mapping protocol for the NISTmAb. *Analytical and bioanalytical chemistry* **410,** 2111–2126 (2018).
146. Traian, M. M. D., Flecha, F. L. G. & Levi, V. Imaging lipid lateral organization in membranes with C-laurdan in a confocal microscope. *Journal of lipid research* **53,** 609–616 (2012).
147. Ganzinger, K. A. *et al.* FtsZ Reorganization Facilitates Deformation of Giant Vesicles in Microfluidic Traps. *Angewandte Chemie International Edition* **59,** 21372–21376 (2020).
148. Moga, A., Yandrapalli, N., Dimova, R. & Robinson, T. Optimization of the Inverted Emulsion Method for High-Yield Production of Biomimetic Giant Unilamellar Vesicles. *ChemBioChem* **20,** 2674–2682 (2019).
149. Briand, E., Zäch, M., Svedhem, S., Kasemo, B. & Petronis, S. Combined QCM-D and EIS study of supported lipid bilayer formation and interaction with pore-forming peptides. *Analyst* **135,** 343–350 (2 2010).
150. Parasassi, T., De Stasio, G, d'Ubaldo, A. & Gratton, E. Phase fluctuation in phospholipid membranes revealed by Laurdan fluorescence. *Biophysical journal* **57,** 1179–1186 (1990).
151. Zhu, N. *et al.* A novel coronavirus from patients with pneumonia in China, 2019. *New England journal of medicine* **382,** 727–733 (2020).
152. Klein, S. *et al.* SARS-CoV-2 structure and replication characterized by in situ cryo-electron tomography. *Nature communications* **11,** 5885 (2020).
153. Ghatak, S. *et al.* Electroceutical fabric lowers zeta potential and eradicates coronavirus infectivity upon contact. *Scientific reports* **11,** 21723 (2021).
154. Jurrus, E. *et al.* Improvements to the APBS biomolecular solvation software suite. *Protein Science* **27,** 112–128 (2018).
155. Nie, C. *et al.* Charge matters: Mutations in omicron variant favor binding to cells. *Chembiochem* **23,** e202100681 (2022).
156. Rodahl, M., Höök, F., Krozer, A., Brzezinski, P. & Kasemo, B. Quartz crystal microbalance setup for frequency and Q-factor measurements in gaseous and liquid environments. *Review of Scientific Instruments* **66,** 3924–3930 (1995).
157. Dixon, M. C. Quartz crystal microbalance with dissipation monitoring: enabling real-time characterization of biological materials and their interactions. *Journal of biomolecular techniques: JBT* **19,** 151 (2008).
158. Yagüe Relimpio, A. *et al.* Bottom-up Assembled Synthetic SARS-CoV-2 Miniviruses Reveal Lipid Membrane Affinity of Omicron Variant Spike Glycoprotein. *ACS Nano* **17,** 23913–23923 (2023).

159. Overduin, M., Kervin, T. A. & Tran, A. Progressive membrane-binding mechanism of SARS-CoV-2 variant spike proteins. *Iscience* **25** (2022).
160. Conca, D. V. *et al.* Variant-specific interactions at the plasma membrane: Heparan sulfate's impact on SARS-CoV-2 binding kinetics. *bioRxiv,* 2024–01 (2024).
161. Nieuwland, R., Siljander, P. R.-M., Falcón-Pérez, J. M. & Witwer, K. W. Reproducibility of extracellular vesicle research. *European journal of cell biology* **101,** 151226 (2022).
162. Nie, J. *et al.* Establishment and validation of a pseudovirus neutralization assay for SARS-CoV-2. *Emerging microbes & infections* **9,** 680–686 (2020).
163. Xu, R., Shi, M., Li, J., Song, P. & Li, N. Construction of SARS-CoV-2 virus-like particles by mammalian expression system. *Frontiers in bioengineering and biotechnology* **8,** 862 (2020).
164. Charles, P. T. *et al.* Reduction of non-specific protein adsorption using poly (ethylene) glycol (PEG) modified polyacrylate hydrogels in immunoassays for staphylococcal enterotoxin B detection. *Sensors* **9,** 645–655 (2009).
165. Xu, F. *et al.* Spatially well-defined binary brushes of poly (ethylene glycol) s for micropatterning of active proteins on anti-fouling surfaces. *Biosensors and Bioelectronics* **24,** 773–780 (2008).
166. Kamiya, K., Kobayashi, J., Yoshimura, T. & Tsumoto, K. Confocal microscopic observation of fusion between baculovirus budded virus envelopes and single giant unilamellar vesicles. *Biochimica et Biophysica Acta (BBA)-Biomembranes* **1798,** 1625–1631 (2010).
167. Kovalev, N., Pogany, J. & Nagy, P. D. Reconstitution of an RNA virus replicase in artificial giant unilamellar vesicles supports full replication and provides protection for the double-stranded RNA replication intermediate. *Journal of Virology* **94,** 10–1128 (2020).
168. Kam, Y.-W. *et al.* Cleavage of the SARS coronavirus spike glycoprotein by airway proteases enhances virus entry into human bronchial epithelial cells in vitro. *PloS one* **4,** e7870 (2009).
169. Nakase, I., Noguchi, K., Fujii, I. & Futaki, S. Vectorization of biomacromolecules into cells using extracellular vesicles with enhanced internalization induced by macropinocytosis. *Scientific reports* **6,** 34937 (2016).
170. Nakase, I. *et al.* Receptor clustering and activation by multivalent interaction through recognition peptides presented on exosomes. *Chemical Communications* **53,** 317–320 (2017).
171. Marty, C, Meylan, C, Schott, H, Ballmer-Hofer, K & Schwendener, R. Enhanced heparan sulfate proteoglycan-mediated uptake of cell-penetrating peptide-

modified liposomes. *Cellular and Molecular Life Sciences CMLS* **61,** 1785–1794 (2004).

172. Subramaniam, S. *et al.* Protein adsorption determines pulmonary cell uptake of lipid-based nanoparticles. *Journal of Colloid and Interface Science* **641,** 36–47 (2023).
173. Chanaday, N. L. & Kavalali, E. T. Time course and temperature dependence of synaptic vesicle endocytosis. *FEBS letters* **592,** 3606–3614 (2018).
174. Tomoda, H., Kishimoto, Y. & Lee, Y. Temperature effect on endocytosis and exocytosis by rabbit alveolar macrophages. *Journal of Biological Chemistry* **264,** 15445–15450 (1989).
175. Li, X. *et al.* Dependence of SARS-CoV-2 infection on cholesterol-rich lipid raft and endosomal acidification. *Computational and Structural Biotechnology Journal* **19,** 1933–1943 (2021).
176. Boyce, A. & Walsh, G. Production, characteristics and applications of microbial heparinases. *Biochimie* **198,** 109–140 (2022).
177. Han, Y.-H. *et al.* Structural snapshots of heparin depolymerization by heparin lyase I. *Journal of Biological Chemistry* **284,** 34019–34027 (2009).
178. Zang, R. *et al.* Cholesterol 25-hydroxylase suppresses SARS-CoV-2 replication by blocking membrane fusion. *Proceedings of the National Academy of Sciences* **117,** 32105–32113 (2020).
179. Rodal, S. K. *et al.* Extraction of cholesterol with methyl-$\beta$-cyclodextrin perturbs formation of clathrin-coated endocytic vesicles. *Molecular biology of the cell* **10,** 961–974 (1999).
180. Odnoshivkina, U. G., Kuznetsova, E. A. & Petrov, A. M. 25-hydroxycholesterol as a signaling molecule of the nervous system. *Biochemistry (Moscow)* **87,** 524–537 (2022).
181. Wang, S. *et al.* Cholesterol 25-Hydroxylase inhibits SARS-CoV-2 and other coronaviruses by depleting membrane cholesterol. *The EMBO journal* **39,** e106057 (2020).
182. Parasassi, T., Krasnowska, E. K., Bagatolli, L. & Gratton, E. Laurdan and Prodan as polarity-sensitive fluorescent membrane probes. *Journal of fluorescence* **8,** 365–373 (1998).
183. Kim, H. M. *et al.* A two-photon fluorescent probe for lipid raft imaging: C-Laurdan. *ChemBioChem* **8,** 553–559 (2007).
184. Aguilar, L. F. *et al.* Differential dynamic and structural behavior of lipid-cholesterol domains in model membranes. *PloS one* **7,** e40254 (2012).

185. Shentu, T.-P. *et al.* oxLDL-induced decrease in lipid order of membrane domains is inversely correlated with endothelial stiffness and network formation. *Biophysical Journal* **98,** 366a (2010).
186. Domingues, M. M., Gomes, B., Hollmann, A. & Santos, N. C. 25-Hydroxycholesterol effect on membrane structure and mechanical properties. *International Journal of Molecular Sciences* **22,** 2574 (2021).
187. Owen, D. M., Rentero, C., Magenau, A., Abu-Siniyeh, A. & Gaus, K. Quantitative imaging of membrane lipid order in cells and organisms. *Nature protocols* **7,** 24–35 (2012).
188. El-Baz, N., Nunn, B. M., Bates, P. J. & O'Toole, M. G. The impact of PEGylation on cellular uptake and in vivo biodistribution of gold nanoparticle MRI contrast agents. *Bioengineering* **9,** 766 (2022).
189. Mitchell, M. J. *et al.* Engineering precision nanoparticles for drug delivery. *Nature reviews drug discovery* **20,** 101–124 (2021).
190. Nicoletti, I., Migliorati, G., Pagliacci, M., Grignani, F. & Riccardi, C. A rapid and simple method for measuring thymocyte apoptosis by propidium iodide staining and flow cytometry. *Journal of immunological methods* **139,** 271–279 (1991).
191. Li, K. *et al.* High cholesterol induces apoptosis and autophagy through the ROS-activated AKT/FOXO1 pathway in tendon-derived stem cells. *Stem cell research & therapy* **11,** 1–16 (2020).
192. Wei, C. *et al.* HDL-scavenger receptor B type 1 facilitates SARS-CoV-2 entry. *Nature metabolism* **2,** 1391–1400 (2020).
193. Wang, H. *et al.* The role of high cholesterol in SARS-CoV-2 infectivity. *Journal of Biological Chemistry* **299** (2023).
194. Magarkar, A. *et al.* Cholesterol level affects surface charge of lipid membranes in saline solution. *Scientific reports* **4,** 5005 (2014).
195. Konermann, L. Protein unfolding and denaturants. *e LS* (2001).
196. Haraszti, R. A. *et al.* High-resolution proteomic and lipidomic analysis of exosomes and microvesicles from different cell sources. *Journal of extracellular vesicles* **5,** 32570 (2016).
197. Patel, D. B. *et al.* Impact of cell culture parameters on production and vascularization bioactivity of mesenchymal stem cell-derived extracellular vesicles. *Bioengineering & translational medicine* **2,** 170–179 (2017).
198. Costello, D. A., Hsia, C.-Y., Millet, J. K., Porri, T. & Daniel, S. Membrane fusion-competent virus-like proteoliposomes and proteinaceous supported bilayers made directly from cell plasma membranes. *Langmuir* **29,** 6409–6419 (2013).

199. Tsumoto, K. & Yoshimura, T. Recombinant proteoliposomes prepared using baculovirus expression systems. *Methods in enzymology* **465,** 95–109 (2009).
200. Himbert, S. *et al.* Erythro-VLPs: Anchoring SARS-CoV-2 spike proteins in erythrocyte liposomes. *Plos one* **17,** e0263671 (2022).
201. Zhukovsky, M. A., Filograna, A., Luini, A., Corda, D. & Valente, C. Phosphatidic acid in membrane rearrangements. *Febs Letters* **593,** 2428–2451 (2019).
202. Vigant, F., Jung, M. & Lee, B. Positive reinforcement for viruses. *Chemistry & biology* **17,** 1049–1051 (2010).
203. Tran, N., Oh, Y., Sutherland, M., Cui, Q. & Hong, M. Cholesterol-mediated clustering of the HIV fusion protein gp41 in lipid bilayers. *Journal of molecular biology* **434,** 167345 (2022).
204. Ando, M., Schikula, S., Sasaki, Y. & Akiyoshi, K. Proteoliposome engineering with cell-free membrane protein synthesis: Control of membrane protein sorting into liposomes by chaperoning systems. *Advanced Science* **5,** 1800524 (2018).
205. Kuruma, Y. & Ueda, T. The PURE system for the cell-free synthesis of membrane proteins. *Nature protocols* **10,** 1328–1344 (2015).
206. Yang, Q. *et al.* Role for N-glycans and calnexin-calreticulin chaperones in SARS-CoV-2 Spike maturation and viral infectivity. *Science Advances* **8,** eabq8678 (2022).
207. Chakiath, C. S. & Esposito, D. Improved recombinational stability of lentiviral expression vectors using reduced-genome Escherichia coli. *Biotechniques* **43,** 466–470 (2007).
208. Damasceno, J. D. *et al.* Functional compartmentalization of Rad9 and Hus1 reveals diverse assembly of the 9-1-1 complex components during the DNA damage response in Leishmania. *Molecular microbiology* **101,** 1054–1068 (2016).
209. Lettice, L. A., Devenney, P., De Angelis, C. & Hill, R. E. The conserved sonic hedgehog limb enhancer consists of discrete functional elements that regulate precise spatial expression. *Cell reports* **20,** 1396–1408 (2017).
210. Brunelle, J. L. & Green, R. in *Methods in enzymology* 161–167 (Elsevier, 2014).
211. Ramm, F. *et al.* The Potential of Eukaryotic Cell-Free Systems as a Rapid Response to Novel Zoonotic Pathogens: Analysis of SARS-CoV-2 Viral Proteins. *Frontiers in Bioengineering and Biotechnology* **10,** 896751 (2022).
212. Twigg, S. M. & Baxter, R. C. Insulin-like growth factor (IGF)-binding protein 5 forms an alternative ternary complex with IGFs and the acid-labile subunit. *Journal of Biological Chemistry* **273,** 6074–6079 (1998).

213. Sachse, R., Dondapati, S. K., Fenz, S. F., Schmidt, T. & Kubick, S. Membrane protein synthesis in cell-free systems: From bio-mimetic systems to bio-membranes. *FEBS letters* **588,** 2774–2781 (2014).
214. Kesidis, A. *et al.* Expression of eukaryotic membrane proteins in eukaryotic and prokaryotic hosts. *Methods* **180,** 3–18 (2020).
215. Murtas, G., Kuruma, Y., Bianchini, P., Diaspro, A. & Luisi, P. L. Protein synthesis in liposomes with a minimal set of enzymes. *Biochemical and biophysical research communications* **363,** 12–17 (2007).
216. Kuruma, Y., Nishiyama, K.-i., Shimizu, Y., Müller, M. & Ueda, T. Development of a minimal cell-free translation system for the synthesis of presecretory and integral membrane proteins. *Biotechnology progress* **21,** 1243–1251 (2005).
217. Das, T. & Mukhopadhyay, C. Identification of possible binding modes of SARS-CoV-2 spike N-terminal domain for ganglioside GM1. *Chemical Physics Letters* **812,** 140260 (2023).
218. Negi, G. *et al.* SARS-CoV-2 Binding to Terminal Sialic Acid of Gangliosides Embedded in Lipid Membranes. *ACS Infectious Diseases* **9,** 1346–1361 (2023).
219. Nguyen, L. *et al.* Sialic acid-containing glycolipids mediate binding and viral entry of SARS-CoV-2. *Nature Chemical Biology* **18,** 81–90 (2022).
220. Sim, J.-R. *et al.* Amelioration of SARS-CoV-2 infection by ANO6 phospholipid scramblase inhibition. *Cell reports* **40** (2022).
221. Croset, A. *et al.* Differences in the glycosylation of recombinant proteins expressed in HEK and CHO cells. *Journal of biotechnology* **161,** 336–348 (2012).
222. Zhang, F. *et al.* SARS-CoV-2 spike glycosylation affects function and neutralization sensitivity. *Mbio* **15,** e01672–23 (2024).
223. Song, H. C. *et al.* Synthesis and characterization of a native, oligomeric form of recombinant severe acute respiratory syndrome coronavirus spike glycoprotein. *Journal of virology* **78,** 10328–10335 (2004).
224. Shi, W. *et al.* Cryo-EM structure of SARS-CoV-2 postfusion spike in membrane. *Nature* **619,** 403–409 (2023).
225. Arrildt, K. T., Joseph, S. B. & Swanstrom, R. The HIV-1 env protein: a coat of many colors. *Current Hiv/Aids Reports* **9,** 52–63 (2012).
226. Aloia, R. C., Tian, H. & Jensen, F. C. Lipid composition and fluidity of the human immunodeficiency virus envelope and host cell plasma membranes. *Proceedings of the National Academy of Sciences* **90,** 5181–5185 (1993).
227. Venkatachalam, R. & Subramaniyan, V. Homology and conservation of amino acids in E-protein sequences of dengue serotypes. *Asian Pacific Journal of Tropical Disease* **4,** S573–S577 (2014).

228. Halstead, S. B. Dengue antibody-dependent enhancement: knowns and unknowns. *Antibodies for Infectious Diseases,* 249–271 (2015).
229. Zheng, T. & Huo, Q. A nanoparticle pseudo pathogen for rapid detection and diagnosis of virus Infection. *Sensors International* **1,** 100010 (2020).
230. Tang, X., Zhang, Y. & Han, X. Ionizable Lipid Nanoparticles for mRNA Delivery. *Advanced NanoBiomed Research* **3,** 2300006 (2023).
231. Li, M. *et al.* Discovery and characterization of a peptide that enhances endosomal escape of delivered proteins in vitro and in vivo. *Journal of the American Chemical Society* **137,** 14084–14093 (2015).
232. Heuvingh, J, Pincet, F & Cribier, S. Hemifusion and fusion of giant vesicles induced by reduction of inter-membrane distance. *The European Physical Journal E* **14,** 269–276 (2004).
233. Noyce, R. S., Lederman, S. & Evans, D. H. Construction of an infectious horsepox virus vaccine from chemically synthesized DNA fragments. *PloS one* **13,** e0188453 (2018).
234. Levine, R. M., Pearce, T. R., Adil, M. & Kokkoli, E. Preparation and characterization of liposome-encapsulated plasmid DNA for gene delivery. *Langmuir* **29,** 9208–9215 (2013).
235. Garenne, D. *et al.* Cell-free gene expression. *Nature reviews methods primers* **1,** 49 (2021).
236. Plavec, Z. *et al.* SARS-CoV-2 production, purification methods and UV inactivation for proteomics and structural studies. *Viruses* **14,** 1989 (2022).

# 8 Appendix

## 8.1 List of publications

I have authored and coauthored the following publications:

Yagüe Relimpio, A. *et al.* Bottom-up Assembled Synthetic SARS-CoV-2 Miniviruses Reveal Lipid Membrane Affinity of Omicron Variant Spike Glycoprotein. *ACS Nano* **17,** 23913–23923 (2023)

Fink, A. *et al.* Extracellular Cues Govern Shape and Cytoskeletal Organization in Giant Unilamellar Lipid Vesicles. *ACS Synthetic Biology* **12,** 369–374 (2023)

Staufer, O. *et al.* Synthetic virions reveal fatty acid-coupled adaptive immunogenicity of SARS-CoV-2 spike glycoprotein. *Nature Communications* **13,** 868 (2022)

## 8.2 List of abbreviations

| | |
|---|---|
| SLB | supported lipid bilayer |
| GUV | giant unilamellar vesicle |
| SUV | small unilamellar vesicle |
| S | spike glycoprotein |
| RBD | receptor binding domain |
| ACE2 | angiotensin-converting enzyme 2 |
| ERGIC | endoplasmic reticulum-Golgi intermediate compartment |
| QCM-D | quartz crystal microbalance with dissipation monitoring |
| NTA | nitrilotriacetic acid |
| PEG | polyethylene glycol |
| MiniVs | synthetic SARS-CoV-2 miniviruses |
| SARS-CoV-2 | severe acute respiratory syndrome coronavirus 2 |
| HIV | human immunodeficiency virus |
| BSL | biosafety level |
| DOPC | 1,2-Dioleoyl-sn-glycero-3-phosphocholine |
| DOPG | 1,2-dioleoyl-sn-glycero-3-phospho-(1'-rac-glycerol) |
| DOPE | 1,2-dioleoyl-sn-glycero-3-phosphoethanolamine |
| DOPS | 1,2-dioleoyl-sn-glycero-3-phospho-L-serine |
| Liss Rhod PE | 1,2-dioleoyl-sn-glycero-3-phosphoethanolamine-N-(lissamine rhodamine B sulfonyl) |
| DGS NTA($Ni^{2+}$) | 1,2-dioleoyl-sn-glycero-3-[(N-(5-amino-1-carboxypentyl)-iminodiacetic acid)succinyl] |
| SM | 1N-nervonoyl-D-erythro-sphingosylphosphorylcholine |
| DOPI | 1,2-dioleoyl-sn-glycero-3-phospho-(1'-myo-inositol) |
| PA | phosphatidic acid |
| M$\beta$CD | methyl-$\beta$-cyclodextrin |
| 25HC | 25-hydroxycholesterol |
| SL | sphingolipids |
| GP | general polarisation |
| IVT | in vitro translation |
| CFPS | cell-free protein synthesis |
| PURE | protein synthesis using recombinant elements |
| GFP | green fluorescent protein |
| tGFP | turboGFP |
| IRES | internal ribosomal entry site |
| RBS | ribosomal binding site |
| SDS-PAGE | sodium dodecyl sulfate-polyacrylamide gel electrophoresis |
| PFA | paraformaldehyde |
| BSA | bovine serum albumin |
| FC | flow cytometry |
| MS | mass spectrometry |
| IS | internal standard |